STUDYING THE STRUCTURAL DYNAMICS AND APTAMER-LIGAND INTERACTIONS IN THE COCAINE-BINDING APTAMER THROUGH FLUORESCENCE SPECTROSCOPY

ARON A. SHOARA

A DISSERTATION SUBMITTED TO
THE FACULTY OF GRADUATE STUIDES
IN PARTIAL FULFILLMENT OF THE REQUIREMENTS
FOR THE DEGREE OF
DOCTOR OF PHILOSOPHY

GRADUATE PROGRAM IN CHEMISTRY
YORK UNIVERSITY
TORONTO, ONTARIO

AUGUST 2022

Abstract

Since its first report in 1990, aptamers have been utilized in biosensor modeling technologies. One of the most important advantages of using aptamers is the structural flexibility and thermal stability of nucleic acids. These structural merits enable aptamers to be linked on solid surfaces, attached to chemical labels, or extended to build nanostructures for advanced therapeutic and diagnostic modeling purposes. The cocaine-binding aptamer was originally selected through a systematic evolution of ligands by exponential enrichment (SELEX) method to select cocaine molecules from cocaine metabolites in biological solutions. However, the aptamer showed binding to quinine and other antimalaria drugs tighter than its original ligand, cocaine.

Work presented in this dissertation demonstrate how the cocaine-binding aptamer can be exploited as a model system for the structural analysis of aptamers using biophysical techniques including fluorometry methods. The results discussed in this study demonstrate how intrinsic fluorescence of ligands was exploited for aptamer-ligand binding and thermal stability analyses. Furthermore, photoisomerization of stilbene coupled with ligand-induced binding mechanism of the cocaine-binding aptamer were employed for the development of the Photochrome Aptamer Switch Assay.

This research aims to gain insight into how aptamers interact with their ligands by utilizing the fluorescence properties of the ligands. Investigating the binding mechanisms of aptamers is essential in sensing technology since biosensors yield greater analytical sensitivity upon ligand-induced structural changes.

It is your light that lights the worlds. *Rumi*

I dedicate this to my family for their endless love and support.

Acknowledgements

I would like to express my deepest gratitude to my supervisor and mentor Professor Philip E. Johnson for teaching me analytical techniques and critical thinking skills. I am deeply indebted to Professor Johnson for providing me the opportunity to learn and practice in his research laboratory. Professor Johnson's humble, kind, and encouraging guidance through this gratifying chapter of my life will always stay with me.

I would like to extend my sincere appreciations to my committee members, Professor Logan Donaldson, and Professor Gerald Audette, for your valued time, meticulous expertise, and seamless support that you have offered to me throughout this project. I appreciate that you allowed me to use your research laboratories. I am also thankful to my examiners, Professor Patricia Lakin-Thomas, and Professor Thorsten Dieckmann, for your valued time and your constructive comments.

My sincere thanks to my lab members: Dr. Miguel Neves, Dr. Sladjana Slavkovic, and Dr. Zach Churcher for your kind friendship, delicate support, and inclined discussions. This endeavor would not have been possible without you.

I would like to extend my gratitude to my collaborators: Professor Richard Manderville, Professor Cameron Mackereth, Professor Sergey Krylov, and Professor Heyu Ni for sharing your bright ideas with me.

Table of Contents

List of Figures

List of Tables

List of Abbreviations

Abbreviation	*Description*
3WJ	Three-way junction
a.k.a.	Also known as
a.u.	Arbitrary units
ACN	Acetonitrile
ART	Artemisinin
ATP	Adenosine triphosphate
ATP#	ATP binding aptamer
B	Photophysical brightness
bp	Base pair
Btz	N-methylbenzothiazolium
CD	Circular dichroism
CE	Capillary electrophoresis
C_{LoD}	Concentration limit of detection
C_{LoQ}	Concentration limit of quantification
CV	Coefficient of variation
Cy#	Cyanine fluorophore variant
ddH_2O	Distilled deionized water
DIDS	4,4'-diisothiocyano-2,2'-disulfonic stilbene
DMSO	Dimethyl sulfoxide
DSC	Differential scanning calorimetry
emi.	Emission
eq.	Molar equivalent
Eq.	Equation
ESS	Spectral slit width
EtBr	Ethidium bromide
eV	Electron volt
exc.	Excitation
F7.9D	Cocaine-binding aptamer variant
FAM	Carboxyfluorescein
FRET	Förster resonance energy transfer
G	Guanine
G	Instrument grating factor
h	Hour
HIV	Human immunodeficiency virus
IPTG	Isopropyl β-D-1-thiogalactopyranoside
ITC	Isothermal titration calorimetry

Abbreviation	*Description*
In vitro	Within glass, chemical and biological experiments in test tubes
In vivo	Within living, chemical and biological experiments in cells
I_{vh}	Intensity vertical-horizontal
I_{vv}	Intensity vertical-vertical
K_a	Association constant, affinity
Ka	Ionization constant of acid
k_{app}	Apparent kinetic decay constant
K_d	Dissociation constant
kDa	Kilodaltons
k_a	Absorbance rate constant
k_f	Fluorescence rate constant
k_{ic}	Internal conversion rate constant
k_{isc}	Intersystem crossing rate constant
k_p	Phosphorescence rate constant
k_q	Quenching rate constant
K_{sv}	Stern-Volmer constant
M	Molar, $mol \cdot litre^{-1}$
MAPS	Minimum aptamer publication standards
mM	$Millimole \cdot litre^{-1}$
MN#	Cocaine-binding aptamer variants
MNS	Cocaine-binding aptamer variant
mRNA	Messenger ribonucleic acid
N	$Normal, equivalent \cdot litre^{-1}$
NBW	Natural bandwidth
ND	Not determined
NECEEM	Non-equilibrium capillary electrophoresis of equilibrium mixtures
nm	Nanometre
NMR	Nuclear magnetic resonance
OD	Optical density
OR#	Cocaine-binding aptamer variants
OTA	Ochratoxin A aptamer
PBS	Phosphate-buffered saline
PCR	Polymerase chain reaction
PHASA	Photochrome aptamer switch assay
pH	Power of hydrogen, negative base-10 logarithm of H^+ in molar concentration
pKa	Power of ionization constant, negative base-10 logarithm of Ka

Abbreviation	*Description*
PMT	Photomultiplier tube
RFU	Relative fraction unit
R_g	Radius of gyration
RSD	Relative standard deviation
r	Fluorescence anisotropy
RSDR	Among-laboratory relative standard deviation
S/N	Signal to noise ratio
SAXS	Small angle X-ray scattering
SBW	Spectral bandwidth
SD	Standard deviation
SEC	Size-exclusion chromatography
SELEX	Systematic evolution of ligands by exponential enrichment
SITS	4-acetamido-4'-isothiocyano-2,2'-disulfonic stilbene
ssDNA	Single-stranded deoxyribonucleic acid
SS1	Negative control for the cocaine-binding aptamer
$S_{y/x}$	Standard deviation of the linear regression residuals
t-SITS	Trans isomer of SITS
T_m	Denaturation point, melting temperature
Tris	Trisaminomethane
TWJ#	Three-way junction aptamer variants
UTP	Uracil triphosphate
UV-Vis	Ultraviolet-visible
V	Volt
WC	Watson-Crick base pair
ΔF	Difference between the fluorescence intensities
ΔG	Change in Gibbs free energy
ΔH	Enthalpy change
ΔS	Entropy change
ε	Extinction coefficient, molar absorptivity
λ	Wavelength
μM	Micromole·litre^{-1}
μs	Microseconds
η	Refractive index
τ	Fluorescence lifetime
Φ_f	Fluorescence quantum yield

Chapter 1: Introduction

1.1 Preface

This chapter includes an introduction to the concept of aptamers and biophysical techniques used to study aptamers. Presented materials in this chapter and subsequent chapters including discussions, results, figures, tables, and illustrations were produced by the author of this dissertation unless referenced or stated otherwise.

1.2 Introduction to Aptamers

Aptamers are a wide class of single-stranded oligonucleotides with the ability to bind various targets ranging from small molecules to macromolecules. The aptamer-target interaction can take place *in vitro* or *in vivo* [1,2]. By targeting specific macromolecules located on the cell membrane, aptamers are capable of identifying whole cells. The aptamer-target interaction is often specific with a high affinity [3]. Although there is no formal limit on the length of aptamers, the construct sequences can be extended up to 100 nucleotides in either RNA, DNA, or a chimeric form. While most of aptamers are chemically synthesized *in vitro*, they naturally exist *in vivo* and have been reported in riboswitches and ribozymes [4,5].

The process of *in vitro* selection of aptamers was first introduced by Craig Tuerk and Larry Gold in 1990, when Tuerk and Gold aimed to isolate ssRNA molecules that can bind T4 DNA polymerase gp43 protein from a randomly calculated pool of ssRNA sequences holding over 65,536 possible combinations [1]. This process generated only two ssRNA molecules capable of strong binding to the target (T4 DNA polymerase gp43 protein) with similar affinities. One of these two ssRNA molecules was, in fact, the wild-type sequence in the native mRNA hairpin

structure [1]. While Craig Tuerk and Larry Gold named their protocol as Systematic Evolution of Ligands by Exponential Enrichment (SELEX), Andrew Ellington and Jack Szostak formulated the term '*aptamer*' from a Latin-Greek motto of '*aptus meros*' meaning fitting part for their candidate RNA molecule, which was selected form ten billion random sequences to specifically bind the target organic dyes [2].

In the beginning stages of aptamer selection, it was thought that RNA molecules were the only oligonucleotide candidate since RNA molecules are structurally more diverse than DNA molecules due to inherently dynamic RNA motifs [6]. However, Ellington and Szostak introduced the first DNA aptamer and showed that DNA aptamers are more sequence- and ligand-specific than RNA aptamers [7]. In addition to DNA and RNA aptamers, Colas *et al*. adapted the traditional yeast two-hybrid system and selected the first peptide aptamer from a library of three billion inert scaffold proteins for a specific and sensitive *in vitro* and *in vivo* target interaction [8,9]. Though, the utilization of peptide aptamers has remined infrequent due its complicated production and similarities to well-stablished methods for monoclonal antibodies [10–12]. In this work unless specified otherwise, the term aptamer is used to refer to conventionally known nucleic acid aptamers. Also, required standards for aptamer research outlined by MAPS were applied [13].

The advantages of DNA aptamers are that they are chemically and thermal stable and can renature after chemical or thermal denaturation as long as their phosphodiester bonds are unaffected [14,15]. Additionally, aptamers can be chemically modified with amino and/or thiol linker at either or both 3' or/and 5' ends. These modifications can further be employed for covalent attachment of aptamers to fluorophore reporters, nanoparticles, or solid surfaces [16–20]. On the

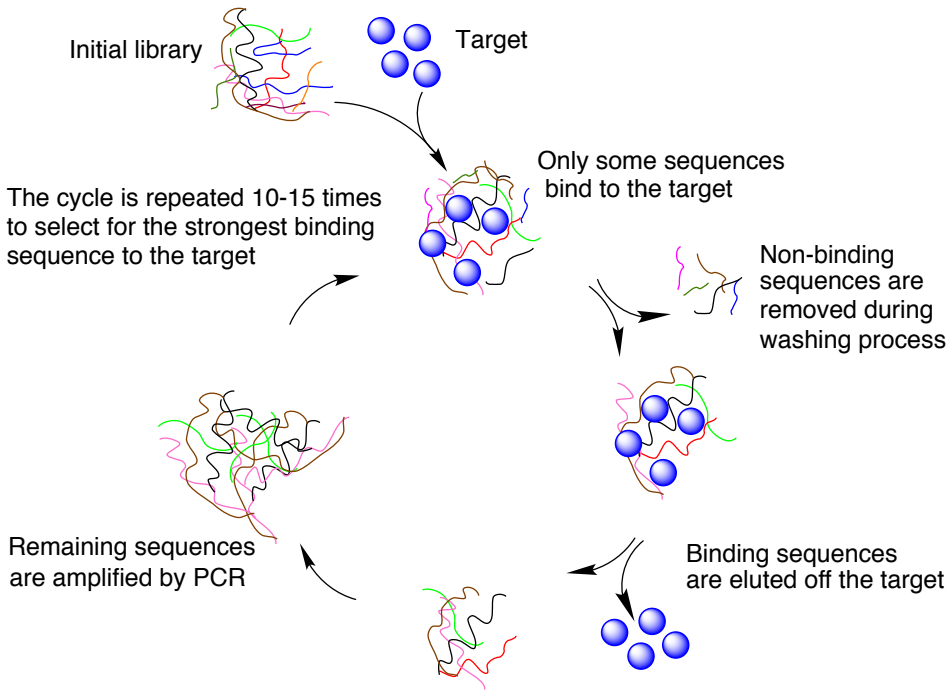

Figure 1.1 Diagram of SELEX process. First, the target ligand exposed to an initial library of aptamer sequences and incubated under the desired condition. For instance, human serum if the target of interest is aimed to be selected in human serum or plasma. Next, non-binding sequences are removed during the wash and bound sequences are collected and amplified using PCR, and re-exposed to the initial target of interest. This cycle is repeated several times. Finally, the bound aptamers are sequenced to retrieve the primary structure of the aptamer. Further optimization and characterization of aptamers can be conducted once the primary structure is known.

other hand, the challenge of using aptamers is that what sequences to include in the initial random pool of SELEX [4,21]. The original SELEX method, as illustrated in Figure 1.1, was based on three steps of *selection*, *separation*, and *amplification* [1]. Several optimization and modification steps have been added to SELEX to enhance the target specificity and affinity of aptamer selection. For instance, Counter SELEX method supplies an extra step, where undesirable ligand analogs are added to the retained sequences to remove non-specific sequences from each cycle [22]. Table 1.1 lists methods of SELEX optimization and modification techniques available in the literature.

Table 1.1 List of SELEX optimization and modification techniques available in the literature.

Method	*Brief description*	*Reference*
Capture SELEX	Immobilizes the oligonucleotides instead of the target molecules during the aptamer selection process.	[23,24]
Cell-SELEX	Targets cell surface transmembrane proteins for cell-specific aptamers.	[25,26]
Counter SELEX	Uses ligand analogues to generate aptamers without co-affinity for small molecule analogues.	[22]
Non-SELEX	Employs a highly efficient affinity method (NECEEM) with repetitive steps of partitioning without amplification in between.	[27,28]
Flu-Mag SELEX	Uses immobilization of streptavidin-coated magnetic beads with biotinylated molecules to select DNA aptamers for targets with very different properties and size.	[29,30]
Silico SELEX	Applies computational and theoretical tools to emulate aptamer selection experiments in silico	[31]
μFFE-SELEX	Involves a perpendicular electric field for the selection method.	[23]
GO-SELEX	Utilizes graphene oxide to enhance screening	[32]
Sweep-CE-SELEX	Uses a non-stopped-flow method to measure bimolecular rate constant of complex formation between protein and DNA.	[33]
Spiegelmers	Uses L-ribonucleic acid aptamer due to highly resistant conformation against nuclease degradation.	[34,35]
SOMAmers	Develops high throughput assays for triaging biomarker candidates against large clinical sample collections.	[36–39]
Thioaptamers	Enhances aptamer immobilization techniques on solid surfaces.	[40]
X-aptamers	Enhances immobilized aptamer binding to the target protein by up to 23-fold, and increasing affinity toward drugs by a million-fold	[41]

1.2.1 Ligand binding specificity

Aptamers often bind their ligands with high affinity and specificity [42,43]. This type of binding property is not exceptionally novel since proteins, as seen in antibodies, have been evolved to have ligand specificity and affinity toward their targets [44,45]. In fact, what makes DNA aptamers interesting macromolecules for target recognition studies are their robustness, stability, sensitivity, low immune response, and their capability of having different binding mechanisms [15,46,47].

Aptamers can be chemically synthesized *in vitro*, which enables aptamers to be commercially available [48]. This is particularly beneficial to research facilities as labs can dedicate their time and resources more efficiently on the research objectives rather than making aptamers in the lab. Thus, the ruggedness factor for the obtained results is improved. The robustness of a method is an evaluation of its capacity to remain unchanged by small, but methodical, variations in the procedure parameters. The ruggedness of an analytical method indicates the degree of reproducibility of test results using the same analytes with different analysts, instruments, and laboratories [49].

Aptamers have a reversible structural stability model in a sense that aptamers, especially DNA aptamers, can be denatured-renatured thermally and chemically many times as long as their primary structure is unchanged [14,15]. Aptamers can be selected to be sensitive to small molecules and are able to distinguish very similar small molecule analogs whereas antibodies are not as sensitive against small molecules as aptamers [50]. Antibodies need to be combined with a conjugate complex molecule to increase the sensitivity against small molecule targets [51]. On the other hand, aptamers do not cause severe immune responses in the host, which makes aptamers to

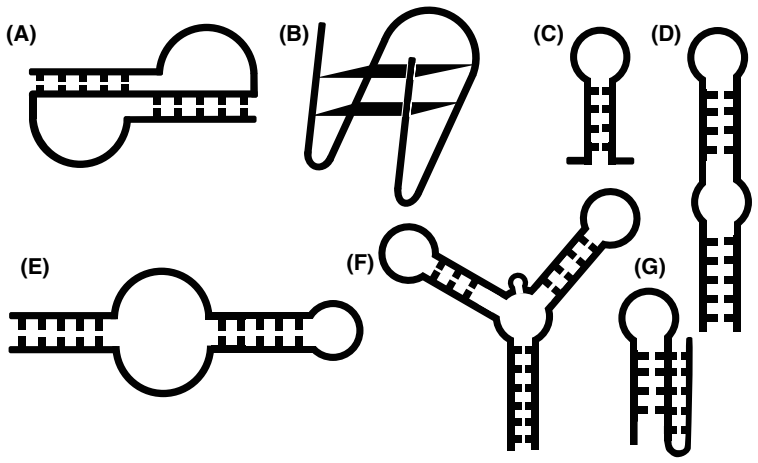

Figure 1.2 Schematic diagrams of the secondary structure motifs of aptamers. (**A**) Pseudoknot, in the HIV-1 reverse transcriptase aptamer [54]. (**B**) G-quartet, in the thrombin aptamer [55]. (**C**) Loop and (**D**) Loop/bulge, in the ATP aptamer [56]. (**E**) Hairpin, in bacteriophage T4 polymerase aptamer [57]. (**F**) Three-way junction, in the cocaine-binding and cholic acid binding aptamers [58,59]. (**G**) Triple helix (*a.k.a.* triplex), in the codeine-binding aptamer [60].

be great candidates for *in vivo* applications [15,46,47]. Moreover, having a variety of structural motifs such as pseudoknots, G-quartets, hairpins, and loops, either without the ligand or induced by the ligand, enables aptamers to have different binding mechanisms. These binding mechanisms are governed by non-covalent interactions such as hydrogen bonds, electrostatic interactions, van der Walls forces, and hydrophobic interactions (π-π stacking and intercalation) [52,53]. Figure 1.2 illustrates diagrams of the main structural motifs of aptamers and their target ligands [54–60].

1.2.2 The cocaine-binding aptamer

The cocaine-binding aptamer was originally selected by Stojanovic *et al.* in 2000 using SELEX to distinguish cocaine from cocaine metabolites. As shown in Figure 1.3, the original cocaine-binding split-aptamer constructs contained 43 nucleotides with a dissociation constant (K_d) of 5 μM at room temperature [61]. Additional studies of Stojanovic *et al.* showed that the MNS 4.1 aptamer (38 nucleotides) was partially folded in free state and becomes fully structured in cocaine-bound

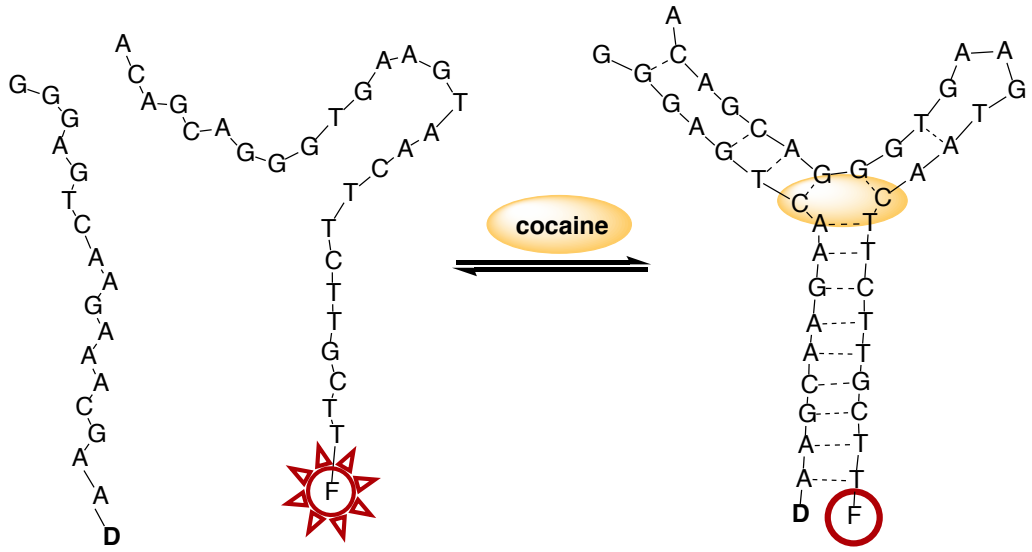

Figure 1.3 Self-assembly of two aptamer constructs in the absence and presence of cocaine. Dabcyl quencher is covalently attached to 3' end and denoted as **D**, and 6-FAM fluorophore to 5' end displayed as **F**, which is excited at 472 nm. When split aptamers are free of cocaine, the fluorescence of 6-FAM is detected at 518 nm. When bound to cocaine, dabcyl quenches the emitted fluorescence of 6-FAM. Experiments were performed in 20 mM Tris (pH 7.4), 140 mM NaCl, 5 mM KCl, 1 mM $MgCl_2$ at room temperature (presumably 20 °C to 25 °C) [61].

state with a K_d range of ~0.4-10 µM at room temperature. Also, the F7.9D aptamer (30 nucleotides) becomes folded in presence of cocaine with a K_d of 100 µM at room temperature [62,63].

Sequence and binding optimization studies by Neves *et al.* provided evidence for the optimized variants of the cocaine-binding aptamer. Neves *et al.* used Isothermal Titration Calorimetry (ITC) and Nuclear Magnetic Resonance (NMR) spectroscopy methods to confirm the three-way junction (3WJ) structure and show sequences of stem 1 were essential for ligand binding, and that having 4 base pairs (bp) in stem 1 is the minimum number of sequences required for the aptamer to fold in the absence of ligand (Figure 1.4). Neves *et al.* also showed stem 2 has

only Watson-Crick base pairs while stems 1 and 3 include two non-canonical AG base pairs and a mismatched thymine (T20) in the absence of the ligand. This optimized variant of the cocaine-binding aptamer (MN4) has 36 nucleotides, is pre-folded in the absence of ligand, and binds cocaine ligand with K_d of 5 μM at 15 °C [58,64,65].

Ligand specificity of the cocaine-binding aptamer was studied by Reinstein *et al.* and Stojanovic *et al*. Their studies showed the cocaine-binding aptamer has a binding promiscuity toward quinine with a 50-fold tighter affinity (K_d = 0.11 μM at 15 °C) as opposed to that of with cocaine [66,67]. Moreover, findings of Slavkovic *et al.* confirmed that the cocaine-binding aptamer binds other quinidine alkaloid ligands such as chloroquine with higher affinity than it does against cocaine and quinine. Competitive ligand displacement analyses verified that quinine and cocaine ligands compete for the same binding site [68,69]. Also, Churcher *et al.* employed NMR techniques to quantify imino exchange rates of the cocaine-binding aptamer variants (MN4 and MN19). The MN19 construct is shorter than MN4 by three canonical base pairs in stem 1. Churcher *et al.* showed that the MN19 aptamer is loosely folded in the absence of ligand and adding ligand would cause the aptamer to fold [70].

1.2.3 Applications of aptamer-ligand binding studies

The exploitation of aptamers in biosensors has exposed great sensitivity and often specificity of recognition due to the structural dynamics, flexibility and affinity of nucleic acids [71]. The aptamer's alternative affinity for quinidine alkaloids and steroids have enabled this aptamer to be employed as an outstanding experimental three-way junction (3WJ) binding model. The cocaine-binding aptamer has several sequence variants including MN4, MN19 and SS1 aptamer

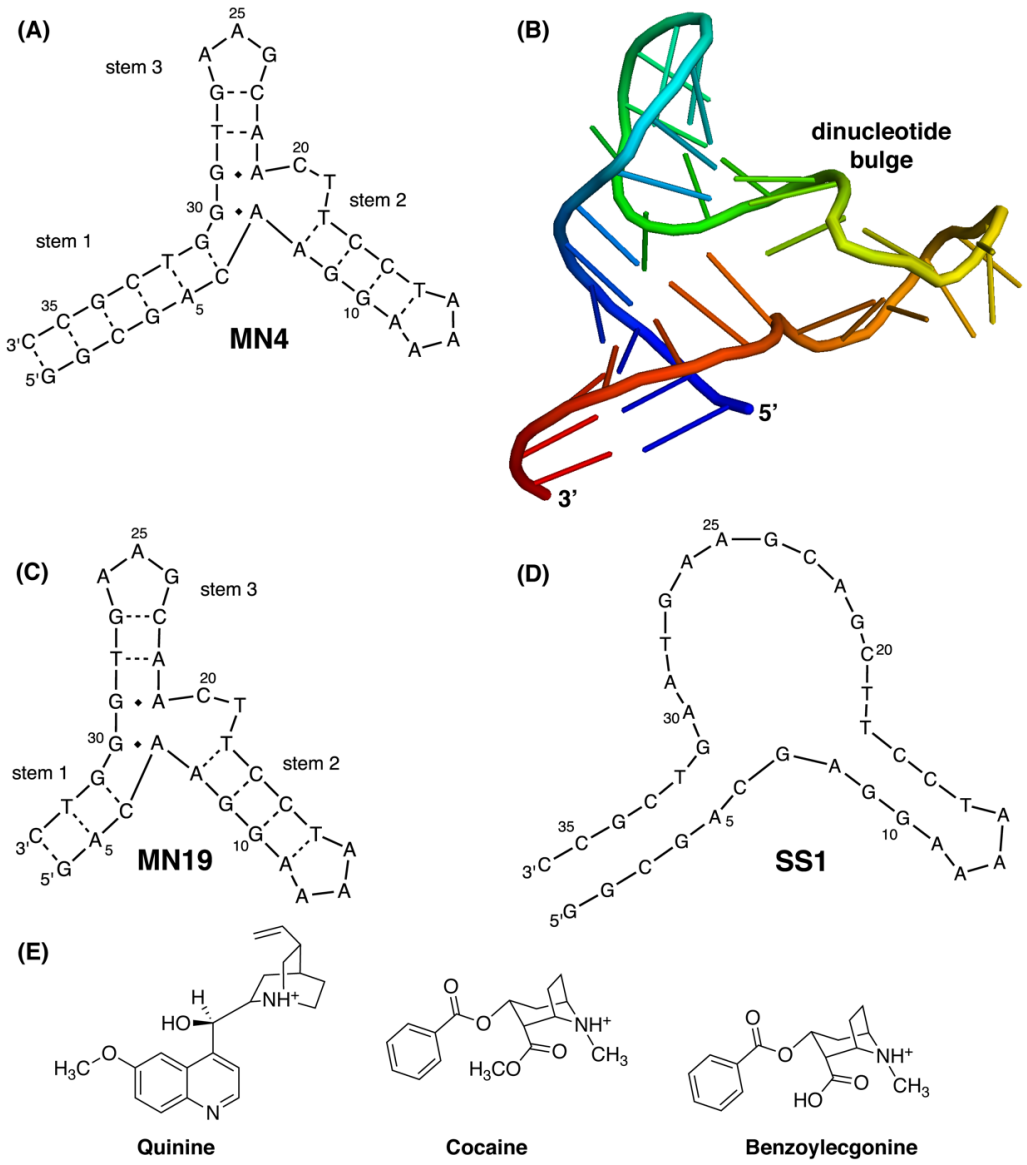

Figure 1.4 Structures of DNA aptamers (**A-D**) and ligands (**E**) discussed in this chapter. Dashed lines between nucleotides indicate Watson-Crick base pairing in the secondary structure, whereas diamonds show non-canonical the AG base pairs. Solid lines display the phosphodiester bonds in the backbone of the aptamers. The 3D structure shown in (**B**) is a predicted crystal structure of MN4 with 1.81Å resolution using DeepRNAFold software [224].

constructs (Figure 1.4). The MN4 and SS1 aptamers are each formed of the same nucleotides. Except, two AG base pairs at the three-way junction are switched to GA in SS1 showing the

sequence specificity of the ligand binding at the three-way junction. This binding hinderance enables SS1 to be utilized as a negative control for binding analyses [58,64,68,72].

The three-way junction (3WJ) structures are naturally occurring motifs in RNA and DNA molecules. Extending three helical stems around a flexible and highly localized electron density junction core, utilizes single stranded nucleic acid molecules (especially rRNA) with additional functionality and stability. The 3WJs can either hold a symmetrical (Y-shaped) or an unsymmetrical (T-shaped) structure, with the stems radiating equilaterally around the core [62,73].

The secondary structure of a known three-way junction construct (TWJ11) with the MN4 aptamer shows conformational similarities in terms of having two unpaired bases and a pseudo-loop (Figure 1.4, dinucleotide bulge) at the core, where two stacked stems are capped with loops [74,75]. In additions to three-way junction motifs, aptamers with G-quadruplex structures have also presented promising functionality in the detection of small molecules such as ochratoxin A, serotonin, dopamine, malachite green as well as macromolecule ligands such as α-thrombin protein or bacteriophage T4 polymerase [43,57,76–79].

1.3 Introduction to Fluorescence

During my last attendance at the Aptamers Conference in Oxford, U.K., I visited the History of Science Museum and Manuscript Treasures Exhibition at the British Library. Having learned fascinating new materials about the history of fluorescence from these exhibitions behooved me to include this section to express how discovery-driven investigations has helped the scientific community to understand the fundamentals of what we know it today as fluorescence.

Mystical blue water

The earliest record of fluorescence goes back to the Aztecs. Nicolás Monardes, a Spanish physician and botanist and Bernardino de Sahagún, a Spanish ethnographer, independently reported in 1565 that Aztec healers mixed woods of a small Mexican tree (coatli) with water to give a bluish opalescence colour. The solution was called "*Matlali*", meaning the blue water, and used as a medicine. A decade later, another botanist Charles de L'Écluse reported medicinal benefits of the blue water for kidney stone and renal pain relief [80]. He named the coatli plant as *Lignum Nephriticum*. Athanasius Kircher, a German pioneer, described his remarks of the blue water extracted from *L. nephriticum* as:

> *"Light passing through an aqueous infusion of this wood appeared more yellow while light reflected from the solution appeared blue."* [81]

Many scientists, including Boyle, Newton and Herschel, attempted to identify the active reagent of the coatli plant responsible for the mystical blue colour and the phenomenon behind it for almost three centuries [82]. Robert Boyle (1664) investigated the blue colour phenomenon in great detail. He noted that after several infusions, the coatli wood lost its ability to produce blue color in water and determined it was due to the effect of some "*essential salt*" in the wood. Boyle also documented that by adding acidic solutions the blue color disappeared, whereas the addition of base returned the blue colour [83]. In 1915, extremely fluorescent glucosyl-hydroxichalcones were isolated from *Eynsemhardtia polystachia* (another member of the Mexican coatli plant) to have anti-inflammatory effects[84]. Finally, Acuña *et al*. (2009) discovered that the original blue emission described by Aztec people was due to the cyclization process of coatline B compound under a slightly alkaline condition with a maximum emission wavelength at 466 nm and strong

quantum yield of 0.8, an analogous yield to what is known about fluorescein. A very similar conversion is observed in naturally occurring catecholamines such as dopamine in slightly basic conditions [82,85].

Sunstone

Vincenzo Casciarolo, an Italian pioneer, discovered in 1603 that after baking a specific type of stone a purple-blue light was emitted. He named the stone *lapis solaris* (sunstone). This discovery created a debate between scientists and philosophers [80]. Galileo, famous Italian scientist, described the emission of light from the sunstone as:

> *"It must be explained how it happens that the light is conceived into the stone, and is given back after some time, as in childbirth."* [81]

The phenomenon of the purple-blue light in the sunstone was likely due to the phosphorescence of barium sulfate salt.

Dispersion

In 1833, David Brewster observed the production of a red light when a white light passed through an alcoholic solution of fresh leaves. Brewster thought the effect was due to the "*dispersion*" of light. In fact, the red light was the emission of chlorophyll fluorescence [80].

Phosphoroscope

Edmond Becquerel built the first phosphoroscope in 1842 and measured the phosphorescence decay time of calcium phosphate. He reported that the emission of phosphorescence followed at a wavelength longer than the ultraviolet light [81].

Epibolic dispersion

John Herschel published the first observation of fluorescence in quinine sulfate solutions in 1845. In his paper "*On a Case of Superficial Colour presented by a homogenous liquid internally colourless.*", Herschel named the phenomenon as "*epibolic dispersion*" [86].

Beautiful celestial blue colour

George Gabriel Stokes published his results in a response to John Herschel in more than hundred pages in a single article in 1852. Stokes described the phenomenon observed by quinine sulfate as a "*dispersive reflection*". Stokes employed a prism to disperse the sunlight. He reported that there was no effect when quinine solution was exposed to the visible range of the sunlight. Instead, "*a beautiful celestial blue colour*" appeared when the solution was exposed to the ultraviolet region of the sunlight as Stokes wrote:

> *"It was certainly a curious sight to see the tube instantaneously lighted up when plunged into the invisible rays: it was literally darkness visible. Altogether the phenomenon had something of an unearthly appearance."* [87]

In the same paper, Stokes invented the term "*fluorescence*" for the first time to describe the unknown phenomenon as:

> *"I confess I do not like this term. I am almost inclined to coin a word, and call the appearance fluorescence, from fluor-spar, as the analogous term opalescence is derived from the name of a mineral."* [87]

The term *Stokes Shift* was also named after George Stokes since he described the displacement of a fluorescence wavelength to a longer wavelength than it was excited at. Furthermore, Stokes was the first scientist to utilize fluorescence as an analytical application to detect substances in 1864. He was also the first scholar to allocate a section of his lectures to teach fluorescence at the University of Cambridge [81].

1.4 Fluorescence Spectroscopy

Fluorescence spectroscopy and spectrophotometry (*a.k.a.,* fluorimetry, fluorometry) are often used interchangeably. Spectrophotometry is the study of quantitative measurement of the spectrum and the interaction between matter and irradiated energy whereas spectroscopy is the theoretical study of light and radiation by matter [88].

Fluorescence spectroscopy is a sensitive method that measures the emitted radiations from a substance when exposed to light. The principle of fluorescence spectroscopy in the UV-visible range is based on the relaxation of an excited small molecule or macromolecule to a lower energy state (usually the ground state) through emission of a photon without a change in the electronic spin. When the initial and final states have different spin multiplicity, the phenomenon is called phosphorescence [88]. The fundamental mechanism for the processes in which the electromagnetic energy of the photon is studied can be explained by Planck's law,

$$E_{photon} = \frac{hc}{\lambda} \qquad \text{Eq. 1.1}$$

where h is Planck's constant (6.6×10^{-34} J·s), c is the speed of light in a vacuum (3.0×10^{8} m·s^{-1}), and λ is the corresponding wavelength of the incident light. The intensity of light is stated as energy per units of area per time (W·cm^{-2}), and it is inversely related to the wavelength of the incident light [89]. Considering light absorption by reagents, a thin cross-section area (σ) with a thickness of dx containing n molecules capable of absorbing light has a rate of change of light absorption proportional to the incident light intensity (I_o) and both σ and n according to the Beer-Lambert Law:

$$\frac{dI}{dx} = -I_o \sigma n \qquad \text{Eq. 1.2}$$

Further integration and rearrangements of the Beer-Lambert Law yield to the commonly used Beer-Lambert equation:

$$I_t = I_o 10^{-\varepsilon \ell C} \quad \text{Eq. 1.3}$$

where I_t is the transmitted intensity, ε is the molar absorptivity (extinction coefficient) of species at a specific wavelength, ℓ is the path length of a cuvette cell, and C is the molar concentration of species. The product of $(\varepsilon \ell C)$ is often denoted as the optical density, light absorbance, or absorption in arbitrary units (a.u.).

The energy of UV-visible light can be absorbed by molecules through one or multiple paths: *sigma bonds*, *non-bonding electrons*, and π *systems* [89,90]. As illustrated in Figure 1.5, the absorption of light reduces the electronic population in the lowest singlet energy state (S_0) and surges the electronic population to next excited states (S_1, S_2…). After this excitation, an extremely fast vibrational relaxation will occur in femtosecond timescales, which is often detectable using infrared spectroscopy. Then decay of S_1 to S_0 occurs through one of the four available paths [91,92]:

1. **Radiative transitions**, which is the loss of excess electronic energy through the emission of photons. This radiative transition is referred to as *fluorescence*.
2. **Intersystem crossing**, which involves with a change in the spin of the electronic state from singlet to triplet (T_1). This transition occurs in μs to seconds and is called *phosphorescence*.
3. **Internal conversion**, or non-radiative decay, which involves with a high vibrational relaxation through bond conversion or isomerization.
4. **Collisional quenching**, which involves with the collision of the excited compound to other species capable of absorbing energy in the same dipole moment as with the excited state.

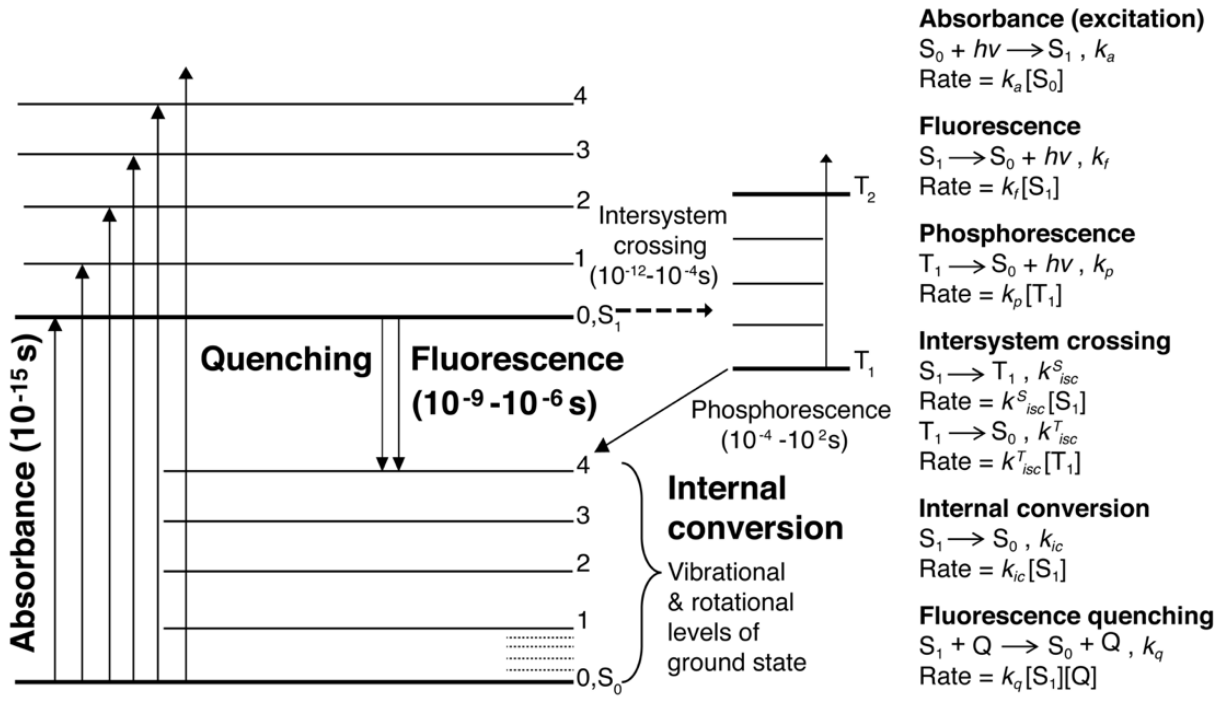

Figure 1.5 Illustration of a Jablonski Diagram depicting an example of possible excitation and relation pathways and rate expressions. Dotted lines show rotational levels. For instance, the UV light irradiations can excite a ligand from its singlet ground state (S_0) to the singlet excited states (S_1, S_2) in femtosecond timescale. The surplus excited energy from *non-radiative* relaxation processes instantly goes through *radiative* processes resulting fluorescence in ns-μs timescale, or phosphorescence in milliseconds to minutes at longer wavelengths, or lower energy states, than the excitation light [94,225].

The decay of energy in each of these four processes follows with a first-order kinetic rate expression as illustrated in Figure 1.5. Since under constant irradiation the concentration of intermediate will not change, the differential rate expression for S_1 can be studied applying the steady-state approximation. Hence, the technique is called steady state fluorometry, by which the fluorescence intensity (F_λ) at a specific emission wavelength (λ_{em}) is quantified as:

$$F_\lambda = (\ln 10)\mathrm{I_o}\varepsilon_\lambda \ell \mathrm{C}\Phi_f \mathrm{k} \qquad \text{Eq. 1.4}$$

where Φ_f is the fluorescence quantum yield (quantum efficiency) of the compound, and k is the proportionality constant [89]. In dilute solutions where compounds are *equally* exposed to I_o

irradiations, fluorescence is *linearly* proportional to concentration. However, fluorescence emissions become logarithmic and eventually remain unchanged when the concentration of fluorophore or the excitation intensity is extremely increased. This is known as the maximum threshold of the Beer-Lambert equation because the mathematical limit of fluorescence intensity (F_λ) in Eq. 1.4 as concentration approaches infinity is equal to a constant number [88,93].

1.4.1 Fluorescence polarization

Fluorescence emission from a dynamic fluorophore can become linearly polarized when it is excited with the plane-polarized irradiations. The level and the angle of emission polarization depends on the molecular size, motion and steric hinderance of the fluorophore in the solution [94]. This change in the plane-polarized fluorescence is measured and characterized by fluorescence polarization (P):

$$\mathrm{P} = \frac{\mathrm{I}_{vv} - \mathrm{I}_{vh}}{\mathrm{I}_{vv} + G\mathrm{I}_{vh}} \qquad \text{Eq. 1.5}$$

where I_{vv} and I_{vh} are the fluorescence intensities detected upon vertical (v) and horizontal (h) excitations under parallel (vv) and perpendicular (vh) planes of polarization, and G determines the instrumental grating factor ($\mathrm{I}_{vh}/\mathrm{I}_{hh}$). Similarly, fluorescence anisotropy (r) is defined as the ratio of the polarized component to the total intensity of light to avoid having negative values for the analysis [95,96].

These two polarization techniques differ from linear or circular dichroism (CD) spectroscopy because dichroism employs *transmitted* light based on the inherent chirality of a reagent whereas fluorescence polarization and anisotropy use *emitted* light, which depends on the isotropic nature of light, local environment, and molecular dynamics of the analyte [97,98].

1.4.2 Photoisomerization analysis

Investigations into photoisomerization reaction mechanisms have a long history in the theoretical and experimental studies. For instance, the *cis-trans* isomerization of retinal, a polyene molecule, attached to bacteriorhodopsin proteins controls a phototransduction cascade, where the absorption of light is converted to an electrical signal [99]. Similar to retinal, stilbene (1,2-diphenylethene) molecule has photoisomerization property with an additional property of being a fluorophore. The *cis-trans* photoisomerization of stilbene (1,2-diphenylethene) fluorophore was first introduced in 1931, and since then biochemical applications of stilbene photoisomerization have been widely recognized. For instance, stilbene is used in radiation detectors, gamma spectroscopy, and fluorescence enhancers [100].

Advantages of stilbene include chemical and biological stability, low toxicity, synthetic robustness, high photochemical sensitivity, prompt and measurable radiation response, and easy regeneration. Though, the drawback is that stilbene is insoluble in aqueous solutions. Thus, water soluble stilbene derivatives like stilbene-maleimides, 4-acetamido-4'-isothiocyano-2,2'-disulfonic stilbene (SITS), or 4,4'-diisothiocyano-2,2'-disulfonic stilbene (DIDS) are generally used in biochemical experiments [101,102]. Utilization of stilbene derivative, SITS, in aptamer studies was first introduced by Zhou *et al.* using the malachite green RNA aptamer in the development of a photochrome aptamer switch assay (PHASA), where the aptamer-SITS was excited at 340 nm in a buffered aqueous solution and the fluorescence emission kinetics were detected at 428 nm [103]. As it will be discussed in Chapter 5, the cocaine-binding aptamer is the second aptamer model to report aptasensor applications with SITS.

1.5 Ligands

Cocaine and quinine were used for fluorometry assays presented in subsequent sections because they are intrinsically fluorescent, and their binding analyses with the cocaine-binding aptamer have been already confirmed using non-fluorometry techniques such as NMR and ITC [64,104]. Some background information about these two ligands is provided in this section.

1.5.1 Cocaine

Benzoylmethylecgonine (cocaine) is a tropane alkaloid that is extracted from leaves of coca plant. Cocaine is structurally similar to atropine and pyrrolidine alkaloids (*i.e.,* nicotine), and it is a widely abused psychostimulant drug that has sympathomimetic properties [105,106]. Sympathomimetic drugs are used to treat the cardiac arrest and low blood pressure, as they are stimulant compounds mimicking the effects of endogenous agonists of the sympathetic nervous system (*i.e.,* increased heart rate, force of cardiac contraction, and blood pressure). The primary endogenous agonists of the sympathetic nervous system are the catecholamines and phenylamine (*e.g.,* dopamine, serotonin, adrenalin, epinephrin), which function as both neurotransmitters and hormones [107].

Cocaine is used recreationally to increase alertness, relieve fatigue, and increase self-confidence and is abused due to its intense euphoric effects. Cocaine is among the most abused illicit drugs, used annually by 0.3–0.4% of the world population aged 15–64 years [108]. Street samples of cocaine include cocaine sulfate and cocaine hydrochloride salts and may be mixed with heroin, tobacco, marijuana, and/or levamisole to increase psycho-stimulative effects or illicit profits [109,110]. Cocaine is a thermolabile compound and degrades to the formation of the

metabolite anhydroecgonine methyl ester at 65 °C or above. All forms of cocaine salts and metabolites such as benzoylecgonine are neurotoxic due to their lipophilic property [111–113].

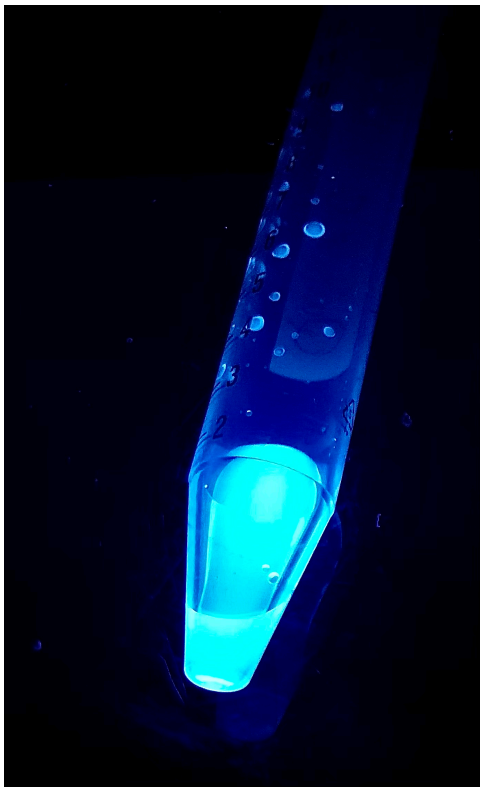

Figure 1.6 Blue emission of quinine. Shown photo demonstrates fluorescence emission of a diluted quinine hemisulfate sample (10 µM) in a mild acidic solution of sulfuric acid at room temperature under UV light (long wavelength range, 360 nm).

1.5.2 Quinine

Quinine ([-]-6'-Methoxycinchonidine) belongs to the naturally occurring β-carboline cinchona alkaloid group, which was originally extracted from the bark of cinchona trees. Quinine is a stereoisomer of quinidine and has been used for the treatment of malaria since 1633. Quinine is inexpensive and non-illicit compared to regulated cocaine compound and has been used for many

years to add a bitter flavour in some soft alcoholic beverages (at a concentration of ~0.2 mM) and to a small extent in flour confectionery. Most importantly, quinine has fluorescence properties and was the first standard fluorophore reported in 1845 (Figure 1.6) [86,114]. Like quinine, other quinidine alkaloid antimalaria drugs such as chloroquine, mefloquine, amodiaquine, and primaquine have similar intrinsic fluorescence properties [115] that are discussed in Chapter 2 for the development of an intrinsic fluorescence detection method for the aptamer-target binding analyses.

It is worth noting that the inherent fluorescence properties of DNA and RNA aptamers differ from the quinine's fluorescence properties. Nucleic acids absorb UV light at 260 nm and emit weak fluorescence at ~327 nm [115,116]. This difference in intrinsic fluorescence is employed to develop a fluorimetry method in order to quantify binding affinity of ligands precisely and conveniently (*i.e.,* quinine, cocaine, methylene blue, ochratoxin A, antimalaria drugs with DNA aptamer). This intrinsic fluorescence method is beneficial since it overcomes the sensitivity limitations associated with non-fluorescence techniques like NMR and ITC.

1.6 Thesis Project

The exploitation of aptamers in biosensing technology is expanding rapidly due to the ease of aptamer selection with high sensitivity and often great specificity of target recognition. The structural flexibility and thermal stability natures of nucleic acids enable aptamers to be utilized for sensing purposes. However, there is little known about the function, binding mechanism, or structural elucidation of aptamers. The general goal of this study is to gain insight about how aptamers interact with their selected ligands.

To achieve my objectives, I utilize available biophysical techniques including steady-state fluorescence, emission kinetics decay, and fluorescence anisotropy to develop a detection method for aptamer-ligand binding analyses based on the inherent fluorescence of ligands. I intend to employ the intrinsic fluorescence of ligands to develop a differential fluorometry thermal denaturation assay. I use the cocaine-binding aptamer as a model system to analyze the characterization of interactions between the cocaine-binding aptamer variants and the small molecule targets.

The cocaine-binding aptamer was originally selected to distinguish cocaine molecules from cocaine metabolites in biological solutions though the aptamer's alternative affinity for quinidine alkaloids and some other ligands have enabled this aptamer to be employed as an outstanding experimental three-way junction DNA model. Furthermore, I aim to exploit the photo-isomerization property of stilbene compound to study the ligand-induced binding mechanism of the cocaine-binding aptamer and demonstrate some analytical applications of the photochrome aptamer switch assay for the detection of artemisinin, an antimalaria drug, and levamisole, which is a hazardous compound added in illicit cocaine samples.

The work postulated in this dissertation coupled with my collaborative work provide valuable insight into the function and structure of the studied aptamers, and I hope this will be a step-up move for future studies of structural elucidation of aptamers.

Chapter 2: Fluorometry protocol for aptamer binding analysis

2.1 Preface

Presented work in this chapter has been submitted for a peer-reviewed publication as a method protocol article [117]:

- **Shoara, A.A.,** and Johnson, P.E. (2022) Fluorometry Studies of Aptamers That Bind Intrinsically Fluorescent Ligands: Techniques, Obstacles, and Optimizations. *Aptamers* (*Submitted*).

2.2 Introduction

Common extrinsic fluorescence detection techniques with aptamers involve the addition of a fluorescent or quencher label to the aptamer. However, adding labels can affect the structure of the molecule [61]. This chapter presents a detection method for aptamer-ligand binding analysis that is based on the inherent fluorescence of the ligand. In this protocol, I describe my methods and protocols that I employed for using ligand fluorescence quenching to quantify the binding affinity of the cocaine-binding aptamer (MN4 construct; Figure 2.1) with great sensitivity, accuracy, and precision. I used quinine, cocaine, and tetracycline because they are intrinsically fluorescent ligands, and their binding and structural analyses with nucleic acid molecules have been previously studied (Figure 2.1) [58,118]. The drawback of using intrinsic fluorometry is that the ligand of interest may have weak or no intrinsic fluorescence property. Also, some extreme experimental conditions may affect the intrinsic fluorescence property of the ligand. For these instances, I utilized fluorescence anisotropy and photoisomerization properties that are independent of absolute magnitude of fluorescence intensity of ligands. These techniques are further discussed in chapters 5-6.

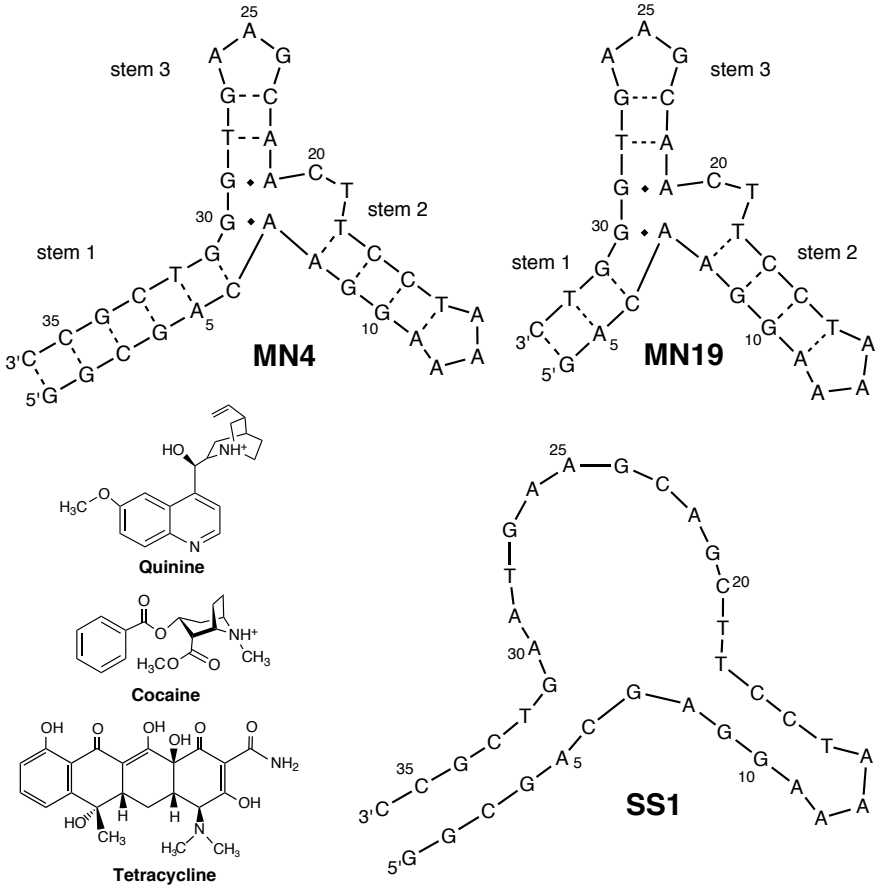

Figure 2.1 Structures of the ligands and the DNA aptamers used in this chapter. Dashed lines between nucleotides indicate Watson-Crick base pairing in the secondary structure, whereas diamonds show non-canonical the AG base pairs. Solid lines display the phosphodiester bonds in the backbone of the aptamers.

2.3 Materials and Methods

2.3.1 Instruments

Fluorescence and UV-visible procedures are performed using Agilent Cary Eclipse and Agilent Cary 100 spectrophotometers. Both spectrophotometers are equipped with xenon flash lamps and linked to separate Peltier thermostatted cell holders allowing simultaneous temperature control for multiple samples. The chemical and physical properties of cuvettes (*e.g.,* plastic or quartz) used

for experiments can impact results. Plastic cuvettes should be avoided when using an organic co-solvent and when working at high temperatures [119]. The perpendicular profile of excitation and emission beams requires the cuvette to be three- or four-windowed. DNA and RNA aptamer constructs can be purchased commercially with standard desalting purification. The cocaine-binding aptamer (Figure 2.1, MN4 and MN19) were used in this protocol. Buffer solutions were prepared using distilled deionized Milli-Q water (ddH_2O). Since the ionic strength of the solution has a quenching effect on the fluorescence, variation in experimental ionic strength could yield imprecise results. Some buffer components (*e.g.,* phosphate buffer) have fluorescence quenching effects [116]. Materials and manufacturers mentioned in this protocol are stated for transparency purposes though one can use any type or brand of analytical grade reagents.

In preparing samples for binding analysis using intrinsically fluorescent ligands, the following considerations are essential: (*i*) optimal ligand and aptamer concentrations; (*ii*) choice of buffer and ionic strength; (*iii*) organic solvent choice, only if necessary, to dissolve the ligand. To analyze the dissociation constant (K_d) of a ligand aptamer complex, the detectable ligand must be placed in the cell. To ensure the ligand is fully saturated with the aptamer, the maximum concentration of aptamer is quantified using:

$$X_{A\bullet L} = [A]^n/(K_d{}^n + [A]^n) \qquad \text{Eq. 2.1}$$

where $X_{A\bullet L}$ is the fraction of bound complex, [A] is the starting aptamer concentration and n is the number of binding sites. A suitable starting concentration for a ligand depends on the fluorescence quantum yield of the ligand and the threshold of detection are further discussed below.

The aptamer is exchanged three times against 1 M NaCl using Amicon-type centrifugal concentration to remove any substances bound to the aptamer from synthesis and then exchanged 4-6 times against ddH_2O. The stock aptamer concentration should be at least 50 folds higher than the aptamer concentration required to saturate the ligand binding. Prior to the binding analysis, the DNA or RNA aptamer constructs should be annealed to favour intermolecular folding. The unbound aptamer samples are incubated in a water bath at 95 °C for 3 min and then transferred in an ice water bath for 5-10 min for fast annealing. For split aptamers, the different strands should be fast annealed separately. To have low fluorescence quenching interference, it is preferred to degas the ligand and aptamer solutions using sonication or inert gas purging methods [120].

2.3.2 Experimental Setup

In a fluorescence binding experiment, either the ligand is intrinsically fluorescent, or the aptamer is labelled with a fluorescent dye. To obtain the K_d value of a ligand aptamer complex, the fluorescent species must be placed in the cell, and the total volume of the cell should not be increased by more than 10% of the initial volume. For instance, the ligand must be placed in the cell and the aptamer in the titrant solution if the intrinsic fluorescence of the ligand is to be utilized. Additionally, the effect of temperature, pH and solvent on the binding affinity should be confirmed from literature values or optimized experimentally (Figure 2.2a).

The effect of solvent on the fluorophore may be challenging as some nonpolar ligands are only soluble in mixtures containing an organic solvent such as dimethyl sulfoxide (DMSO) or acetonitrile (ACN). In this case, light absorptivity or fluorescence properties of the organic solvent should be accounted for. Instrumental parameters such as cuvettes, photomultiplier tube (PMT)

voltage, excitation and emission slit widths and scan rates should be optimized and kept unchanged to yield the highest sensitivity, accuracy, and precision of the results (Figure 2.3).

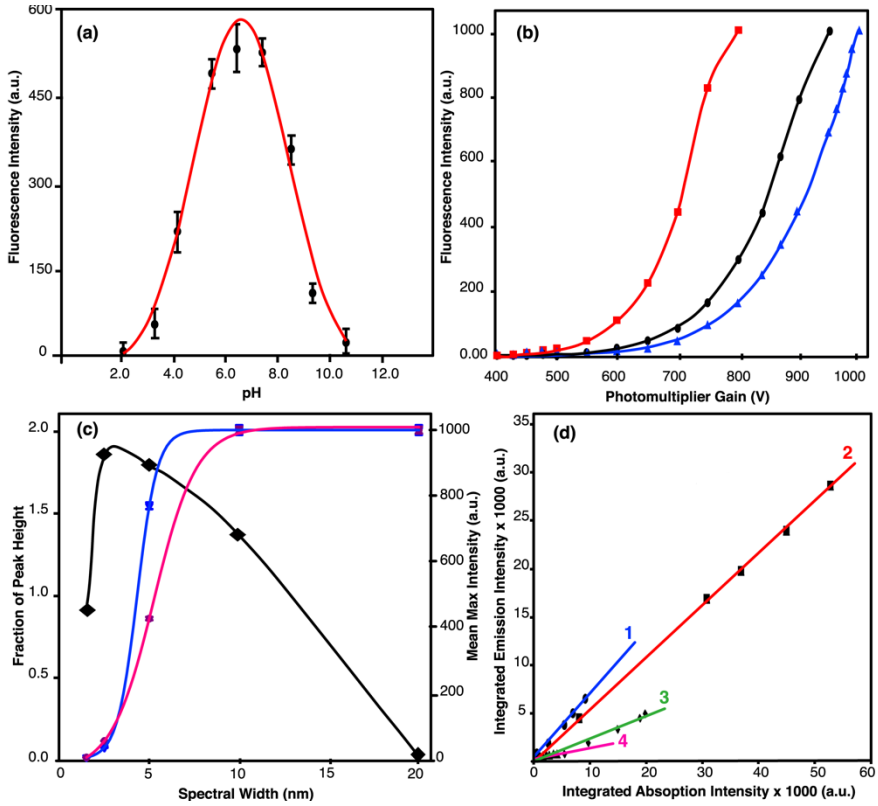

Figure 2.2 (**a**) The effect of pH change on the fluorescence emission of quinine at 23 °C. Fluorescence intensities were fit to a Gaussian curve. Inflection points obtained from the fitted curve (4.83 and 8.49) correspond to pKa values of quinine. The fitted peak height at pH 6.6 signifies the optimum pH condition (pH 6.6 ± 1) for fluorescence studies of quinine ligand. (**b**) displays the exponential effect of photomultiplier change on the fluorescence intensity of quinine at 23 °C. Data acquired at different concentrations of quinine, 0.5 µM (red), 0.2 µM (black), and 0.1 µM (blue). (**c**) shows how the fraction of peak height (black line, left vertical axis) changes with effective spectral slit width. Right vertical axis shows how the maximum fluorescence intensity changes with adjusting instrumental bandwidth as ligand concentration and other experimental conditions remain unchanged. Blue line denotes excitation at 235 nm and fuchsia line represents excitation at 330 nm (**d**) displays a comparative analysis of quantum yield measurements. Integrated emission intensities are plotted against integrated absorbance intensities and analyzed using a linear regression method. Quinine excited at 330 nm (Blue line 1: slope = 0.599, R^2 = 0.9987), quinine excited at 235 nm (Red line 2: slope = 0.537, R^2 = 0.9997), cocaine excited at 232 nm (Green line 3: slope = 0.254, R^2 = 0.9996), and MN4 excited at 260 nm (Fuchsia line 4: slope = 0.037, R^2 = 0.9994).

2.3.3 Determination of the threshold of detection

To evaluate the precision and accuracy of acquired fluorescence data, it is essential to test the linearity of emission intensities versus ligand concentration by determining the threshold of detection at the lowest and highest concentrations of the ligand. This test is performed to verify the instrument is capable of measuring emission intensities within the range of experimental concentrations [121].

1. Prepare a fresh stock solution of the ligand in buffer. Note the ligand concentration should be at least 10-fold greater than the highest concentration of the ligand in the experimental design.

2. For each trial, prepare at least 5 ligand samples with different concentrations. The minimum and maximum concentrations should cover the ligand concentration range in the experiment.

3. Using a UV-Vis spectrophotometer, identify the maximum absorbance wavelength of the ligand noting that maximum excitation wavelength of a fluorophore corresponds to its maximum UV-Vis absorption under the same experimental conditions.

4. Using the fluorimeter perform an emission scan at a fixed excitation wavelength at 600 nm/min, 0.10 s averaging time, 1.00 nm emission wavelength intervals, and 400-600 volts PMT.

5. The obtained maximum emission intensities are plotted as a function of ligand concentration and analyzed to a linear fit. The signal threshold for concentration limit of detection (C_{LoD}) and limit of quantification (C_{LoQ}) are determined using:

$$C_{LoD} = 3s/m \qquad \text{Eq. 2.2}$$

$$C_{LoQ} = 10\ s/m \qquad \text{Eq. 2.3}$$

where s is the residual sum of the vertical intercept (y-intercept) and m is the slope [122,123]. Two examples of the threshold of detection determination for cocaine and quinine are demonstrated in Figure 2.4cd.

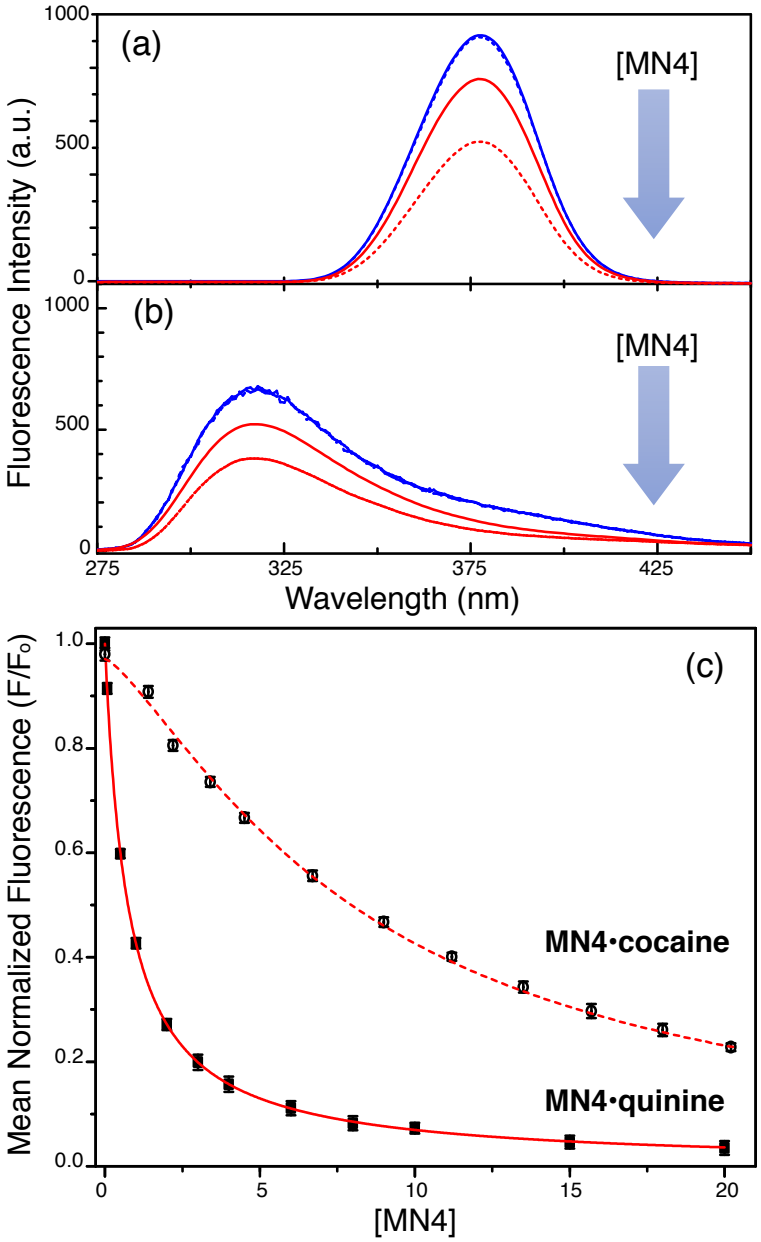

Figure 2.3 The fluorescence emission spectra of quinine (**a**) and cocaine (**b**) titrated with the MN4 aptamer. Fluorescence scans were carried out in PBS (pH 7.4) at 23 °C. Aptamer aliquots quenched intrinsic fluorescence of 6.0 µM quinine excited at 234 nm and 4.8 µM cocaine excited at 232 nm. (**c**) The corrected and normalized relative fraction fluorescence for each ligand is expressed on the y-axis. F_o and F are inner-filter corrected emission maxima in the absence and presence of the MN4 aptamer, respectively. Each data point signifies an average of 3-6 experiments. Error bars represent one standard deviation. The K_d values were quantified as (0.75 ± 0.01) µM and (7.7 ± 0.1) µM for MN4•quinine and MN4•cocaine titrations, respectively, using Eq. 2.5.

2.3.4 Photomultiplier optimization

To ensure the best signal-to-noise ratio (S/N), the photomultiplier tube (PMT) voltage variation should be optimized. PMT gain values higher than 800 V reduces the S/N ratio.

1. Set the fluorescence excitation scan mode at the known emission wavelength of the ligand (*i.e.*, 380 nm for cocaine and quinine).

2. Using a buffer-only sample perform fluorescence scans as a negative control.

3. From a concentrated solution of ligand, titrate the ligand into buffer until the intensity of peaks are observed at slightly lower than 1000 a.u. counts.

4. Keeping other parameters constant, obtain fluorescence scans as a function of PMT voltage from 1000 V to 400 V. Repeat this step to at least 10 different PMT voltage points. Plot emission intensities against PMT values.

5. The observed fluorescence intensity depends on the PMT voltage and excitation wavelength. Figure 2.2b represents an exponential relationship ($F = 2^{(PMT/100)}$) between the fluorescence intensity of quinine as a function of PMT voltage at three different quinine concentration values (0.1-0.5 μM) [124,125]. The optimal PMT is a voltage at which the intensity versus PMT plot holds a linear profile for all ligands in one experiment.

2.3.5 Fluorometer slit width optimization

To have an accurate and precise resolution of fluorescence detection, a monochromatic excitation and emission is preferred. When the irradiated photons pass through monochromator slits, a Gaussian distribution emerges where the spectral bandwidth (SBW) is controlled by the instrument as the width at 50% of the maximum *peak intensity* (commonly set at 2-10 nm). The effective spectral slit width (ESS), the wavelength range covering wider than half of the maximum peak, is

often used for SBW, interchangeably. The natural bandwidth (NBW) is the width of an experimentally detected peak at half of the *peak height*. The ratio of SBW/NBW should equal or be less than 0.100 to have a minimum of 99.5% accuracy of measurement. This ratio shows how accurately the fluorometry detects the true height of the emitted peak.

Most scientific spectrophotometers have adjustable slit widths for both excitation and emission monochromators to optimize the instrument for the best resolution [126]. The high ratio of SBW/NBW generates overlapped peaks and adds stray light rays to the excitation and emission. As a result, a pronounced deviation from the Beer-Lambert law and wider peaks are observed. On the other hand, the low SBW/NBW ratio increases the resolution with a trade-off for reduced sensitivity. The spectrophotometer is expected to resolve 99% of the actual emitted light when the SBW/NBW ratio is 0.125 [126–128]. Figure 2.2c presents optimization of slit widths for the fluorescence analysis of MN4 and quinine.

2.3.6 Determination of quantum yield

The fluorescence quantum yield (Φ_f) is an intrinsic property of a fluorophore and denotes as the ratio of total emitted photons by the total absorbed photons while photophysical brightness (B) is quantified as the product of the quantum yield and the molar absorption coefficient of the fluorophore at the excitation wavelength [88,129].

Two methods are available in the literature for relative quantum yield analyses: (*i*) single-point, where the emission intensities from a fluorescent ligand and a reference pair at identical concentration and buffer conditions are measured, and (*ii*) comparative methods. The single-point

method estimates Φ_f quickly though it is not considered as an accurate method [130,131]. Here, we show a robust comparative method of quantum yield measurement (Figure 2.2d).

Table 2.1 Commonly used fluorescence quantum yield values of reference fluorophores in standard solutions.

Standard compound	Φ_R *(%)*	*Excitation wavelength (nm)*	*Conditions*
Fluorescein	95	496	0.1 N NaOH, 22 °C
Rhodamine 101	100	450	Ethanol, 25 °C
Rhodamine 6G	95	488	Water, 25 °C
Rhodamine B	31	514	Water, 25 °C
Quinine sulfate	58	350	0.1 N H_2SO_4, 22 °C
Cyanine 3	4	540	PBS
Cyanine 5	27	620	PBS

1. Prepare at least four samples of the experimental ligand in the desired buffer conditions and four samples of a reference fluorophore solution.

2. Using excitation scan mode, measure fluorescence emission at the excitation wavelength.

3. Plot the integrated fluorescence intensities against the integrated absorbance intensities and perform a linear regression analysis.

4. Repeat steps 1-3 for a reference ligand with known fluorescence quantum yield. Table 2.1 lists commonly used quantum yield standards [88,129].

5. The obtained linear slope for the analyte and reference ligands (denoted with subscript R) are compared to determine the fluorescence quantum yield using:

$$\Phi_f = \Phi_R \, (m/m_R)(\eta^2/\eta^2_R) \qquad \text{Eq. 2.4}$$

where *m* denotes linear slope, and η is refractive index of the solutions [88,129–131].

2.3.7 Binding affinity determination

To analyze the binding affinities of an equimolar ligand-aptamer complex, the most valid K_d quantification is found using the quadratic function (Eq. 2.5). I fitted the fluorescence isotherms to a nonlinear regression model, which I defined from the quadratic function and developed applying OriginPro script:

$$F = F_1 + (F_2 - F_1)\frac{K_d^n}{K_d^n + x^n} \qquad \text{Eq. 2.5}$$

where F is the dependent variable (fluorescence intensity of the ligand), x is the independent variable (titrant aptamer concentration), n denotes the number of binding events, and F_1 and F_2 are the horizontal and vertical asymptotes, respectively [104,132].

2.4 Results and Discussions

To quantify the K_d value of a ligand-aptamer titration experiment, the maximum emission intensities (or integrated emission peak values) for each titration point is collected as a function of aptamer concentration. The acquired data should be corrected for any possible light scattering noise or inner-filter effect (described below). As demonstrated in Figure 2.3a-c, the corrected fluorescence intensities are normalized to have a consistent range of zero to 1 in all experimental batches, plotted against the aptamer concentration, and fitted to Eq. 2.5. For the errors in the K_d, one can either take the standard deviation (SD) of the fitted average values or analyze each trial individually and report the average $K_d \pm$ experimental SD.

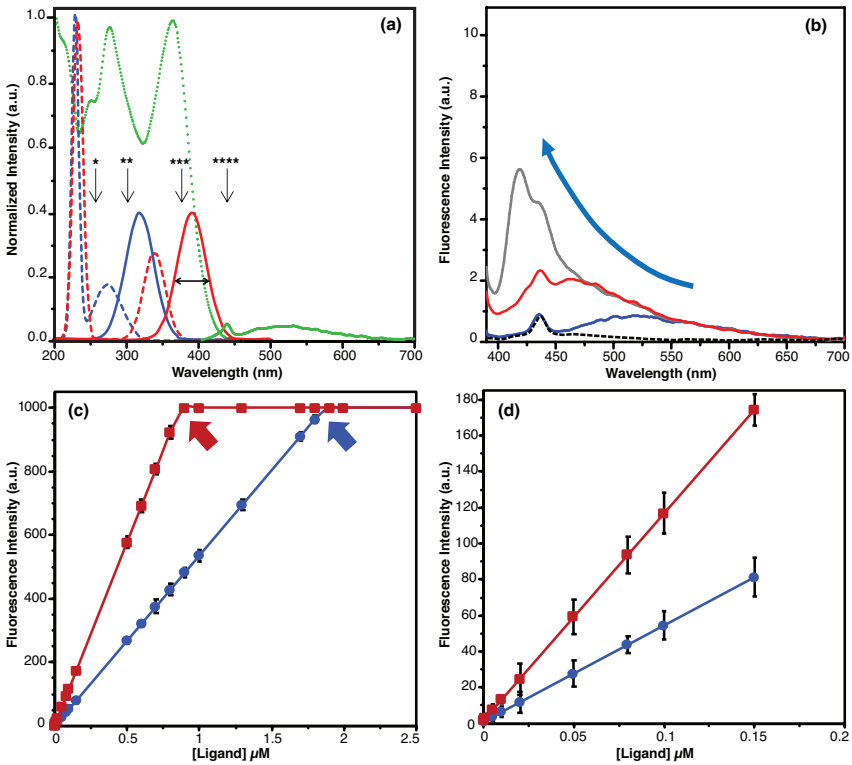

Figure 2.4 The effect of light scattering and detection limit on the observed fluorescence emission of ligands: (**a**) shows excitation (dashed lines) and emission (solid lines) spectra of cocaine (red), quinine (blue), and tetracycline (green) in PBS at 25 °C. Asterisks with arrows denotes anticipated Raman scattering signals in aqueous solutions when excited at 230-235 nm (*), 275 nm (**), 335 nm (***), and 360-365 nm (****). Black arrow illustrates NBW of 61 nm at 5 nm SBW. The SBW/NBW ratio is 0.082 at 235 nm excitation. (**b**) shows how light scattering can negatively influence fluorescence emission of tetracycline ligand titrating with MN4. As tetracycline interacts with the aptamer, the emission intensities are enhanced though the emission is near scattering light (blue arrow) observed at ~440 nm in a blank PBS sample (black dashed), 0.9 μM tetracycline in PBS (blue), 0.9 μM tetracycline titrated with 1 μM MN4 (red), and 5 μM MN4 (grey). (**c**) demonstrates an example of the threshold of detection comparison for cocaine (blue) and quinine (red) in PBS at 25 °C. Arrows show the maximum thresholds of detection. (**d**) exhibits a zoomed view of zero to 0.2 μM ligand concentration from data in (**c**) to show the minimum thresholds of detection. The fitted linear regression values quantified as $y = 543.9x + 98.3$ for cocaine (blue) and $y = 1150.7x + 973.5$ for quinine (red). Residual sums of the vertical intercept (y-intercept) values are acquired as ±109.9 for cocaine (blue) and ±103.6 for quinine (red). The minimum thresholds of detection are calculated as $\frac{3\times109.9}{543.9} = 0.6$ μM for cocaine and $\frac{3\times103.6}{1150.7} =$ 0.3 μM for quinine using Eq. 2.2.

To characterize the fluorescence properties of the examined ligand, it is essential to test the effect of change in the pH and ionic strength conditions of the experimental design. Any considerable change in pH, ionic strength, viscosity or temperature that influences the quantum yield of a fluorophore can consequently alter the fluorescence detection [119]. To confirm the pH and ionic strength conditions, where highest sensitivity of the fluorescence is gained, steady-state fluorescence scans for 7-10 ligand samples are performed in preferred buffer conditions under variable pH range of approximately 2-11. Some ligands exist as diprotonated compounds. For instance, quinine has one aromatic and one aliphatic group offering two pKa values of 4.2 and 8.3, respectively [133]. In mild to strong acidic solutions (pH lower than 4.0), quinine is fully protonated, and its fluorescence is quenched as the excited state energy is converted internally. Also, the intensity of quinine fluorescence quenches as the ionic strength is increased, or pH is higher than 9. The acquired pKa values (4.83 and 8.49) agreed with available pKa values of quinine using alternative techniques (Figure 2.2a).

To optimize the excitation and emission slit widths, one should note that the signal resolution decreases with the spectral bandwidth increase. Figure 2.4a shows how the ratio of SBW/NBW was quantified 0.082 at 5 nm slit width at 235 nm excitation wavelength and 10 nm at 335 nm excitation wavelength. Obtaining a ratio below 0.1 signifies an accurate measurement (>99.5%) at constant temperature and PMT voltage.

2.5 Critical Parameters and Troubleshooting

It is possible that detected emission counts are higher than the maximum threshold of 1000 a.u. To resolve this issue, changing one or a combination of the following parameters would be useful:

reducing ligand concentration, length of the light path, PMT voltage, excitation (or both) slit widths, or increasing the temperature is advised.

In case the fluorescence intensity of the least concentrated ligand sample is found to be as low as the scatting intensities of the buffer, increasing the length of the light path, excitation (or both) slit widths, or reducing the temperature can resolve the problem. The optimal bandwidth for an analysis should not necessarily be 1.0 nm though a narrow spectral bandwidth improves the resolution of peaks that are emitted close to each other. If the analyte has low quantum yield, one or a combination of the following adjustments enhances the detection: increasing the excitation slit width, reducing the length of light path, reducing temperature, or the ionic strength. As shown in Figure 2.2c for quinine emission, the fraction of peak height (resolution) is reduced with the spectral bandwidth increasing from 2.5 nm.

Quantum yield is an intrinsic property of a ligand. Thus, Φ_f is independent of the ligand concentration or instrument parameters [129]. However, the ligand concentration needs to be within the linear range of Beer-Lambert law and the instrument parameters should be kept constant throughout the experiment. Any significant change in the pH, ionic strength, and refractive index (η) consequently alters Φ_f. Figure 2.2d illustrates a comparative analysis of quantum yield measurements for quinine, cocaine and the MN4 aptamer.

The desired experimental temperature is determined by the aptamer stability, ligand thermolability, and instrument limits. It is worth noting that binding affinities are temperature

dependent [134]. The temperature can be set between -10 °C to 120 °C with 0.1 °C resolution and cell temperature variation of ± 0.05 °C.

The total number of sample titrations should be uniformly distributed across the concentration range studied to get a precise binding analysis. If one-binding process is anticipated for the aptamer-ligand complex, the titration volume should be chosen such that aptamer to ligand equimolar ratio reaches in the middle of the binding titration. Considering nucleotides are weakly fluorescent, measuring the background fluorescence signals from the titration of the aptamer into a blank buffer is essential to confirm the changes in the observed fluorescence was specifically due to ligand-aptamer interactions and not scattering effects (Figure 2.4b). If the ligand is excited at any wavelengths below ~330 nm, where nucleotides absorb UV light, the loss of excitation and emission photons due to the inner-filter effect should be compensated as:

$$F = F_{obs}[10^{(A_{ex}+A_{em})\ell/2}] \qquad \text{Eq. 2.6}$$

where F is the corrected fluorescence intensity, F_{obs} is the observed intensity in the absence of the inner-filter effect, A_{ex} and A_{em} are the absorbance values of the aptamer, or any other light absorbing components, at the excitation and emission wavelengths of the ligand, respectively, and ℓ is the length of the light path [104]. Additionally, performing a negative control experiment using a non-binding aptamer with comparable extinction coefficient as the analyzed aptamer is highly recommended.

Preliminary data analysis can be performed with the software supplied by the manufacturer (*i.e.,* Eclipse-Bio) or exported to advanced data analysis software packages (*e.g.,* MATLAB, OriginPro, SigmaPlot, GraphPad). An important setback that can be experienced at micro- or

nanomolar concentration scales of ligands is the presence of light scattering spikes in the baseline. Main scattering signals accounted in fluorescence spectrometry of solutions are (*i*) the first and second orders Rayleigh, (*ii*) Tyndall, (*iii*) Raman, which appear depending on the excitation wavelength. Tyndall scattering is caused by solid particle residues (*e.g.,* dust), which can be eliminated applying a nanopore membrane filtration. The Rayleigh scattering signals appear at the same excitation wavelength and 2-times the excitation wavelength. The Raman scattering wavelength of aqueous solutions is attributed to the symmetrical vibrational energy [135]. The mathematical relationship between the excitation wavelength (λ_{ex}) and the anticipated Raman scattering signal (λ_R) is expressed as:

$$1/\lambda_R = 1/\lambda_{ex} - 3400\ cm^{-1} \qquad \text{Eq. 2.7}$$

To eliminate the effect of scattering signals, one can change the excitation wavelength to a lower range of excitable wavelengths and adjust the emission scan wavelength range outside the scattering signal. Alternatively, one can subtract the fluorescence intensity of a blank buffer from experimental samples or normalize the observed fluorescence intensity with respect to scattering signals [136]. Figure 2.4ab shows anticipated scattering signals with respect to fluorescence emissions of quinine, cocaine, and tetracycline titrating with the MN4 aptamer. More complicated binding models such as two-site independent binding, sequential binding, and Förster resonance energy transfer (FRET) can also be analyzed upon modification of aptamer. Data fitting to more complicated models are also possible though not discussed in this chapter [137–139].

Chapter 3: Label-free fluorometry studies of aptamers that bind intrinsically fluorescent ligands

3.1 Preface

Presented work in this chapter has been published in the articles listed below [104,140]:

- **Shoara, A.A.**, Slavkovic, S., Donaldson, L.W., and Johnson, P.E. (2017) Analysis of the interaction between the cocaine-binding aptamer and its ligands using fluorescence spectroscopy. *Can. J. Chem.* 95(12): 1253-1260.

- Van Riesen, A.J., Le, J., Slavkovic, S., Churcher, Z.R., **Shoara**, **A.A.**, Johnson, P.E., and Manderville, R.A. (2021) Visible Fluorescent Light-up Probe for DNA Three-Way Junctions Provides Host–Guest Biosensing Applications, *ACS Appl. Bio Mater*. 4, 6732-6741.

3.2 Introduction

The cocaine-binding aptamer model has become a widely employed system for the development of aptamer-based biosensors. The different sensors, utilizing this aptamer, report ligand binding using a variety of methods including color change, electric and fluorescent tag outputs [61–65,141–153]. In the first part of this chapter, I present how I utilized the intrinsic fluorescence of ligands to gain new insights about the binding mechanisms of these fluorescent ligands with the cocaine-binding aptamer. In the second part, I use a merocyanine containing probe to study how intrinsically fluorescence ligands bind the cocaine-binding aptamer. Quantification of observed fluorescence quenching or enhancement provides a sensitive method to measure the binding affinity using small amounts of sample [154]. These observations coupled with the Stokes shifts in the emission spectra indicate whether the ligands interact with the aptamer through base stacking, groove binding, or base intercalation [155].

As discussed in Section 1.2, DNA three-way junctions (3WJs) consist of a Y-shaped or T-shaped hydrophobic branch point linking three double-stranded stems, and are considered as

susceptible targets for cancer treatment (*e.g.*, HeLa and human breast MCF-7 cancer cells) [156,157]. They are also important building blocks for the construction of DNA nanostructures and serve as recognition elements for aptasensors for diagnostic applications (*e.g.*, α-thrombin, ATP, antibiotics) [158,159]. Identification of these elements for aptasensors demand chemical probes that can bind certain structural motifs with high affinity and specificity. Available label-free probes for the 3WJ structures such as blue cyanine (Cy7), naphthyridine (ATMND), and calix-3-carbazole have either low sensitivity or emit in the UV light range [63]. However, visible fluorescent light-up probes for specific 3WJ structure recognition are currently lacking.

Here, I show binding analysis of a merocyanine containing probe that could function as a universal turn-on dye for DNA 3WJ motifs. Merocyanine dyes contain an aromatic donor vinyl linked to a cationic acceptor and have been used as colorimetric indicators and chemosensors. Van Riesen *et al*. initially designed a new phenolate merocyanine dye (Figure 3.1, PhOBtz) that could be used as a temperature chemosensor [160–162]. In the second part of this chapter, I present an application of fluorometry techniques in the detection of a newly designed fluorescent light-up probe (Figure 3.1, FPhOBtz).

3.3 Materials and Methods

3.3.1 Sample preparation

All aptamer samples were purchased from Integrated DNA Technologies (IDT, Coralville, Iowa) with standard desalting purification. All aptamer and ligand solutions were prepared in the same manner as discussed in Chapter 2. The merocyanine probe FPhOBtz was synthesized in Professor Richard Manderville's lab at the University of Guelph [140,160]. Except when it is specified, all

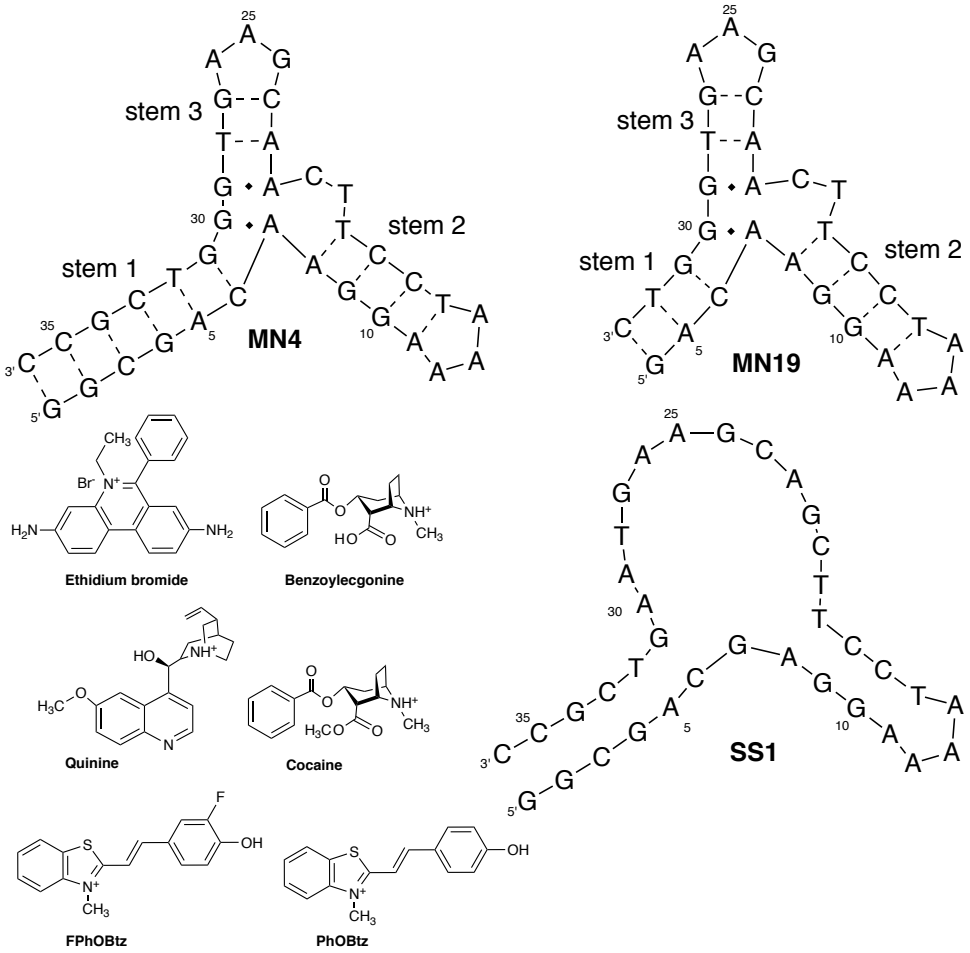

Figure 3.1 Structures of the ligands and the DNA aptamers discussed in this chapter. Dashed lines between nucleotides indicate Watson-Crick base pairing in the secondary structure, whereas diamonds show the AG base pairs. Solid lines display the phosphodiester bonds in the backbone of the aptamers.

aptamer and ligand samples were dissolved in 20 mM sodium phosphate (pH 7.4) and 140 mM NaCl before use. DNA samples were incubated at 95 °C for 3 min and immediately immersed in ice water for 5 min before they were mixed with the ligand.

3.3.2 Fluorescence measurements

Fluorescence scans were performed employing a Cary Eclipse spectrofluorometer and 10 mm fused quartz cuvettes. Each experiment was performed at a constant temperature maintained throughout each experiment using a Cary Peltier controller as discussed in Chapter 2. For each ligand-aptamer titration, the total ligand concentration was kept constant and lower than the available K_d value. To ensure the ligand is fully saturated with the aptamer, the maximum concentration of aptamer was quantified using Eq. 2.1. The observed fluorescence intensities were corrected for the inner-filter effect to compensate the loss of the incident intensity using Eq. 2.6 [104,163]. For the simplicity of the parameters referred to in this study, all of the observed fluorescence intensities were corrected and denoted as fluorescence intensity (F).

The fluorescence intensities were averaged and normalized as relative fraction units (RFU) of F_o, where F_o denotes the fluorescence intensities of the ligand in the absence of the aptamer. To quantify the binding affinities, each binding isotherm was plotted as a function of bound to free ligand (F/F_o) versus the total aptamer concentration in the solution. Then, each isotherm was fitted to Eq. 2.5. The dissociation constant (K_d) was obtained using a non-linear regression analysis as explained in Chapter 2.

In quinine-aptamer binding assays, quinine was excited at 234 nm. Then, emission scans were performed from 270 nm to 450 nm to exclude the interference of Raman and Rayleigh scattering peaks. The maximum fluorescence intensity of quinine at (383 ± 1) nm was collected from each spectrum. For the cocaine-aptamer binding assays, cocaine was excited at 232 nm. The emission scans were carried out from 270 nm to 450 nm, and the maximum fluorescence intensity

of cocaine was detected at (315 ± 1) nm. To confirm that the quenching results were specific for a functional cocaine-binding aptamer, both ligands were titrated against a non-binding aptamer construct (SS1) at 15 °C and under the same conditions as performed for MN4 and MN19.

In the dynamic quenching analyses, the Stern-Volmer isotherms of the acquired maximum fluorescence intensities were plotted as a function of free to bound ligand (F_o/F) versus the total aptamer concentration. The Stern-Volmer plots were fitted to the mixed static-dynamic quenching models:

$$\frac{F_o}{F} = (1 + K_{SV}[Q])(1 + K_a[Q]) \quad \text{Eq. 3.1}$$

$$\frac{F_o}{F} = (1 + K_{SV}[Q])e^{V[Q]} \quad \text{Eq. 3.2}$$

where the association constant (K_a) and the Stern-Volmer constant (K_{SV}) become mutually dependent constants, and (V) stands for the volume per mole of the ligand-aptamer complex within the static interaction proximity [164–166].

To compare the effect of intercalation with the base-stacking interactions, the MN4 and MN19 aptamers were titrated into 1 μM ethidium bromide (EtBr) and excited at 230 nm, 286 nm, and 486 nm separately. Each emission scan was acquired from 550 to 700 nm to detect the fluorescence of EtBr at (613 ± 1) nm at 23 °C. Similar to binding affinity analyses of quinine and cocaine, the maximum emitted intensities of EtBr were averaged, corrected, and analyzed as discussed for quinine and cocaine. Furthermore, wavelengths of the emission maxima were recorded to determine the Stokes shift of each fluorescence scan. The difference in Stokes shifts between free and bound states of the ligands (EtBr, quinine, and cocaine) with the MN4 and MN19 aptamer variants were recorded for a comparative analysis.

To quantify the bimolecular quenching rate constant (k_q) of cocaine, the fluorescence lifetime (τ) of cocaine in the absence of aptamers were measured using the time-resolved mode of the Cary Eclipse spectrofluorometer at 15 °C and 23 °C. The rate of the fluorescence intensity as a function of time (t) was fitted to:

$$F(t) = I_o e^{-t/\tau} \quad \text{Eq. 3.3}$$

where I_o denotes the incident light intensity. For the calculation of k_q in quinine–aptamer binding experiments, we used the standard τ_o values available in the literature (18.5 ns and 17.5 ns) at 15 °C and 23 °C, respectively. The k_q was computed using Eq. 3.4:

$$\frac{F_o}{F} = (1 + K_{SV}[Q]) = (1 + K_a[Q]) = 1 + k_q \tau_o [\mathrm{Q}] \quad \text{Eq. 3.4}$$

where the Stern-Volmer constant (K_{SV}) represents a dynamic binding constant in a collisional interaction. In an exclusively static quenching, the K_{SV} is replaced with the K_a.

Fluorescence titrations with 1 μM FPhOBtz in PBS buffer (pH 7.4) were carried out with systematic addition up to 2 μM (2 eq.) MN4 and mixed for 2 min. The relative fluorescence quantum yields (Φ_f) of unbound FPhOBtz and FPhOBtz•MN4 in PBS buffer at 20 °C were measured using quinine sulfate in 0.1 N sulfuric acid for the fluorescence standard solution as discussed in Chapter 2 [167]. Six samples in a concentration range from 0.2 to 10 μM unbound FPhOBtz were individually excited at 485 nm, and the integrated emission intensities were detected at 560 nm in a wavelength range of 500-600 nm. For the quantum yield measurements of FPhOBtz•MN4, FPhOBtz samples were mixed with 3-fold MN4 concentrations and the molar ratio of MN4 to FPhOBtz was kept constant throughout the experiment. The photomultiplier tube voltage, signal-to-noise ratio, and spectral bandwidth parameters were also kept constant in all experiments. FPhOBtz•MN4 samples were individually excited at 540 nm, and the integrated

emission intensities were detected at 580 nm in a wavelength range of 550-650 nm. The integrated emission intensities were plotted against the integrated excitation (absorption) intensities. The obtained linear slope was used to quantify the relative quantum yield values using OriginPro software package [132].

3.4 Results

3.4.1 Effect of aptamer binding on ligand fluorescence

Upon addition of aptamer to quinine or cocaine, the fluorescence of the ligand was quenched (Figure 3.2). We utilized this quenching to quantify the binding affinity and dynamics of MN4 and MN19 to both quinine and cocaine. The observed fluorescence emission maxima were corrected for the inner-filter effect using Eq. 2.6 for each aptamer-ligand pair accounting for the absorbance of DNA at the excitation wavelength used for the ligand. We found that the titrations of MN4 and MN19 into a constant concentration of quinine, while irradiated at 234 nm, quenched the maximum fluorescence emission at ~383 nm (Figure 3.2a). Similarly, the titrations of MN4 and MN19 aptamers in cocaine, while excited at 232 nm, quenched the maximum fluorescence emission at ~315 nm (Figure 3.2b). The nonlinear fitting analyses of the acquired binding isotherms using Eq. 2.5 (Figure 3.3) yielded the K_d values reported in Table 3.1. The K_d values of all four aptamer-ligand combinations decreased as the temperature was raised from 15 °C to 23 °C confirming temperature dependency of observed aptamer-ligand interactions (Table 3.1).

To confirm that the fluorescence quenching we observe is a result from specific binding, we analyzed the change in fluorescence of quinine and cocaine upon addition of the SS1 cocaine-binding aptamer. This aptamer has the same sequence as MN4 except that both AG base pairs

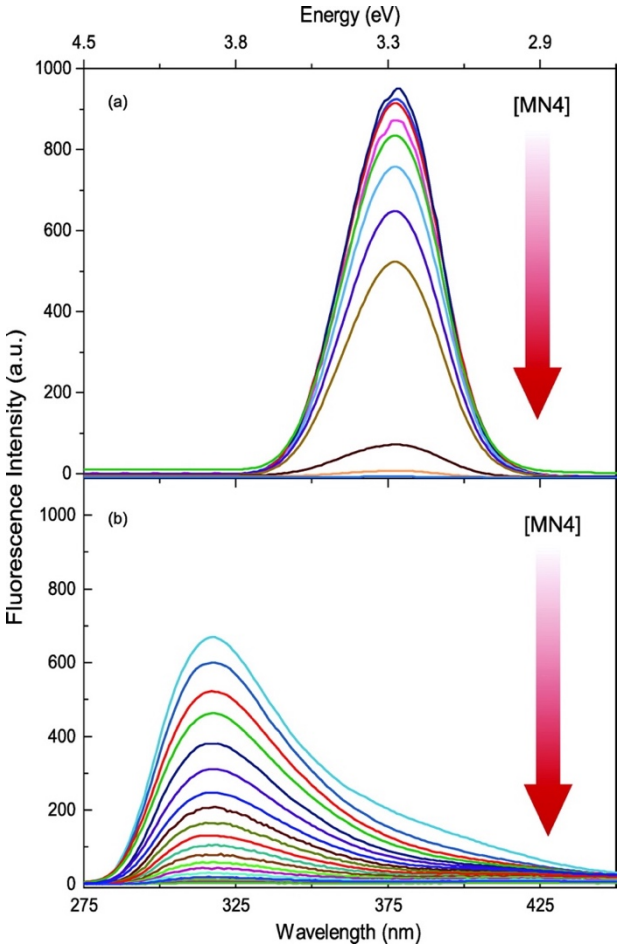

Figure 3.2 The raw fluorescence emission spectra of (**a**) quinine and (**b**) cocaine titrated with the MN4 aptamer. Fluorescence scans were carried out in 20 mM sodium phosphate buffer (pH 7.4) and 140 mM NaCl at 23 °C. Aptamer aliquots quenched fluorescence, and aptamer was added until the fluorescence of the ligand remained unchanged between additions. (**a**) Fluorescence emission spectra of 0.06 μM quinine hemisulfate excited at 234 nm. (**b**) Fluorescence emission spectra of 4.8 μM cocaine hydrochloride excited at 232 nm.

(A21/G29, A7/G30) are switched to be GA base pairs (G21/A29, G7/A30) (Figure 3.1). When SS1 was titrated into cocaine or quinine, the observed fluorescence reduced in intensity; however, when corrected for the inner filter effect, no reduction in binding was observed (Figure 3.4a-b). As a comparison, the observed and corrected data for MN4–quinine is also shown in Figure 3.4c.

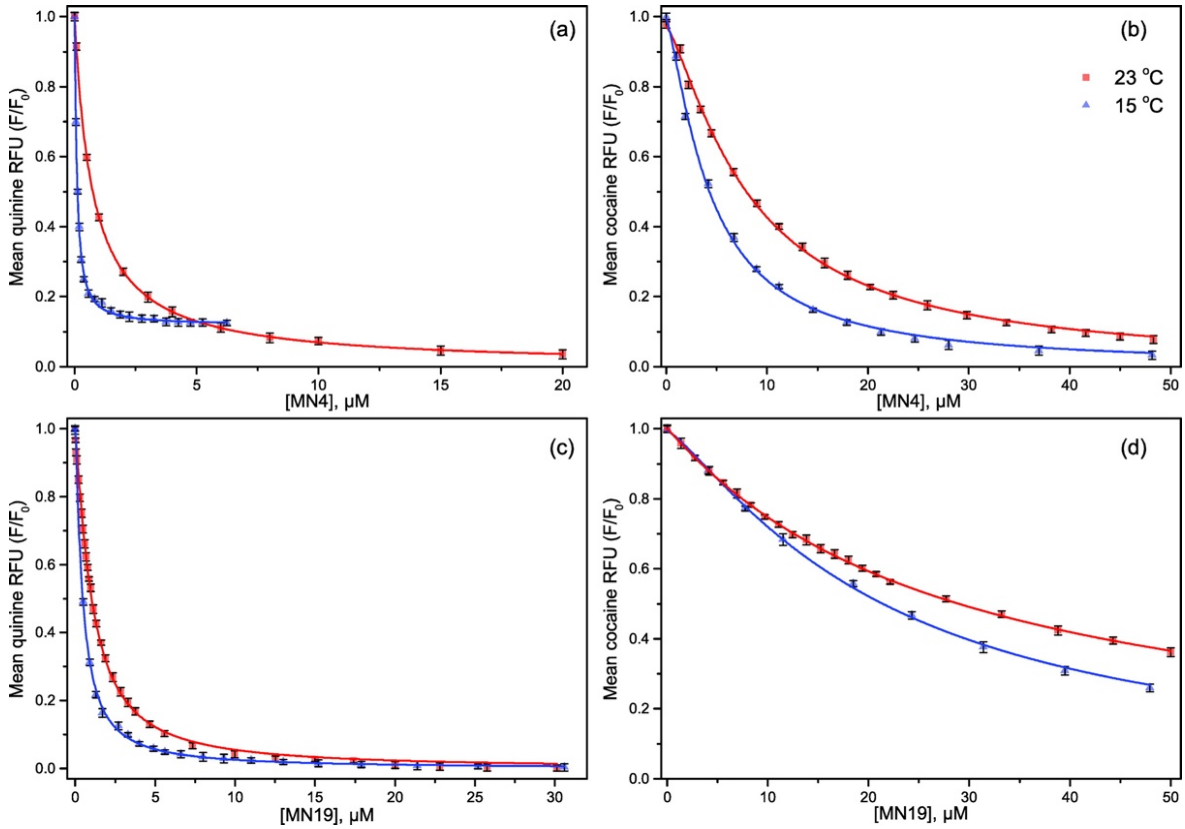

Figure 3.3 Steady-state fluorescence quenching analysis of quinine and cocaine ligands binding MN4 and MN19 aptamers in 20 mM sodium phosphate (pH 7.4) and 140 mM NaCl at 15 °C (blue triangle) and 23 °C (red square). Displayed here are the titrations of (**a**) MN4–quinine, (**b**) MN4-cocaine, (**c**) MN19-quinine, and (**d**) MN19-cocaine. The corrected and normalized relative fraction fluorescence (RFU) for each ligand is expressed on the vertical y-axis, where F_0 and F are inner-filter corrected emission maxima in the absence and presence of the corresponding aptamer, respectively. Each data point represents an average of 3-6 experiments, with the error bars representing one standard deviation.

As a further control, we tested the MS3 and ATP3 DNA sequences as additional negative controls for binding and also observed no change in the observed fluorescence upon addition of MN4.

The shift of the emission maximum of quinine was measured in the free and ligand-bound states for both MN19 and MN4 aptamers. When quinine was bound by MN4, the emission maxima of quinine shifted (3.05 ± 0.02) nm toward the infrared region (Figure 3.5a). A slightly shorter red

Table 3.1 Dissociation constants and binding parameters of the two ligands, quinine and cocaine, with the MN4 and MN19 aptamer constructs[1].

Aptamer	Temperature (°C)	K_d (μM)	K_{SV} (μM^{-1})	k_q ($\mu M^{-1}s^{-1}$)
Quinine				
MN4	15	0.094 ± 0.003	7.2 ± 0.3	39×10^7
	23	0.745 ± 0.004	1.31 ± 0.03	7.1×10^7
MN19	15	0.47 ± 0.01	2.71 ± 0.06	15×10^7
	23	1.09 ± 0.02	0.81 ± 0.01	4.4×10^7
Cocaine				
MN4	15	3.92 ± 0.07	0.24 ± 0.02	16
	23	7.7 ± 0.1	0.110 ± 0.001	7.1
MN19	15	21.1 ± 0.6	$(3.4 \pm 0.9) \times 10^{-3}$	0.22
	23	28.8 ± 0.3	$(4.75 \pm 0.06) \times 10^{-3}$	0.31

[1]Assays were carried out in 20 mM sodium phosphate buffer (pH 7.4), and 140 mM NaCl. The error range stated here is the standard deviation after fitting to a mean of 3-6 replicates. The K_d constants were quantified using Eq. 2.5. The K_{SV} constants were acquired using Eq. 3.1 and Eq. 3.2. The k_q rate constants were obtained using Eq. 3.4.

shift of (2.49 ± 0.01) nm occurred when quinine was bound by MN19. With cocaine binding, the emission maximum of MN4•cocaine shifted (1.07 ± 0.03) nm toward the infrared region, and with MN19 binding, it red-shifted by (0.46 ± 0.01) nm (Figure 3.5). These differences in Stokes shift are statistically different, as confirmed by a *t*-test with a *p*-value less than 0.0001.

To provide a comparison for quinine and cocaine binding, we titrated MN4 and MN19 into EtBr and monitored the change in fluorescence of EtBr. When bound by both MN4 and MN19, the fluorescence intensity of EtBr increased (Figure 3.5b). Additionally, the MN4•EtBr and MN19•EtBr complexes resulted a blue shift in the EtBr emission spectrum of (10.9 ± 0.02) nm and (11.5 ± 0.1) nm, respectively (Figure 3.5c).

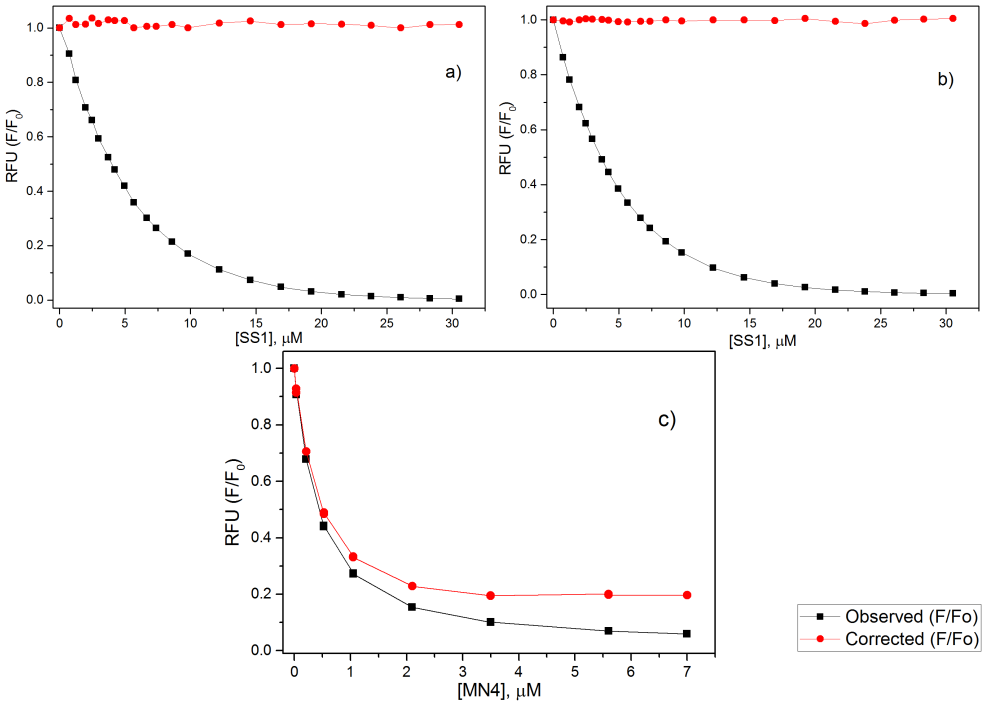

Figure 3.4 Shown is the emission of cocaine (**a**) and quinine (**b**) ligands versus the SS1 DNA construct concentration in 20 mM sodium phosphate (pH 7.4) and 140 mM NaCl. Black squares show the observed non-specific quenching of fluorescence due to the inner-filter effect of the aptamer. Red circles are the corrected fluorescence using Eq. 2.6. Isotherms in (**c**) display a comparison between the observed and corrected fluorescence quenching in MN4-quinine titration.

As a control ligand binding, we also analyzed the interaction of benzoylecgonine with MN4. Benzoylecgonine is a metabolite of cocaine and the cocaine-binding aptamer is typically described as only weakly binding, or not interacting, with this molecule [61,62,68,168]. Using differential scanning calorimetry (DSC) methods, Harkness *et al.* have determined an affinity of MN4 for benzoylecgonine of 0.60 mM at 30 °C [169]. Benzoylecgonine has the same fluorescent properties as cocaine, as shown in Figure 3.1, and its fluorescence is quenched upon addition of MN4 with a resulting K_d value of (91 ± 52) μM at 15 °C. This binding affinity agrees reasonably well with the expected affinity of 220 μM that is calculated using the thermodynamic parameters

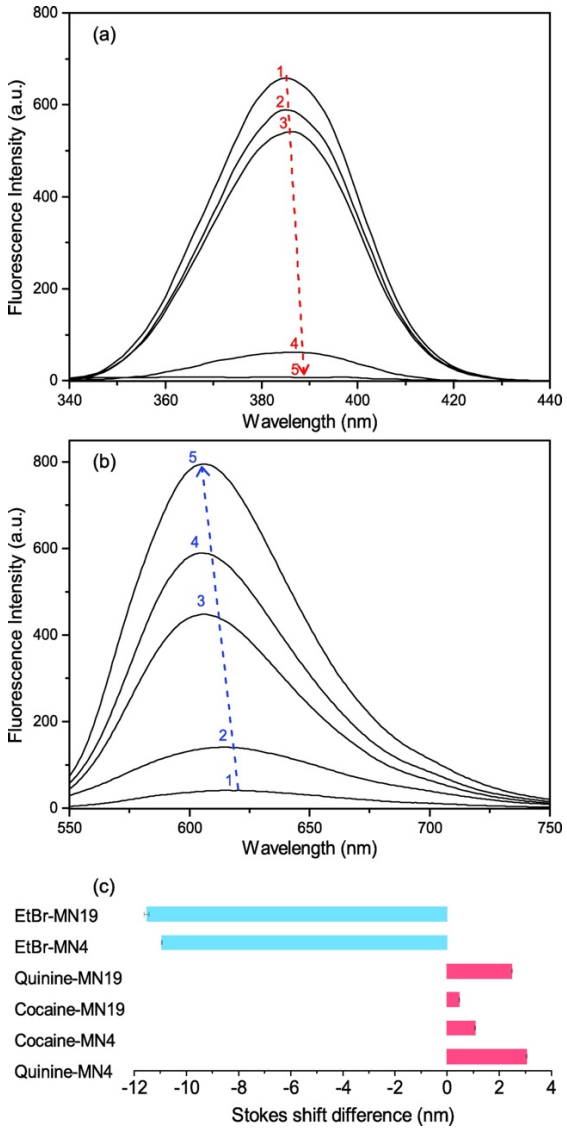

Figure 3.5 The fluorescence emission spectra of quinine and ethidium bromide (EtBr) titrated with MN4. Fluorescence scans were carried out in 20 mM sodium phosphate buffer (pH 7.4) and 140 mM NaCl at 23 °C. Aptamer aliquots were added until the fluorescence of the ligand remained unchanged. (**a**) Fluorescence emission spectra of 0.06 µM quinine hemisulfate excited at 234 nm. (**b**) Fluorescence emission spectra of 1 µM EtBr excited at 230 nm. (**c**) Bar graph of the changes in Stokes shift for the indicated combinations of ligand and aptamer.

previously reported by Harkness *et al*. [169]. We also note that the lower K_d value measured here at a lower temperature is consistent with our binding measurements that show the affinity of the cocaine-binding aptamer increases as the temperature decreases (Table 3.1).

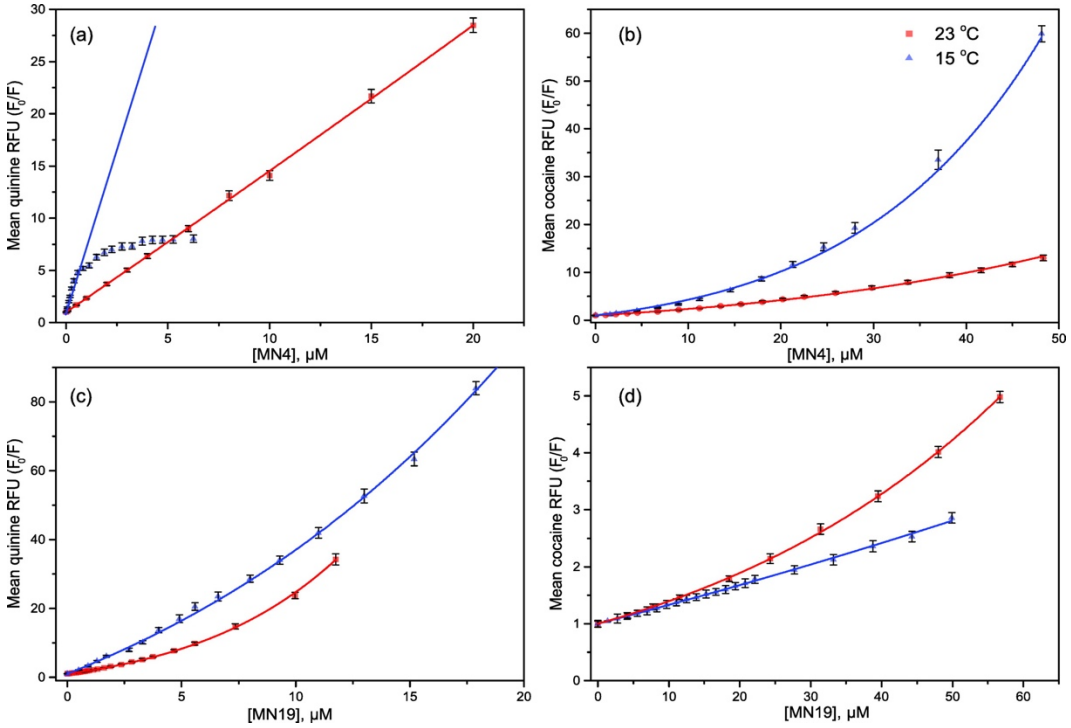

Figure 3.6 Dynamic and static fluorescence quenching analysis of quinine and cocaine ligands binding MN4 and MN19 aptamers at 15 °C (blue triangles) and 23 °C (red squares). Shown here are the Stern-Volmer plots of (**a**) MN4•quinine, (**b**) MN4•cocaine, (**c**) MN19•quinine, and (**d**) MN19•cocaine. The corrected and normalized relative fraction fluorescence (RFU) for each ligand is expressed on the y axis, where F_o and F are inner-filter corrected emission maxima in the absence and presence of the corresponding aptamer, respectively. Each data point represents an average of 3-6 experiments, with the error bar representing one standard deviation.

3.4.2 Analysis of fluorescence quenching mechanisms

I analyzed the mechanism of the fluorescence quenching of quinine and cocaine with MN4 and MN19 binding by Stern-Volmer analysis. The Stern-Volmer isotherm of MN4•quinine at 15 °C produced a nonlinear plot with K_{SV} constant of (7.2 ± 0.3) μM^{-1}, using the linear portion of the binding curve. The isotherm saturated with excess MN4 indicating that the ligand is fully bound (Figure 3.6a). In contrast, the MN4•quinine titration resulted in a linear Stern-Volmer plot with K_{SV} constant of (1.31 ± 0.03) μM^{-1} at 23 °C (Figure 3.6a). As both of these plots have a linear

region, when the temperature is increased, the K_{SV} value decreases. Therefore, I conclude that the MN4•quinine quenching follows a static mechanism [164,170–172].

The titrations of MN4•cocaine at 15 °C and 23 °C showed nonlinear Stern-Volmer plots with K_{SV} constants of (0.24 ± 0.02) μM^{-1} and (0.110 ± 0.001) μM^{-1}, respectively (Figure 3.6b). The titrations of MN19•quinine at 15 °C and 23 °C also showed nonlinear Stern-Volmer plots with K_{SV} constants of (2.71 ± 0.06) μM^{-1} and (0.81 ± 0.01) μM^{-1}, respectively (Figure 3.6c). For both of these aptamer-ligand pairs, the curve shows that quenching occurs through a mixed static–dynamic process [164,170–172].

For the titration of MN19 with cocaine at 15 °C, we observe a linear Stern-Volmer plot with a K_{SV} constant of (3.4 ± 0.06) mM^{-1}. We obtain a nonlinear plot with K_{SV} constant of (4.75 ± 0.06) mM^{-1} at 23 °C (Figure 3.6d). This switch from a linear to a quadratic plot and an increase in K_{SV} value with temperature indicates that the quenching mechanism changes from a mostly static to a mostly dynamic mechanism. The fluorescence lifetime (τ) of free cocaine was measured using time-resolved fluorescence spectroscopy. For free cocaine, τ was measured to be (2.6 ± 0.7) μs and (2.2 ± 0.8) μs at 15 °C and 23 °C, respectively. For quinine, the τ value is extremely short to measure using available instrumentation.

3.4.3 FPhOBtz Binding to MN4

In aqueous buffered solutions, FPhOBtz holds a p*K*a ≈ 6.6 with phenol and phenolate absorbance at ∼398 nm ($\varepsilon = 32{,}787.0\ cm^{-1}\ M^{-1}$) and ∼485 nm ($\varepsilon = 34{,}636.0\ cm^{-1}\ M^{-1}$). The fluorescence response of FPhOBtz to MN4 binding provided an increase of >600-fold emission intensity at

~580 nm to provide bright yellow fluorescence (Figure 3.7). In PBS at pH 7.4, free FPhOBtz provided a fluorescence quantum yield (Φ_f) of 0.085 for a brightness ($\varepsilon\Phi_f$) of 2,944.0 M^{-1} cm^{-1}. For the MN4•FPhOBtz complex, $\Phi_f = 0.76$ for $\varepsilon\Phi_f = 26{,}640.0$ M^{-1} cm^{-1}, a 10-fold increase in brightness compared to free FPhOBtz in PBS. For comparison, the brightness of PicoGreen dye ($\varepsilon \approx 7.0 \times 10^4$ cm^{-1} M^{-1}) bound to calf thymus DNA ($\Phi_f \approx 0.5$) is $\sim 3.5 \times 10^4$ cm^{-1} M^{-1}, which is only 1.3-fold brighter than the MN4•FPhOBtz complex. The emission intensity response was also pH dependent, exhibiting an approximately 3.5-fold increase at 580 nm upon raising the pH from 6.0 to 8.5. Thus, increased dye rigidity coupled with the phenolate was deemed important for the emission intensity response of FPhOBtz binding to MN4.

3.5 Discussion

We have used the observed fluorescence quenching of quinine and cocaine with aptamer binding to measure the affinity of these ligands to both the MN4 and MN19 cocaine-binding aptamer constructs (Table 3.1). The values measured here agree within experimental error with our previously reported values using ITC values [58,64,68]. The benefits of using this fluorescence technique to measure binding affinity are the significantly (over 40-fold) lower amounts of material needed for fluorescence methods compared with ITC methods and the faster time it takes to perform the titration in the fluorescence experiment than in the ITC run (though the ITC experiment is automated).

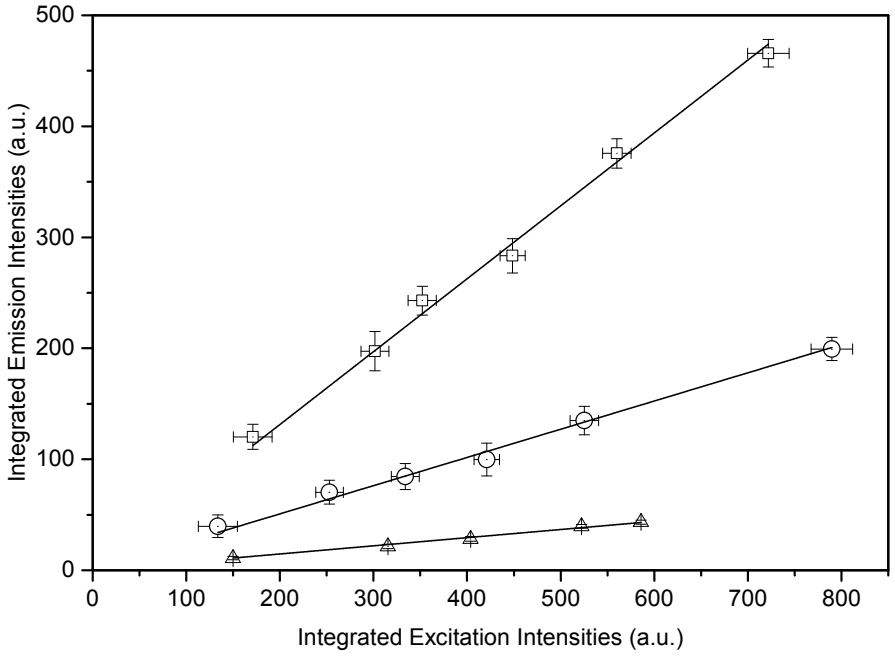

Figure 3.7 Fluorescence quantum yield measurements of FPhOBtz in 100% methanol (v/v). Shown is the linear regression analysis for the integrated fluorescence emissions as a function of integrated light absorbance (excitation) at 20 °C for unbound FPhOBtz ligand and bound to MN4. Triangles display the results for unbound FPhOBtz at 485 nm excitation and 560 nm emission peaks (R^2 = 0.9988). Circles show the results for FPhOBtz•MN4 at 485 nm excitation and 577 nm emission peaks (R^2 = 0.9986). Squares demonstrate the results for FPhOBtz•MN4 at 534 nm excitation and 577 nm emission peaks (R^2 = 0.9992). For FPhOBtz•MN4 experiments, the molar ratio of MN4 to FPhOBtz kept constant at 3-fold. Error bars are one standard deviation of three trials.

The experiments performed in this study, where the intrinsic change in fluorescence intensity upon binding is used to measure affinity, is not new but has rarely been used to study aptamer-ligand interactions. This method could be easily implemented to other aptamer-ligand pairs as long as the ligand for the aptamer has fluorescence properties.

The fluorescence studies performed here also provide new insights into the binding interaction of cocaine and quinine with the cocaine-binding aptamer. As we previously noted, the values of the thermodynamic binding parameters (ΔH and $T\Delta S$) place cocaine and quinine into the intercalating type of DNA ligands, as classified by Chaires [67,173]. However, quinine and cocaine are neither known to be intercalating molecules, nor do they seem likely to be intercalators as their structures possess only one or two fused aromatic rings. Instead, we have thought that these two ligands interact with the cocaine-binding aptamer in a stacking manner where one face of the aromatic ring of the ligand interacts in a π–π stacking manner with a base or multiple bases in the aptamer. It is likely that stacking interaction contribute significantly to binding as 6-methoxyquinoline, the aromatic portion of quinine, is bound by the cocaine-binding aptamer 10-fold tighter than cocaine [68].

In support of this stacking mechanism, we measured the fluorescence binding properties of a known intercalator, EtBr, and compared them with those of cocaine and quinine. The fluorescence intensity of EtBr increases when bound by the aptamer, and we observe a blue shift of 11-12 nm with MN4 and MN19 binding (Figure 3.5). These values are consistent with previously reported changes in fluorescence for EtBr intercalating into DNA [174,175].

In contrast to EtBr fluorescence results, cocaine and quinine exhibit fluorescence quenching and a red shift when binding MN19 or MN4 (Figure 3.5). These differences indicate that in the bound state, quinine and cocaine are still at least partially solvent accessible as would be expected in a stacking arrangement. Jagtap *et al.* demonstrated that overlap of conjugated π-

systems in stacking interactions results in a distinctive emission transition to the low-energy range and this red shift increases with greater π-system overlap [155].

Our results show that quinine binding by MN19 and MN4 yields a greater red shift than when the same aptamers bind cocaine. Detecting a smaller red shift in cocaine-aptamer emission spectra corresponds to cocaine having one aromatic ring as opposed to two fused aromatic rings in quinine. This is consistent with stacking interactions.

3.6 Conclusion

To conclude, the change in the fluorescence spectrum of quinine and cocaine ligands as a function of cocaine-binding aptamer concentration is a powerful and sensitive tool to quantify the binding affinities of cocaine-binding aptamers, as well as provide insights into their binding mechanisms. Presented results confirm that quinine binding by MN19 and MN4 yields a larger red shift than that of with cocaine, which corresponds to cocaine having one aromatic ring as opposed to two fused aromatic rings in quinine.

Chapter 4: Optimizing stem length to improve ligand selectivity and thermal stability in a structure-switching cocaine-binding aptamer

4.1 Preface

Presented work in this chapter has been published in the articles listed below [158,176,177]:

- Neves, M.A.D.[*], **Shoara, A.A.[*],** Reinstein, O.[*], Borhani, O.A., Martin, T.R., and Johnson, P.E. (2017) Optimizing Stem Length to Improve Ligand Selectivity in a Structure-Switching Cocaine-Binding Aptamer. *ACS Sensors* 2, 1539–1545, ([*]denotes co-first author).

- **Shoara, A.A.**, Reinstein, O., Borhani, O.A., Martin, T.R., Slavkovic, S., Churcher, Z.R., and Johnson, P.E. (2018) Development of a thermal-stable structure-switching cocaine-binding aptamer. *Biochimie* 145, 137–144.

- Neves, M.A.D., S. Slavkovic, Reinstein, O., **Shoara, A.A**., Johnson, P.E. (2019) A proof of concept application of aptachain: ligand-induced self-assembly of a DNA aptamer, RSC Adv. 9, 1690–1695.

4.2 Introduction

The development of aptamer-based sensing technologies is a rapidly growing field. Reasons for this include the ease of current *in vitro* selection strategies that can select an aptamer for almost any target and the straightforward nature of nucleic acid chemical modifications that allow for the easy immobilization of an aptamer to a sensing surface or covalent attachment of a chemical label or tag [178]. Many aptamers undergo or can be engineered to undergo a structural transition upon ligand binding, and the signal transduction schemes of many aptamer-based biosensors require ligand-induced structural changes or structure formation of the aptameric probe [154].

In general, structure-switching aptamers have lower affinity for their targets than aptamers that feature a preformed secondary structure. However, biosensors that can function using either a structure-switching or a rigid aptamer display greater analytical sensitivity using the structure-

switching aptamer, despite the lower affinity [65]. This indicates that, in general, the structural changes that an aptamer undergoes upon ligand binding are more important for ligand selectivity than just the affinity of the aptamer when utilized as the biosensing element in a sensor provided sufficient affinity is retained by the aptamer.

The cocaine-binding aptamer has become a model system for the development of aptamer-based biosensors. The secondary structure of the aptamer is composed of three stems arranged into a three-way junction with both tandem AG base pairs and a dinucleotide bulge located at or adjacent to the three-way junction (Figure 4.1) [64]. When stem 1 has 6 bp, the aptamer folds in the free state and retains the same secondary structure when it is ligand-bound. However, if stem 1 is shortened to be 3 bp in length, as shown in Figure 4.1, the aptamer undergoes a ligand-induced structure switching binding mechanism. In the ligand-free state, the short stem 1 aptamer is loosely or poorly structured. Upon ligand binding, the aptamer folds or dynamically tightens into the secondary structure shown in Figure 4.1 [179]. It is this structure-switching binding mechanism that has been exploited in many of the applications of the cocaine-binding aptamer in biosensor development, and consequently, the short stem 1 version of the cocaine-binding aptamer is a widely utilized version of the cocaine binding aptamer [180].

The structure switching nature of the short stem 1 construct of the cocaine-binding aptamer must arise from the interplay between the destabilizing reduction in the length of stem 1 and the stabilizing nature of ligand binding. This is demonstrated by the observation that tighter binding ligands for the cocaine-binding aptamer such as quinine [181], result in aptamer-ligand pairings with a higher melt temperature than the cocaine-bound aptamer [169]. Additionally, the steroid-

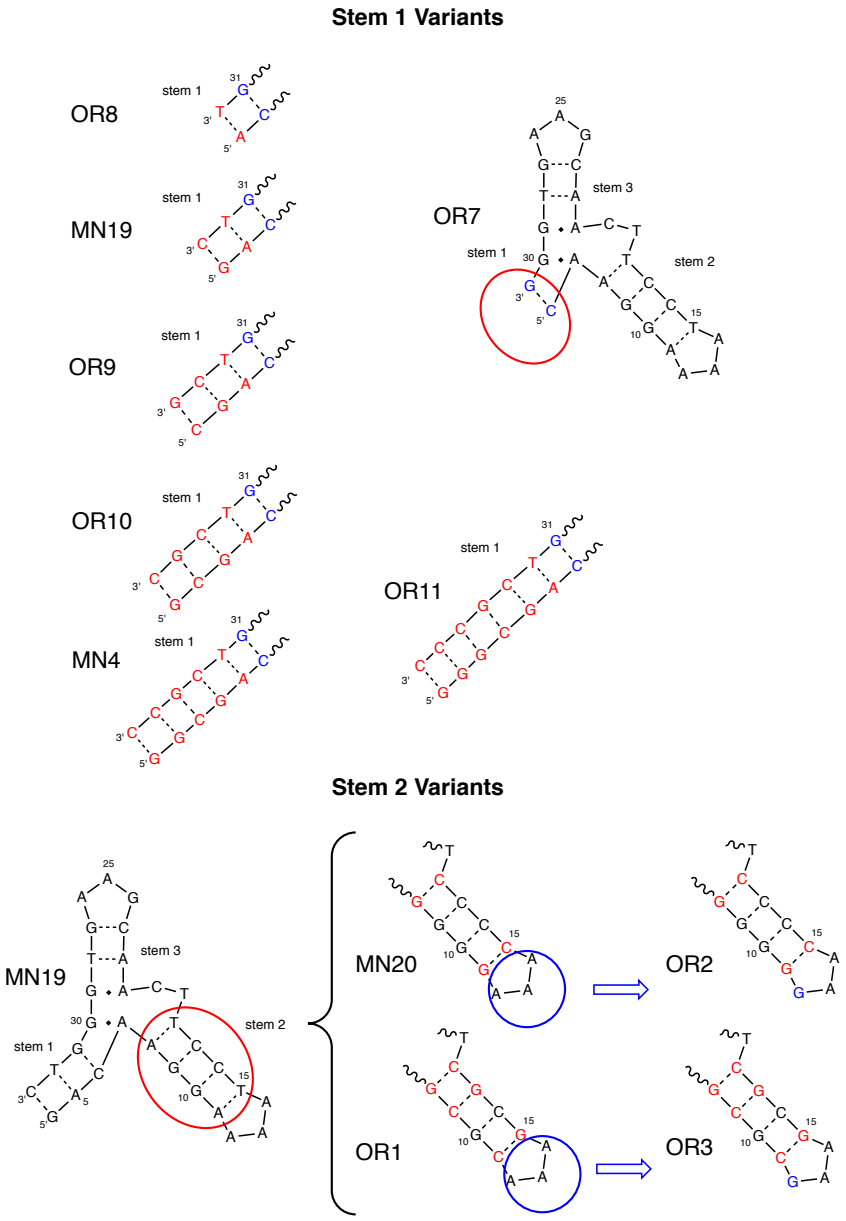

Figure 4.1 Sequence and secondary structures of the cocaine-binding aptamer variants investigated in this chapter. For ease of comparison, nucleotides in all constructs are numbered in the same manner.

binding aptamer, a three-way junction aptamer based on the cocaine-binding aptamer sequence, binds deoxycholic acid very weakly. This interaction is not tight enough to fold the version of the aptamer that contains a three-base-pair-long stem 1. Instead, deoxycholic acid binds and folds a

version of this aptamer with a stem 1 of four base-pair long [66]. Despite the widespread adoption of the short stem 1 version of the cocaine-binding aptamer (Figure 4.1; MN19) in biotechnology, this sequence is not optimal, as it is only marginally stable at room temperature. This is demonstrated by previously published temperature dependent NMR studies [64], temperature-dependent ITC-based binding studies [68], and DSC analyses [66].

The goal of this study is to develop a more thermally stable version of the cocaine-binding aptamer that preserves the functionally important ligand-induced structure-switching binding mechanism. To achieve this, we retained the three-base pair-long stem 1 and the sequence of stem 3, as these stems are important for the structure-switching and ligand binding functions. We modify the sequence of stem 2 to obtain a cocaine-binding aptamer variant with as high a melt temperature as possible based on the nearest-neighbour effect [182]. We demonstrate that the resulting sequence, OR3 (Figure 4.1), has these characteristics.

4.3 Materials and Methods

In determining which sequences to investigate we used MN4 as a starting point and simply shortened the length of stem 1 one base pair at a time. In elongating stem 1, we added a GC base pair in order to help maximize the stability of the longer stem 1 aptamer (OR11). Aptamer and ligand concentrations were determined by UV absorbance spectroscopy using the extinction coefficients supplied by the manufacturer. All aptamer samples were obtained from Integrated DNA Technologies (IDT) and prepared in the same manner as described in Chapter 2. Cocaine hydrochloride, quinine hemisulfate monohydrate ligands, and other analytical grade reagents were purchased from Sigma-Aldrich.

4.3.1 UV Thermal Melts

UV thermal melt experiments were performed using a Cary 100 spectrophotometer and 10 mm fused quartz cuvettes. The DNA melting curves were observed in a temperature range of 5 °C to 65 °C for cocaine-aptamer experiments due thermolability of cocaine and a range of 5 °C to 80 °C for quinine-aptamer assays. The temperature was changed throughout each experiment at 1 °C·min^{-1} using a Cary Peltier controller with an instrumental precision of ± 0.05 °C in milliseconds timescale. Each experiment was performed in 20 mM sodium phosphate buffer (pH 7.4), 140 mM NaCl. For each run, a concentration of aptamer was chosen to yield ~0.5 absorbance arbitrary units (a.u.) at 260 nm using the known extinction coefficients of the aptamers. For aptamer-quinine complexes, the amount of ligand was adjusted to provide a 95% ligand-bound aptamer sample using Eq. 2.1 and known K_d values. The observed UV light absorbance at 260 nm from 4-6 replicates was averaged and then the difference between the average sample and average blank absorbance was obtained. For free aptamer, the blank was the corresponding buffer; for aptamer-quinine samples, the blank was quinine in the stated buffer. This difference was then normalized (I) as:

$$I = (\Delta I_{max} - \Delta I_i)/(\Delta I_{max} - \Delta I_{min}) \quad \text{Eq. 4.1}$$

where ΔI_{max} is the maximum value of the difference between the sample absorbance, ΔI_{min} is the minimum value of the difference between the sample absorbance, and ΔI_i is the value of the difference between the sample and blank absorbance at a particular temperature. Then the normalized absorbance values (I) were plotted against the temperature. To quantify the thermal denaturation (T_m) value, the first derivative of each thermal curve (dI/dT) was plotted as a function of temperature using OriginPro 2016 software. The maximum peak value of each dI/dT versus

temperature was acquired as T_m value and reported as an average with experimental standard deviation (SD).

4.3.2 Fluorescence thermal shift assays

Differential thermal shift assays using intrinsic fluorescence of ligands were performed to study the aptamer-ligand bound complex thermal stability employing a 90°-light path Cary Eclipse spectrofluorometer and 10 mm fused quartz cuvettes. The temperature was monitored throughout each experiment at 1 °C·min^{-1} using a Cary Peltier controller with an instrumental precision of ± 0.05 °C in milliseconds timescale. The thermal shifts were observed in a temperature range of 5 °C to 65 °C for cocaine-aptamer experiments due thermolability of cocaine and 5 °C to 80 °C for quinine-aptamer assays in 20 mM sodium phosphate buffer (pH 7.4), 140 mM NaCl. For aptamer-ligand complexes, the amount of ligand was adjusted to provide a 95% ligand-bound aptamer sample using Eq. 2.1 and known K_d values.

Quinine-aptamer complexes were optimized for the excitation and emission maxima of quinine, photomultiplier tube voltage, signal-to-noise ratio, and spectral bandwidth parameters. The observed fluorescence emission intensities from 4 to 6 replicates were corrected for the inner-filter effect to compensate for the loss of the light intensity by the aptamer as described in Chapter 2. The obtained corrected fluorescence intensities were averaged and normalized using Eq. 4.1 to be consistent with the UV melts. In the assays of the quinine-aptamer complexes, quinine was excited at 234 nm, and the emission maxima were recorded at 383 nm. For the assays of the cocaine-aptamer complexes, cocaine was excited at 232 nm, and the maximum fluorescence intensity was detected at 320 nm. The obtained fluorescence intensities were averaged. Then the

difference between the average bound and average fluorescence intensity of blank ligand was obtained. This difference was then normalized as:

$$F = (\Delta F_i - \Delta F_{start})/(\Delta F_{end} - \Delta F_{start}) \quad \text{Eq. 4.2}$$

where ΔF_{start} is the value of the difference between the fluorescence intensity of the ligand-aptamer mixture and free ligand fluorescence intensity at the start of the melt (lowest temperature), ΔF_{end} is the value of the difference between the fluorescence intensity of the ligand-aptamer mixture and free ligand fluorescence intensity at the end of the melt (highest temperature), and ΔF_i is the value of the difference between the fluorescence intensity of the ligand-aptamer mixture and free ligand fluorescence intensity at a particular temperature. The normalized fluorescence (F) was then plotted against temperature. To quantify the thermal shift, the first derivative of each thermal curve (dF/dT) was plotted as a function of temperature [183]. The maximum peak value of each dF/dT versus temperature was acquired as T_m value and reported as average with experimental standard deviation (SD).

4.4 Results

4.4.1 Aptamer thermal stability analysis of stem 2 optimization

The thermal stability of the different stem 2 variants both free and bound to quinine was analyzed by UV melting experiments. All the constructs displayed evidence of being unfolded in the free state as their UV light absorbance at 260 nm (A_{260}) versus temperature plots displayed no sign of a typical sigmoidal denaturation curve (Figure 4.2). In the presence of quinine, all the constructs exhibited a sigmoidal melt curve as shown for MN19•quinine and OR3•quinine in Figure 4.2. From a first-order derivative analysis, the T_m values for the aptamer•ligand complexes were obtained and are listed in Table 4.1. These data show that the MN19•quinine complex has the

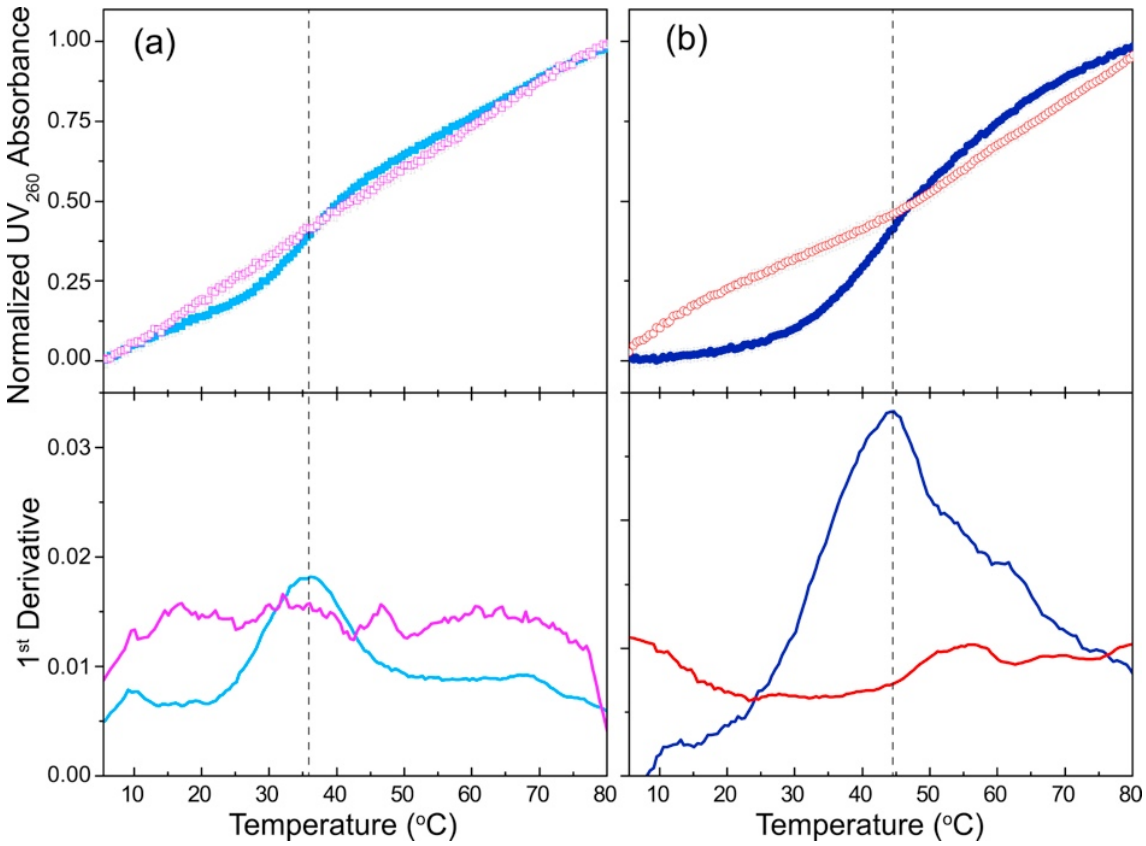

Figure 4.2 Analysis of thermal stability using UV-monitored melting curves. Shown is the normalized UV absorbance at 260 nm for the (**a**) MN19 both free (open pink squares) and quinine-bound (filled blue squares) and (**b**) OR3 free (open red circles) and quinine-bound (filled blue circles). On top are the UV_{260} absorbance plots in a temperature range of 5 °C-80 °C. On the bottom, the first-order derivatives of the melts are shown. Dashed lines designate the T_m point of aptamer-quinine complexes. Each data point denotes an average of 4-6 experiments with the error bars corresponding to one standard deviation. Data acquired in 20 mM sodium phosphate buffer (pH 7.4), 140 mM NaCl.

lowest T_m value (35.5 ± 0.3 °C) and OR3 has the highest T_m value (44.2 ± 0.1 °C). As a comparison for the UV melt analysis, the stability of MN19 and OR3 were also analyzed using a fluorescence thermal shift assay based on the differential scanning fluorimetry technique [184].

The presented differential scanning fluorimetry method is very sensitive, and the effects of both quinine and cocaine binding on the stability of MN19 and OR3 were investigated. When the

Table 4.1 Thermal denaturation temperature for aptamer-quinine complexes determined using UV melts and fluorescence shift assays[1].

Aptamer	*Free (UV) (°C)*	*Quinine-bound (UV) (°C)*	*Quinine-bound (Fluorimetry) (°C)*
OR8	ND	28 ± 1	27.0 ± 0.9
MN19	ND	35.6 ± 0.3	35.2 ± 0.5
		35.5 ± 0.3	
OR9	42.6 ± 0.6	44.1 ± 0.4	44.2 ± 0.7
OR10	51.6 ± 0.4	53.1 ± 0.4	53.1 ± 0.6
MN4	56.7 ± 0.4	57.6 ± 0.4	57.6 ± 0.5
OR11	61.7 ± 0.6	62.1 ± 0.2	62.6 ± 0.3
MN20		40.2 ± 0.2	
OR1		44.0 ± 0.2	
OR2		43.7 ± 0.3	
OR3		44.2 ± 0.1	

[1]Data acquired in 20 mM sodium phosphate (pH 7.4), 140 mM NaCl. The values reported are averages of 4-6 individual experiments. The error range reported is one standard deviation. ND denotes no thermal denaturation detected.

aptamer binds its ligand, quinine and cocaine fluorescence intensity is quenched [104]. In this assay, the increase in the intrinsic fluorescence intensity of a ligand is measured as the ligand is released when the aptamer is thermally unfolded. First derivative analysis of the MN19•cocaine thermal shift provides a T_m value of (26.6 ± 0.8) °C while the OR3•cocaine complex has a T_m value of (31.0 ± 0.7) °C (Figure 4.3). For the MN19•quinine thermal shift, a T_m value of (35.2 ± 0.3) °C was obtained, and for the OR3•quinine complex a T_m value of (44.6 ± 0.7) °C was measured.

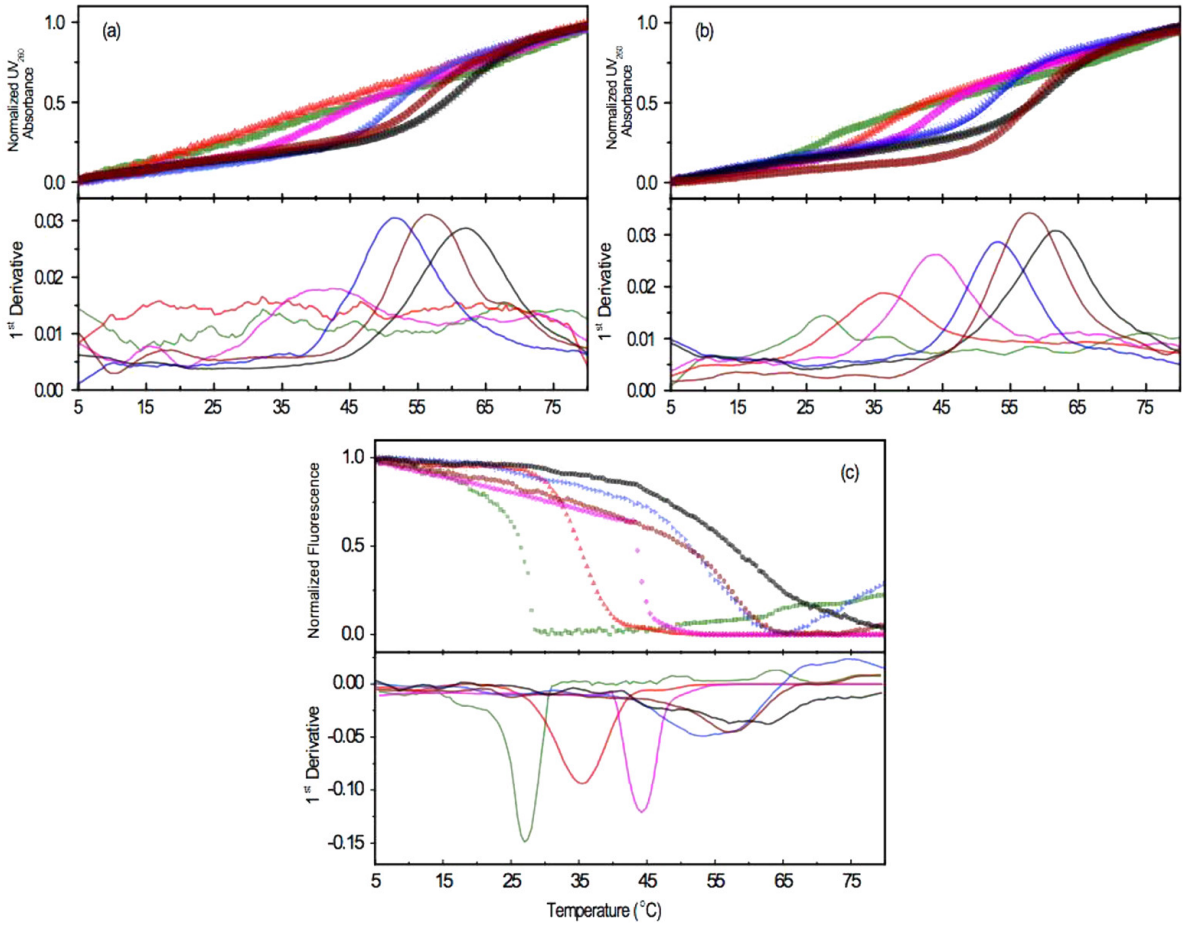

Figure 4.3 Analysis of the thermal stability of the unbound and quinine-bound aptamer constructs. Shown are the normalized UV absorbance at 260 nm for the OR8 (green), MN19 (red), OR9 (magenta), OR10 (blue), MN4 (brown), and OR11 (black) aptamer constructs: (**a**) unbound and (**b**) quinine-bound states. Analysis of the thermal stability of the aptamer-quinine complexes using differential scanning fluorimetry thermal shift analysis is shown in (**c**). Each data point denotes an average of 4-6 experiments with the error bars corresponding to one standard deviation. Data acquired in 20 mM sodium phosphate buffer (pH 7.4), 140 mM NaCl.

4.4.2 Aptamer thermal stability analysis of stem 1 optimization

I have analyzed the stability of the free and quinine-bound aptamers using UV-based thermal melts as well as using differential scanning fluorimetry thermal shift analysis for the quinine-bound aptamers. For free OR8 and MN19 the UV melts were non-sigmoidal providing evidence for the absence of a folded structure of the unbound aptamer (Figure 4.3a). This confirms the findings

from the 1D NMR spectra of the studied aptamers, performed by other lab members, that also provided evidence for the absence of a fully folded unbound OR8 or MN19 aptamer. When bound to quinine the aptamers with stem 1 having two to seven base-pair-long showed a sigmoidal denaturation curve (Figure 4.3b) with T_m values provided in Table 4.1. These values showed that as stem 1 progressively elongated, the T_m values also progressively increased. These UV melts were confirmed using a fluorimetry based thermal shift assay looking at the quinine ligand being released from the bound aptamer (Figure 4.3c).

As previously demonstrated in Chapters 2 and 3, binding of aptamer quenches the intrinsic fluorescence of quinine [104]. Both the UV and fluorimetry-based thermal melting experiments match within the error ranges of each other. In all of the aptamers analyzed, the T_m value of the quinine-bound aptamer is higher than that of with the free aptamer. This indicates that ligand binding is occurring, and that quinine binding stabilizes the structure of the examined aptamer variants.

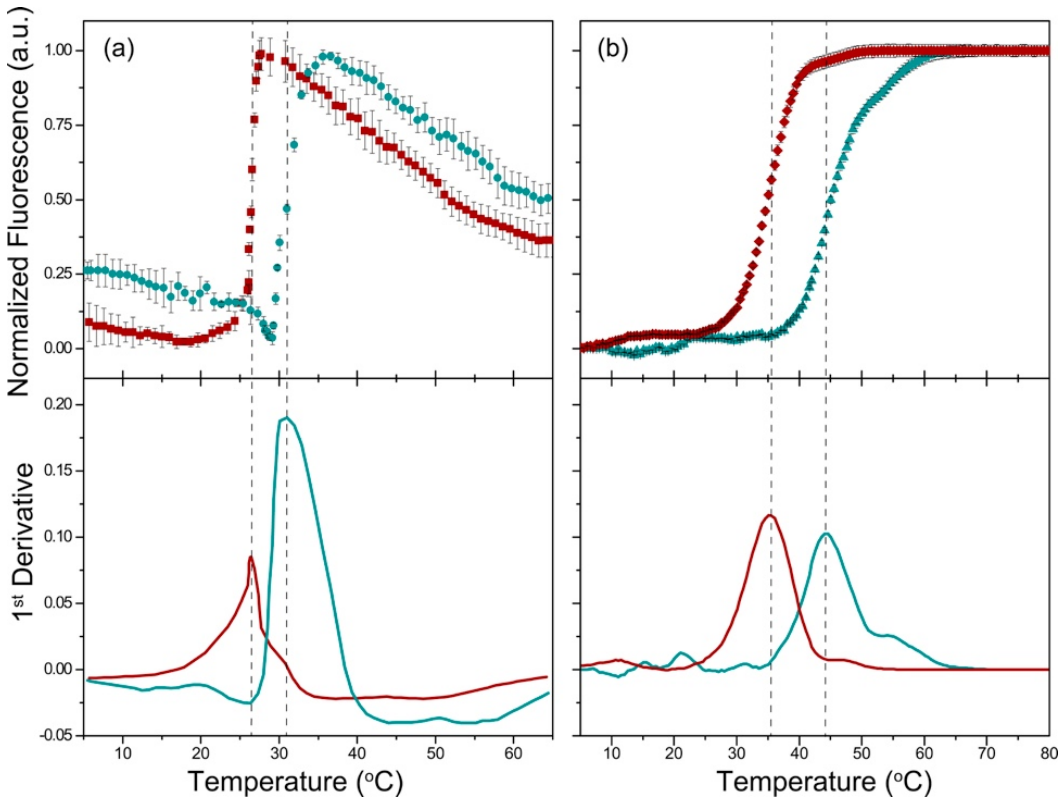

Figure 4.4 Analysis of thermal stability using differential scanning fluorimetry thermal shift analysis. Displayed are the average intrinsic fluorescence responses for OR3- and MN19-ligand complexes. (**a**) On top is the MN19•cocaine complex (red) and OR3•cocaine (green) thermal shift assays. Cocaine is excited at 232 nm, and emission maxima detected at 320 nm in a temperature range of 5 °C-65 °C. (**b**) On top is the MN19•quinine complex (red) and OR3•quinine (green) thermal shift assays. Quinine is excited at 234 nm, and emission maxima detected at 383 nm in a temperature range of 5 °C-80 °C. On the bottom of each panel is the first derivative of the MN19•ligand and OR3•ligand thermal shifts. Dashed lines indicate the T_m point of each aptamer-ligand complex. Each data point denotes an average of 4-6 experiments with the error bars corresponding to one standard deviation. Data acquired in 20 mM sodium phosphate buffer (pH 7.4), 140 mM NaCl.

4.5 Discussion

The primary goal of this project was to develop a thermally stable version of the cocaine-binding aptamer based on the rational design of its nucleotide sequence. The objectives were:

(1) to retain the ligand-induced structure-switching binding mechanism by retaining the three-base-pair stem 1 sequence.

(2) to retain the ligand-binding affinity of the original MN19 sequence by not changing the nucleotides likely to be involved in interacting with the ligand (in stems 1 and 3, and at the 3WJ) as identified by previous sequence variation and NMR-based chemical shift perturbation studies [58].
(3) to optimize the nucleotide sequence in stem 2 to increase the thermal stability of the bound aptamer.

The results shown in this chapter demonstrate that I have achieved stated objectives. As verified by the imino NMR spectra of the OR3 aptamer, performed by other lab members, this aptamer molecule retains the ligand-induced structure switching mechanism of the original short stem 1 construct MN19. The OR3 aptamer was chosen for structural analysis since it has the highest melt temperature of the aptamer-quinine complexes studied (Table 4.1). Additional NMR studies have shown that the OR3 aptamer is loosely or poorly structured in the free state and becomes structured as cocaine is titrated in the solution and bound by the aptamer. This behaviour is similar to other short stem 1 aptamers we have studied [66,147].

The exact structural nature of the ligand-free short stem 1 aptamer state is not known. Small angle X-ray scattering (SAXS), a method that measures hydrodynamic parameters of molecules, shows that there is little change in the radius of gyration (R_g) or the maximum interatomic vector in the molecule (R_{max}) between free and ligand bound MN19 [67]. As seen in the NMR spectra, the fact that there are some imino signals present in the free state shows that some base pairs do form in stems 2 and 3 in the absence of ligand. The absence of some observable imino signals is possibly due to a high level of dynamics in the free state that is reduced with ligand binding. This

reduction in dynamics is reflected in the reduction of the imino hydrogen exchange rates of both long and short stem 1 cocaine-binding aptamers upon ligand binding [179]. The loosely folded structure of the free short stem 1 construct, as demonstrated by the NMR spectra obtained by other lab members, is shared by both MN19 and OR3.

ITC methods, performed by other lab members, were used to measure the ligand binding ability of the series of short stem 1 constructs studied here. Previously, we demonstrated that the MN20 construct bound cocaine tighter than MN19 [58]. In the OR1, OR2 and OR3 constructs, the sequence alterations used to optimize the thermal stability do not adversely affect cocaine binding but yield a marginally tighter binding aptamer than MN19. Due to it having the highest thermal stability, OR3 was chosen for further ligand binding analyses using quinine as the ligand. Quinine binds the cocaine binding aptamer ~50 fold tighter than cocaine [68], ITC analyses, performed by other lab members, show that OR3 binds quinine slightly tighter (21 ± 2 μM) than it does with MN19 (26.7 ± 0.7 μM) in 20 mM Tris (pH 7.4), 140 mM NaCl, 5 mM KCl at 20 °C, mirroring the relative affinity seen for cocaine binding by these two aptamer variants.

The sequence changes in stem 2 of OR3 coincide with the location of the NaCl concentration-dependent second (low affinity) ligand-binding site in the cocaine-binding aptamer [185]. We therefore tested OR3 binding to quinine under buffer conditions of no added NaCl and determined that OR3 retains the ability to bind two molecules of quinine. In particular, the K_d values of the high affinity site of MN19 and OR3 are identical within the error ranges but the K_d value at the low-affinity site, the NaCl concentration dependant site in stem 2 is significantly lower in OR3 than in MN19. When comparing the sequence of stem 2 in OR3 and MN19 we have

retained the same number of Watson-Crick base pairs in both constructs though we have changed their identities. Retaining weak two-site binding in OR3 implies that binding at the second site depends at least to some extent on the shape of the aptamer though the exact identity of the base pairs is needed for high affinity binding at this site.

The thermal stability of the structure-switching version of the cocaine-binding aptamer was optimized by changing the sequence in stem 2 to maximize ΔG according to the nearest neighbor thermodynamic parameters [186,187]. Additionally, the GAA triloop was shown to be the most stable DNA triloop sequence [188]. Simply changing the AT base pairs in MN19 to be GC base pairs, as in MN20, produced an increase in T_m value of 4.7 °C for the aptamer-quinine complex. By optimizing the sequence through staggering the GC base pairs, as in OR1, the T_m value of the aptamer-quinine complex increased to 44.0 °C. The final optimization step of replacing the AAA triloop with the more stable GAA triloop produced an improved T_m value for OR3•quinine to 44.2 °C. The increase in T_m values measured by UV melts was replicated using a differential scanning fluorimetry thermal shift assay (Figure 4.4). The T_m values obtained in these assays for both MN19•quinine and OR3•quinine matched those found using UV melting experiments to within the experimental error.

Presented results in this chapter in combination with other lab members' results, demonstrate that the OR3 construct is useful for researchers, who use the cocaine-binding aptamer in biosensor development because a great proportion of the aptamer•ligand complex will be folded using the OR3 sequence at room temperature (20-25 °C). Therefore, this should provide a more

intense signal in an assay (*i.e.,* electrochemical aptamer-based sensing) that depends on the structure-switching function of the aptamer.

The OR3 and MN19 aptamer constructs bound to cocaine were chosen for further stability analysis using the fluorescence-based thermal shift assay. Consistent with the lower binding affinity of MN19 and OR3 to cocaine than quinine, the MN19 and OR3 complexes with cocaine have a lower T_m value than their respective complexes with quinine. Additionally, as seen in the quinine complexes, the OR3•cocaine complex is more stable than the MN19•cocaine complex.

Our proposed mechanism for what is occurring is that the sequence changes made in OR3 have stabilized either the unbound aptamer state, but not enough to produce a folded unbound aptamer. Alternatively, it is possible that sequence changes in OR3 have stabilized the ligand-bound folded state with respect to MN19. I think that each ligand interacts with MN19 and OR3 with roughly the same ΔG value, less free energy from binding needs to go into folding the OR3 aptamer than the MN19 aptamer leaving more free energy to go into the observed binding free energy resulting in tighter binding observed for the OR3 aptamer and a higher melt temperature than we observe for MN19 (Figure 4.5).

Results presented here support a general mechanism where it is possible to destabilize an aptamer in order to improve ligand selectivity for tighter binding ligands. The trade-off for this improved selectivity is to gain a reduced affinity for the new aptamer-ligand pairing.

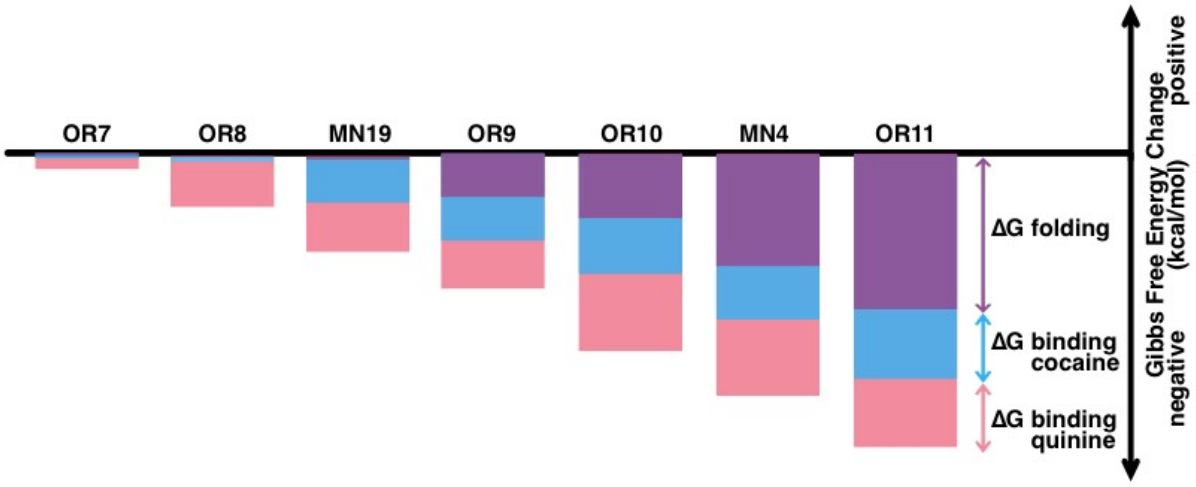

Figure 4.5 Free energy diagram outlining the binding scheme observed for the cocaine-binding aptamer with a varying stem 1 length. The horizontal black line indicates the level below which the aptamer or aptamer-ligand complex folds. The relative energy levels of unfolded states are not indicated.

In previous studies by Reinstein *et al.*, the reverse process was examined by adding a base pair to the deoxycholic acid steroid-binding aptamer to increase the stability of an aptamer, where a single base pair added in the terminal stem to improve the stability of the deoxycholic acid aptamer [66]. The aptamer was still unfolded while free and became structured with ligand binding. This increase in the stability of the free and unfolded, aptamer was needed due to the weak binding by the ligand (~15 μM) and consequently smaller amount of free energy available to contribute to folding. Figure 4.5 illustrates the thermal stability results combined with NMR and ITC results, performed by other lab members.

For OR8 and MN19 the unbound state is below the threshold for a fully structured aptamer whereas the free aptamer is folded for aptamers with a stem 1 four base-pairs and longer. The free energy of quinine binding is greater than that of cocaine binding as manifested in the tighter

binding of quinine compared to cocaine. These results suggest that the binding of a ligand interacts about equally with each folded unbound aptamer. This is shown by the ΔG of quinine and cocaine binding being within the error range for the aptamers OR9, OR10, MN4, and OR11. Additionally, the difference in the unbound free energy of OR9 to OR11 is roughly equal since they all differ by one GC base pair.

4.6 Conclusion

Thermal stability analyses presented in this chapter confirmed the development of a new cocaine-binding aptamer construct (OR3) that retains the ligand-induced structure-switching binding mechanism critical to biosensing applications, has a K_d value slightly tighter than the original MN19 aptamer, and has a significantly higher melt temperature when bound to both cocaine and quinine than observed for the original sequence.

The more favorable thermal stability characteristics of the OR3 aptamer should make it a useful construct of the cocaine-binding aptamer in biosensing applications. Furthermore, the stem 1 length optimization results provided here should suggest a direction for the development of surface-sensitive sensor techniques using the cocaine-binding aptamer. The use of an aptamer with 2 base pairs in stem 1, such as OR8, may provide a more sensitive sensor when using quinine as an analyte rather than the 3-base-pair-long MN19 because it may transition from an unfolded unbound state to a folded bound state.

The binding free energy supplied by quinine is enough to fold the OR8 and MN19 aptamer constructs, but cocaine binding only supplies enough free energy to fold MN19 and not the less

stable OR8. This implies more amount of free energy is required to fold OR8 than to fold MN19. For OR8, the free energy supplied by quinine binding is enough to fold the aptamer and supply an apparent K_d of (11.2 ± 0.5) μM. In contrast, the ΔG supplied by cocaine binding is not enough to fold this aptamer. Hence, no binding is observed with OR8-cocaine. For MN19, the ΔG supplied by both quinine and cocaine are enough to fold the aptamer with the excess amount resulting in the apparent K_d values of 0.47 μM and 21 μM, respectively, as previously discussed in Chapter 3 (Table 3.1).

Chapter 5: Analysis of the role played by ligand-induced folding of the cocaine-binding aptamer

5.1 Preface

Presented work in this chapter has been published in the article listed below [189]:

- **Shoara, A. A.**, Churcher, Z. R., Steele, T. W. J., and Johnson, P. E. (2020) Analysis of the role played by ligand-induced folding of the cocaine-binding aptamer in the photochrome aptamer switch assay. *Talanta*, 217, 121022.

5.2 Introduction

The Photochrome Aptamer Switch Assay (PHASA) is a fluorescence-based biosensing assay that exploits the ligand-induced folding, or adaptive binding mechanism, of an aptamer to alter the photoisomerization kinetics of stilbene. This change is consequently used to detect ligand binding by the aptamer [102,103,190]. As reviewed for photoisomerization in Section 1.4.2, the *trans*-isomer of stilbene is fluorescent, while the *cis* isomer has a much lower quantum yield at a given excitation wavelength (Figure 5.1).

When stilbene is irradiated with excitation light, the fluorescence decay rate for the *trans*-isomer is sensitive to the viscosity of its surrounding environment, its dynamics or spatial mobility, or some combination thereof [102]. Moreover, when the *trans*-isomer is attached to an aptamer that undergoes ligand-induced folding, the local viscosity and mobility of the stilbene becomes altered and as a result, the fluorescence decay changes.

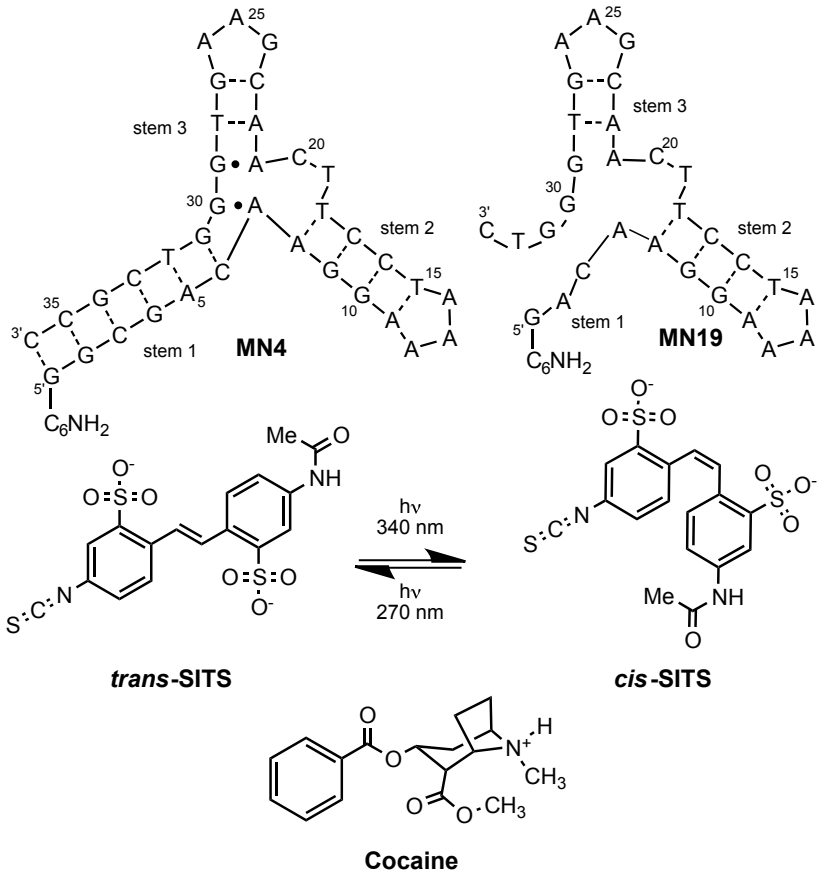

Figure 5.1 Shown are the sequences and secondary structures of the MN4 and MN19 aptamers with their 5′-C_6 amino (-$C_6H_{12}NH_2$) modifiers, the structure of cocaine and the structure of the SITS fluorescence tag in equilibrium between the *cis* and *trans* isomers. Nucleotides in both constructs are numbered in the same manner as in MN4. Dashes between nucleotides indicate Watson-Crick base pairs while dots indicate non-canonical base pairs.

The aptamer-stilbene conjugate combines a molecular recognition element (the aptamer) with stilbene acting as a fluorescent transducer, where a first-order decay in fluorescence quantifies ligand binding:

$$F = F_o e^{-k_{app}t} \qquad \text{Eq. 5.1}$$

where F_o is the fluorescence intensity at $t = 0$, and k_{app} is the apparent fluorescence decay rate in units of per second. This assay has the advantages that is independent of background fluorescence, does not require analyte separation, and the signal is detected quickly within seconds [103,190].

In this work, I demonstrate the general applicability of the PHASA by showing that this assay also functions using the cocaine-binding DNA aptamer. When stem 1 of the cocaine-binding aptamer contains three or fewer base pairs (Figure 5.1; MN19), the aptamer is unfolded or loosely folded in the free state, and folds in the presence of its ligand. When stem 1 contains four or more base pairs (Figure 5.1; MN4) the aptamer is folded in the free form and remains folded when bound, and little structural rearrangement occurs upon ligand binding [64,177,179]. Since the cocaine-binding aptamer was first selected [61], it has found widespread use in the development of biosensors mainly using the structure-switching version of the aptamer [62,146,150,180,191–193]. I think when the PHASA is used with the cocaine-binding aptamer, the short stem 1 version of the aptamer should display a larger change in fluorescence decay and would be more sensitive to cocaine binding than the long stem 1 version of the aptamer.

This study shows that the cocaine-binding aptamer, with its stem 1 length-dependent binding mechanism, is an excellent example of an aptamer model, where PHASA can be tested and utilized. In the present work, I attached the stilbene compound SITS (Figure 5.1) to the 5' end of two versions of the cocaine-binding aptamer. One version, MN19, undergoes a structure-switching binding mechanism while the other, MN4, is structured in the free state and little structure change occurs with ligand binding [64]. I used UV-based thermal melts of the aptamer-SITS conjugates to see how the addition of SITS affects the thermal stability of the aptamers. Then, the PHASA-derived limit of detection for cocaine was determined using both the MN4-SITS and MN19-SITS conjugates. Results presented in this chapter clearly demonstrate that the structure-switching aptamer is significantly more sensitive in cocaine detection.

5.3 Materials and Methods

5.3.1 Materials

SITS (4-acetamido-4′-isothiocyanato-2,2′-stilbenedisulfonic acid disodium salt) and cocaine hydrochloride samples were obtained from Sigma-Aldrich. In order to covalently link SITS to the aptamer constructs, the MN4 and MN19 sequences (Figure 5.1) were synthesized with a 5′-$C_6H_{12}NH_2$ (*n*-hexylamine) group. All aptamer samples were obtained from Integrated DNA Technologies (IDT). Prior to use, the DNA samples were dissolved in distilled deionized Milli-Q water (ddH_2O) and then exchanged three times using 3-kDa molecular weight cut-off concentrators with sterilized 1 M NaCl followed by three exchanges into ddH_2O. Aptamer, ligand and SITS concentrations were determined by UV absorbance spectroscopy using the extinction coefficients supplied by the manufacturers.

5.3.2 Aptamer-SITS conjugation

The covalent conjugations of MN4 and MN19 to *trans*-SITS were individually performed through the amine-isothiocyanate reaction [3]. To inhibit random photoisomerization of *trans*-SITS, all the SITS powder and solutions were kept under dark conditions. To allow the MN4 and MN19 aptamer constructs to anneal in an intermolecular manner, aptamer samples were incubated in a 95 °C water bath for 3 min and cooled in an ice-water bath for 5 min. Then, aptamer samples were allowed to equilibrate at 20 °C prior to the conjugation reaction. The MN4 and MN19 aptamers were mixed in 100-fold of molar excess SITS in 100 mM potassium bicarbonate buffer (pH 10) at 150 rpm shaking for at least 12 h under dark conditions to form the MN4-SITS and MN19-SITS aptamers, respectively. The conjugation reactions were done at 20 °C, which is below the expected thermal denaturation points (T_m) of these aptamer constructs, in order to retain their secondary

structures [176]. The aptamer-SITS products were washed and concentrated for 10 times using the described ultracentrifugation method. To confirm the 1:1 molar ratio of aptamer-SITS products, the relative UV absorbance at 260 nm and 340 nm of aptamer-SITS were measured.

5.3.3 Fluorescence decay kinetics

The analyses of fluorescence decay kinetics of MN4-SITS and MN19-SITS were performed in 20 mM Tris buffer (pH 7.4), 140 mM NaCl at 15 °C, 20 °C, 25 °C and 30 °C employing a Cary Eclipse fluorescence spectrophotometer and 10-mm fused quartz cuvettes. The temperature was maintained constant throughout each experiment using a Cary Peltier controller. Next, the spectrofluorometer was optimized for the limit of detection to maintain constant photomultiplier tube voltage, signal-to-noise ratio, and spectral bandwidth parameters. Since the studied DNA aptamers and cocaine had no light absorbance at (340 ± 10) nm, the inner-filter effect for the loss of the excitation light intensity was not calculated [194].

5.3.4 Structure-switching binding analysis by stilbene fluorescence anisotropy

We measured the fluorescence anisotropy decay of SITS as a function of cocaine concentration in 20 mM Tris buffer (pH 7.4), 140 mM NaCl at 15 °C. As discussed in Section 1.4.1, the fluorescence anisotropy of SITS depends on the ratio of the polarized light, and it is independent of the absolute emission intensity magnitudes [195,196]. Using a pair of manual Cary Eclipse light polarizers, the instrument grating factor (G) was measured as:

$$G = I_{hv}/I_{hh} \qquad \text{Eq. 5.2}$$

where I_{hv} is the integrated vertical emission intensity of SITS from 350 nm to 600 nm at the horizontal excitation at 340 nm. Also, I_{hh} is the integrated horizontal emission intensity of SITS

from 350 nm to 600 nm at the horizontal excitation at 340 nm. Then the polarized I_{vv} and I_{vh} at each titration point was measured as a function of decay time, and the fluorescence anisotropy (r) values calculated as in Eq. 5.3:

$$r = [I_{vv} - (GI_{vh})] / [I_{vv} + (2GI_{vh})] \quad \text{Eq. 5.3}$$

The results from three trials were averaged and plotted as a function of cocaine concentration [197,198]. To quantify the K_d values and compare the binding affinities obtained by this method with published data, the binding curves were fitted to a one-site binding function (Eq. 2.5) [104,195].

5.3.5 Method validation

The threshold of detection for the PHASA method employing the cocaine-binding aptamer conjugate and the C_{LoD} for cocaine binding were determined from the residual standard deviation of the regression data obtained from the least square regressions of the linear region of the dose-response curve [121,199]. I determined the C_{LoD} of cocaine using fluorescence kinetics decay of 1.0 μM aptamer-SITS with varying cocaine concentrations in both simple and complex matrices at 15 °C.

The obtained fluorescence kinetics decay constants (k_{app}) were plotted as a function of cocaine concentration. The C_{LoD} of aptamer-SITS and the C_{LoD} of cocaine were separately quantified as:

$$C_{LoD} = \frac{3S_{y/x}}{m} \quad \text{Eq. 5.4}$$

where $S_{y/x}$ is the calculated standard deviation of the linear regression residuals, and m is the fitted slope analyzed in the OriginPro software package [122,132]. The simple buffer solution consists

of 20 mM Tris buffer (pH 7.4) 140 mM NaCl. To examine the accuracy of the assay, the fluorescence decay kinetics of MN4-SITS and MN19-SITS were performed in a non-binding light absorbing complex matrix at 15 °C. The complex matrix conditions included the simple buffer components plus 50 μM each of: ATP, atropine sulfate, benzoic acid, choline, creatine phosphate, CTP, dapsone, glycine, GTP, isopropyl β-D-1-thiogalactopyranoside (IPTG), L-ascorbic acid, L-glutamic acid, triethylamine and UTP as well as 5.5 mM D-glucose and 140 mM glycerol.

A spike-recovery experiment was performed to assess the difference in the assay response. To perform a spike-recovery experiment, randomly selected known amount of cocaine was added to the experimental matrix and a standard buffer diluent, individually. Then, the two sets of responses were compared based on values obtained from a standard curve [123]. To evaluate the precision of this analysis, relative standard deviation (%RSD) of the mean standard values, or coefficient of variation (%CV), were calculated as:

$$\%CV = \frac{SD}{mean} \times 100 \qquad \text{Eq. 5.5}$$

The obtained CV values were then compared with the among-laboratory relative standard deviation (RSDR) using the Horwitz equation:

$$\%RSDR = 2^{(1-0.5logx)} \qquad \text{Eq. 5.6}$$

The linearity of each experiment was evaluated through a linear regression analysis of normalized k_{app} values versus cocaine concentration. Similarly, the range of linear detection threshold was evaluated in a calibration plot of fluorescence intensity of SITS as a function of conjugated aptamer-SITS concentration [123].

5.3.6 UV- monitored thermal denaturation

UV thermal melt experiments on MN4-SITS and MN19-SITS both free and cocaine-bound were performed using a Cary 100 spectrometer and 10 mm fused quartz cuvettes. The temperature increase rate for each experiment was 1 °C·min^{-1} as controlled by a Cary Peltier unit. The DNA melting curves were acquired in a temperature range from 5 °C to 75 °C. Each experiment was performed in 20 mM Tris buffer (pH 7.4), 140 mM NaCl. For each ligand-aptamer complex, a concentration of the aptamer-SITS was chosen to yield ~0.5 a.u. at 260 nm using extinction coefficients of the aptamer. The ligand to conjugated aptamer molar ratio was kept constant at 95% ligand-bound using Eq. 2.1. The data was acquired at 0.5 °C·min^{-1}. To quantify the thermal shift points, the first derivative of each thermal curve was plotted as a function of temperature using OriginPro software as described in Chapter 4 [132,176].

5.4 Results

5.4.1 Stability and structural analysis of SITS-modified aptamers

The thermal stability of the MN19-SITS and MN4-SITS conjugates free and cocaine-bound were assessed using UV spectroscopy and measuring the absorption at 260 nm (Figure 5.2). There is no statistical difference between the free and cocaine-bound MN4-SITS. The unbound MN4-SITS aptamer melts at (57.1 ± 0.8) °C while the cocaine•MN4-SITS complex melts at (57.1 ± 0.5) °C. The cocaine-bound MN19-SITS aptamer shows the typical sigmoidal transition for a folded molecule and melts at (33.0 ± 0.6) °C as displayed in Figure 5.2 a,b. The unbound MN19-SITS aptamer does not show a transition expected of a folded nucleic acid molecule. Instead, the absorption gradually increases as temperature rises (Figure 5.2 c,d).

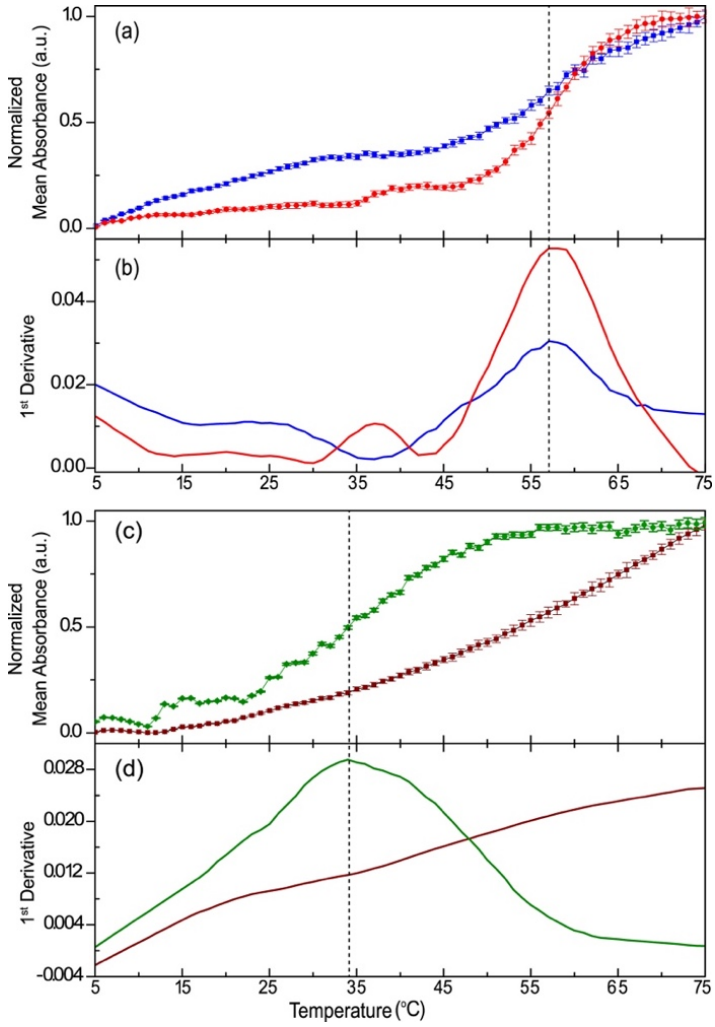

Figure 5.2 Analysis of thermal stability using UV melting curves. Displayed is the normalized UV absorbance at 260 nm for: (**a**, **b**) the free MN4-SITS (blue) and cocaine-bound MN4-SITS (red); (**c**, **d**) free MN19-SITS (brown) and cocaine-bound MN19-SITS (green). Dashed lines designate the T_m points of the aptamer. Each data point denotes an average of three experiments with the error bars corresponding to one standard deviation. Shown below each absorption plot are the first derivative curves. Data acquired in 20 mM Tris (pH 7.4), 140 mM NaCl.

The folding of the MN19-SITS aptamer was evaluated by other lab members using a 1D ^{1}H NMR spectroscopy in the absence and presence of cocaine. In the free state, MN19-SITS displays an NMR spectrum highly similar to what we previously observed for unconjugated and unbound MN19 [58,179].

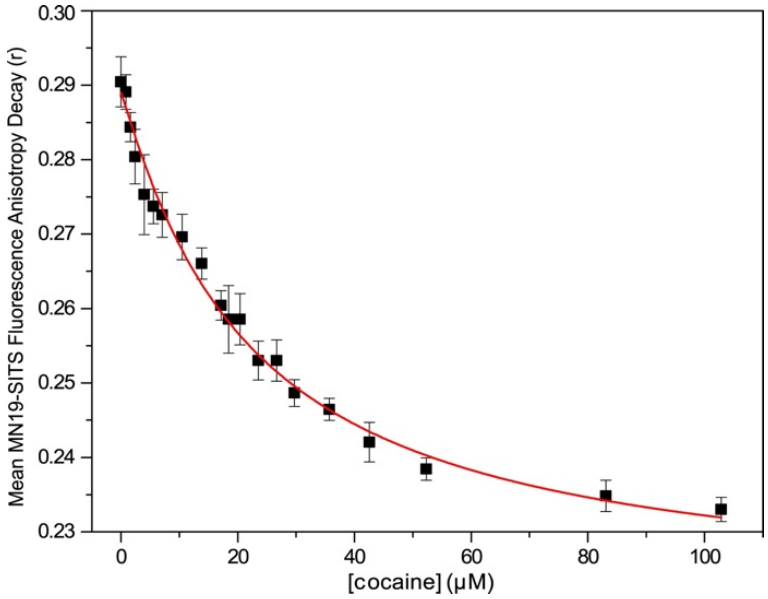

Figure 5.3 Fluorescence anisotropy decay plot of the MN19-SITS upon the addition of cocaine in 20 mM Tris (pH 7.4), 140 mM NaCl at 15 °C. The aptamer-SITS complex is excited at 340 nm and polarized decay emissions at 422 nm are detected as a function of ligand concentration. Error bars are one SD of at least three trials. Solid fitted line represents non-linear binding analysis using Eq. 2.5.

5.4.2 Determination of binding affinity using fluorescence anisotropy

We used fluorescence anisotropy to measure the binding affinity of the MN19-SITS aptamer to cocaine. Fluorescence anisotropy correlates to the hydrodynamic radius of the molecule for which the anisotropy is measured. As shown in Figure 5.3, I determined that the affinity of MN19-SITS for cocaine is (22 ± 3) μM at 15 °C by measuring the observed fluorescence polarization decay upon addition of cocaine.

5.4.3 Fluorescence kinetics of SITS as a function of cocaine concentration and temperature

We measured the fluorescence kinetics of MN19-SITS and MN4-SITS at constant intensity with excitation and emission settings positioned to detect the concentration of *trans*-stilbene.

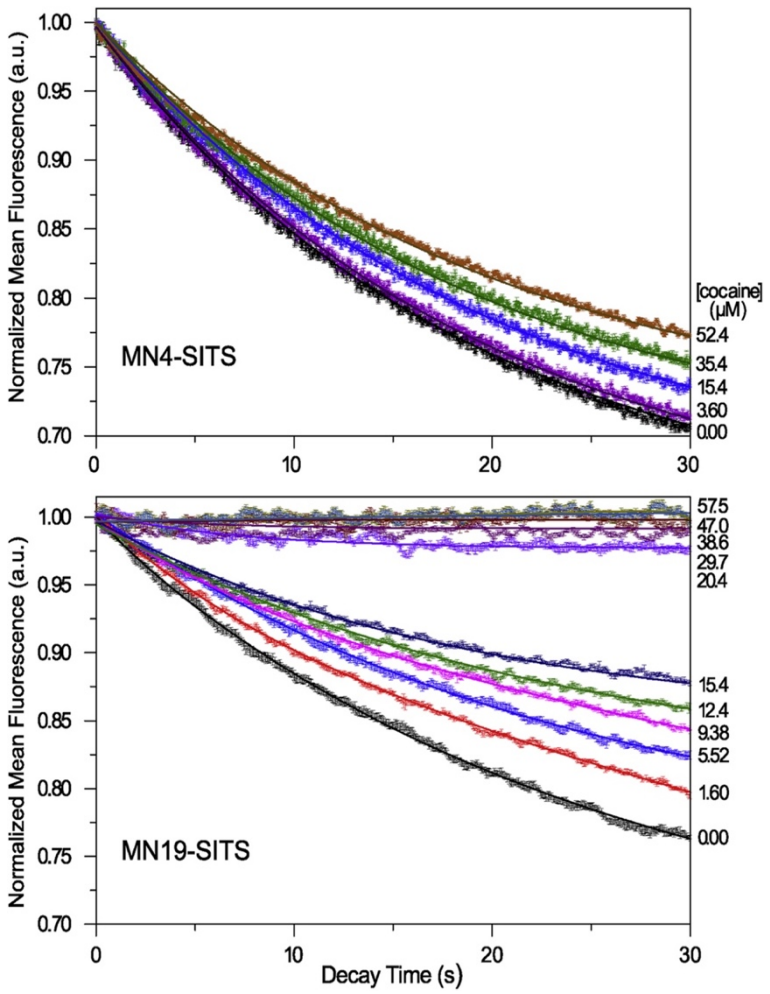

Figure 5.4 Fluorescence decay kinetics of MN4-SITS free and bound to cocaine (**top**) and MN19-SITS free and bound to cocaine (**bottom**). The aptamer-SITS conjugate is continuously excited at 340 nm and emissions at 422 nm are simultaneously detected as a function of time using a Cary Eclipse fluorescence spectrophotometer. Each normalized curve is fitted to the first-order decay function Eq. 5.1 (solid line) to quantify the apparent *trans-cis* decay kinetic constants (k_{app}). Triplicate experiments were performed in 20 mM Tris (pH 7.4), 140 mM NaCl at 15 °C.

First order decay was determined as a function of cocaine concentration (Figure 5.4). We observe that for the MN19-SITS aptamer, as the cocaine concentration increases, the apparent rate for the fluorescence decay decreases. For the MN4-SITS conjugate, the addition of cocaine did not alter the apparent decay rate to the extent it did for MN19-SITS (Figure 5.4). For MN19-SITS at 15 °C

and 20 °C, the addition of cocaine has a large effect on the measured k_{app} value as compared with MN4-SITS.

This observation is consistent with MN19-SITS undergoing ligand-induced folding at both of these temperatures (15 °C and 20 °C). However, the slopes of MN19-SITS did not exhibit a linear trend at 25 °C and 30 °C while the fits for MN4-SITS remained linear (Figure 5.5, Table 5.1). We attribute this to the fact that MN19-SITS is only partially folded below 25 °C (Figure 5.2), and consequently the slope of decay is relatively unchanged with ligand addition at 15 °C and 20 °C (Table 5.1). The slope of MN4-SITS does not change appreciably across these temperatures as this aptamer does not undergo ligand-induced folding, and consequently the apparent decay rates are relatively unchanged.

A series of stilbene fluorescence decay experiments were designed to evaluate non-specific stilbene interactions. Any possible stilbene interference was evaluated with the following conditions: (*i*) neat SITS, (*ii*) SITS + Aptamer, (*iii*) SITS + Ligand, (*iv*) SITS + Aptamer + Ligand. All of these experiments showed similar decay curves with the k_{app} values given in Table 5.2. None of these conditions showed any significant differences in the presence or absence of cocaine. This suggests that fluorescence decay of stilbene is not appreciably altered by non-specific interactions with free aptamer, ligand, or combination of the two. We quantified the apparent rates of decay as a function of cocaine concentration at temperatures of 15 °C, 20 °C, 25 °C, and 30 °C and plotted the normalized k_{app} against concentration of cocaine (Figure 5.5, Table 5.1).

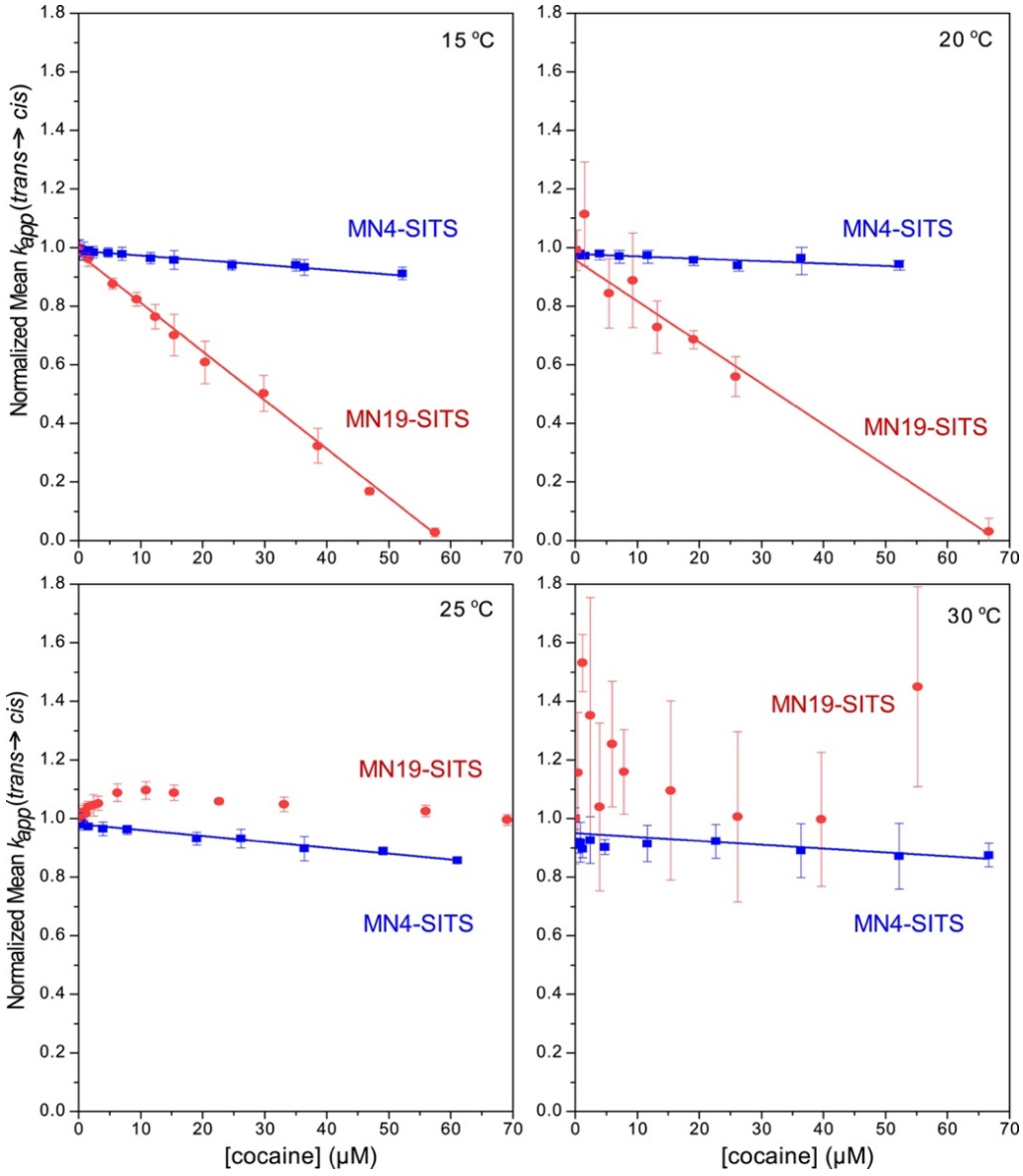

Figure 5.5 Plots of the measured apparent decay kinetic constants (k_{app}) of MN4-SITS (blue) and MN19-SITS (orange) as a function of cocaine concentration. Solid lines represent linear regression analyses. Obtained linear regression slopes are listed in Table 5.1 for statistical analysis. Data were acquired in triplicate with the standard deviation indicated by the error bars at the temperatures indicated on each panel.

Table 5.1 Linear regression values determined from measured apparent decay kinetic constants (k_{app}) versus cocaine concentration analyzed in Figure 5.5.

Linear regression parameters		MN4-SITS in simple buffer	MN19-SITS in simple buffer[1]	MN4-SITS in complex matrix[2]	MN19-SITS in complex matrix[2]
15 °C	Slope (μM^{-1})	$-1.6 \times 10^{-3} \pm 1.0 \times 10^{-4}$	$-1.7 \times 10^{-2} \pm 2.2 \times 10^{-4}$	$-3.1 \times 10^{-3} \pm 2.0 \times 10^{-4}$	$-1.5 \times 10^{-2} \pm 2.9 \times 10^{-4}$
	R^2	0.9948	0.9988	0.9937	0.9970
20 °C	Slope (μM^{-1})	$-8.3 \times 10^{-4} \pm 1.5 \times 10^{-4}$	$-1.4 \times 10^{-2} \pm 5.6 \times 10^{-4}$	ND	ND
	R^2	0.7438	0.9939	ND	ND
25 °C	Slope (μM^{-1})	$-2.0 \times 10^{-3} \pm 6.8 \times 10^{-5}$	$-2.7 \times 10^{-4} \pm 3.1 \times 10^{-4}$	ND	ND
	R^2	0.9898	0.0556	ND	ND
30 °C	Slope (μM^{-1})	$-1.3 \times 10^{-3} \pm 5.6 \times 10^{-4}$	$7.3 \times 10^{-3} \pm 7.6 \times 10^{-3}$	ND	ND
	R^2	0.9981	0.0704	ND	ND

[1]Samples in 20 mM Tris (pH 7.4), 140 mM NaCl.
[2]Complex matrix included the simple buffer components plus 50 µM each of: ATP, atropine sulfate, benzoic acid, choline, creatine phosphate, CTP, dapsone, glycine, GTP, IPTG, L-ascorbic acid, L-glutamic acid, triethylamine and UTP as well as 5.5 mM D-glucose and 140 mM glycerol.
Error is the standard error of the fit. Parameters that failed linearity were not plotted (shaded in gray). ND denotes Not Determined.

5.4.4 PHASA sensitivity using the cocaine-binding aptamer

The threshold of detection for the PHASA method with the cocaine-binding aptamer conjugate and the C_{LoD} for cocaine binding were determined in both buffer and a complex matrix (Figure 4.6) and are presented in Table 5.3. The threshold of detection for the PHASA method showed no statistical difference between the MN4-SITS and the MN19-SITS in buffer or in the complex matrix. When comparing the threshold of detection for the PHASA method between buffer and the complex matrix, the threshold is significantly lower in the buffer.

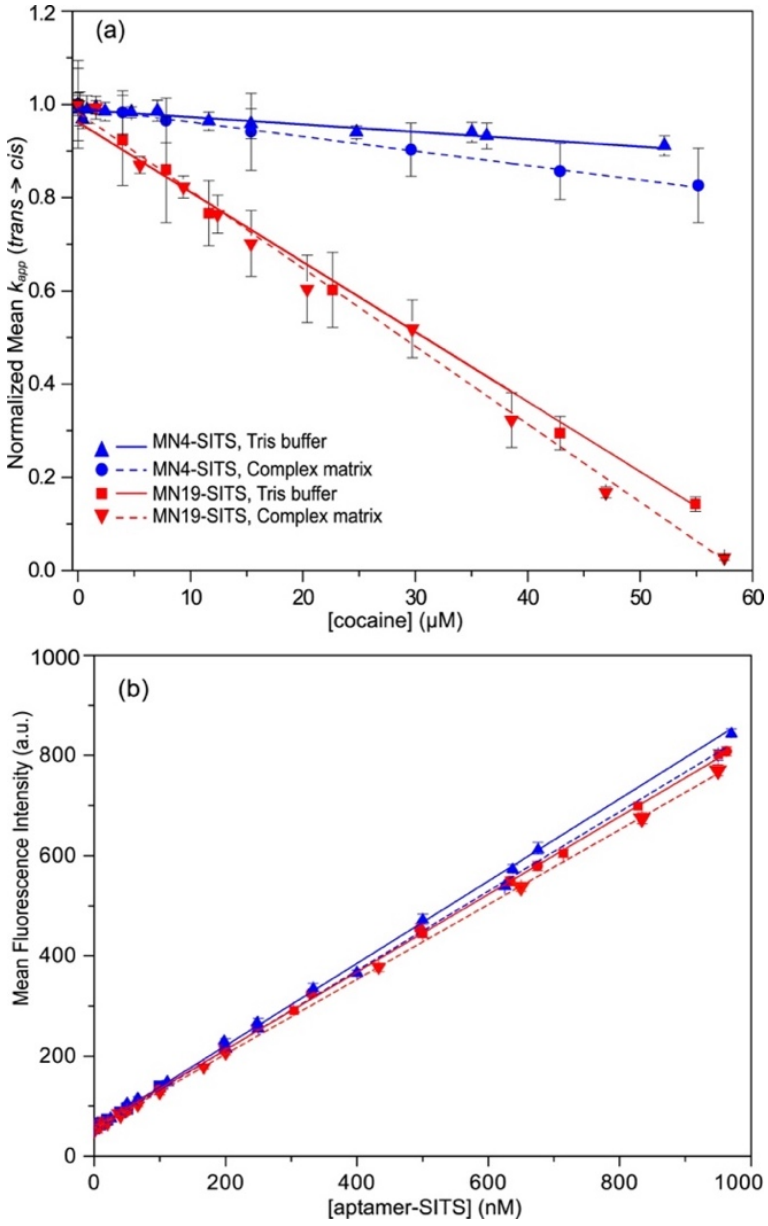

Figure 5.6 Aptamer sensor threshold and concentration limit of detection for the Photochrome Aptamer Switch Assay applied to the cocaine-binding aptamer. (**a**) Calibration plot for the measured apparent decay kinetic constants (k_{app}) of MN4-SITS (blue) and MN19-SITS (red) as a function of cocaine concentrations in the absence (solid line) and presence (dashed line) of a complex mixture. (**b**) Calibration plot for the measured fluorescence intensity of MN4-SITS and MN19-SITS in buffer and a complex mixture. All samples included 20 mM Tris (pH 7.4), 140 mM NaCl at 15 °C.

For cocaine binding, the C_{LoD} is significantly lower using MN19-SITS compared with the MN4-SITS conjugate (Figure 5.6). For both MN4-SITS and MN19-SITS binding cocaine the C_{LoD} is lower in the Tris buffer, but the difference is within the error range. Analytical performance for method validation such as spike-recovery test results are provided in Table 5.4.

Table 5.2 Results of the fluorescent decay experiments for the evaluation of non-specific interactions[1].

Sample	k_{app} (s^{-1})
SITS, MN19	0.054 ± 0.004
SITS, MN19, 50 µM cocaine	0.059 ± 0.005
Free SITS	0.054 ± 0.001
SITS, MN4	0.053 ± 0.003
SITS, MN4, 50 µM cocaine	0.052 ± 0.002
SITS, 50 µM cocaine	0.054 ± 0.004

[1]Samples in 20 mM Tris (pH 7.4), 140 mM NaCl at 15 °C. Error is the standard deviation in 10-15 replicates.

5.5 Discussion

5.5.1 Stability and structure of SITS-modified aptamers

We used a variety of biophysical methods to gauge what the effects of adding the SITS group to the 5′-end of the aptamer are to the thermal stability, the structure, and the binding affinity of the cocaine-binding aptamer. Our thermal melt results demonstrate that the attachment of SITS to the MN19 aptamer results in the cocaine•MN19-SITS complex increasing its melt temperature to (33.0 ± 0.6) °C (Figure 5.2). This is 6.4 °C higher than the T_m for the unconjugated MN19-cocaine complex [15]. There is no evidence in the thermal melt data that the unbound MN19-SITS is folded as its absorbance versus temperature graph behaves in a similar manner as we previously showed for the unmodified MN19 molecule (Figure 5.2) [169,176,177,179].

Table 5.3 Detection threshold and concentration limit of detection for the Photochrome Aptamer Switch Assay applied to the cocaine-binding aptamer[1].

	Sample	*Detection threshold (μM)*
Aptamer sensor signal	MN4-SITS (Tris buffer)	0.022 ± 0.002
	MN4-SITS (complex matrix)	0.030 ± 0.002
	MN19-SITS (Tris buffer)	0.024 ± 0.002
	MN19-SITS (complex matrix)	0.034 ± 0.003
	Sample	C_{LoD} *(μM)*
Cocaine detection	MN4-SITS (Tris buffer)	26 ± 2
	MN4-SITS (complex matrix)	30 ± 3
	MN19-SITS (Tris buffer)	8.6 ± 0.8
	MN19-SITS (complex matrix)	10 ± 1

[1]Data acquired at 15 °C. Error is the standard deviation in 3-6 trials.
Method validation is described in Section 5.3.5.

These data indicate that the addition of SITS stabilizes the bound MN19-SITS aptamer, possibly through hydrogen bonding and/or stacking interactions with the terminal base pair. In a previous molecular dynamics study of the malachite green-binding aptamer-SITS conjugate, the SITS group did, in fact, show evidence of hydrogen bond formation to the 5′ guanine nucleotide [190].

Similar stabilizations of nucleic acid structures have been seen previously with both dangling nucleotides [72,200], and with the addition of 5′ modifiers such as the Cy3 or Cy5 dye [201]. This stabilization of the cocaine-bound MN19-SITS by the addition of the SITS may

Table 5.4 Data obtained from spike-recovery method for accuracy validation

Standard [cocaine] (μM)		*Mean recovered [cocaine] (μM)*	*%RSD*	*%RSD$_R$*	*%Recovery*
Simple matrix[1]	1.59	1.82	2.46	1.83	51.6
	5.52	6.62	3.11	1.50	101.8
	9.00	9.72	4.50	1.42	96.9
	15.4	16.8	1.52	1.31	102.4
	57.5	57.3	2.11	1.09	98.0
Complex matrix[2]	3.00	3.52	5.80	1.65	87.3
	6.89	7.14	4.15	1.49	90.5
	11.9	12.3	5.22	1.37	95.7
	22.6	22.7	4.34	1.25	96.3
	55.0	54.9	4.85	1.09	98.2

[1]Samples in 20 mM Tris (pH 7.4), 140 mM NaCl.
[2]Complex matrix as described in Section 5.3. Data acquired for both simple and complex matrices at 15 °C. %RSD is the relative standard deviation in 10 replicates.
Method validation is described in Section 5.3.5.

prove useful in PHASA sensing applications, where there is only marginal stability of the folded ligand-bound aptamer is present, if stabilization is shown to be a general property of SITS addition.

The NMR data of the MN19-SITS conjugate, obtained by another lab member, show that the unbound MN19-SITS is unfolded, or loosely folded, in a manner we have previously shown for unconjugated MN19 and then folds or becomes much less dynamic with cocaine binding [64,177,179]. We were able to use fluorescence anisotropy methods using the SITS moiety to measure the affinity of the MN19-SITS aptamer for cocaine at 15 °C. The affinity measured here, (22 ± 3) μM (Figure 5.3) matches, within the error range, the value of (21.1 ± 0.6) μM

reported previously using the fluorescence quenching of the ligand at the same temperature and in the same buffer conditions [104]. This K_d value is also within the range of the values reported using isothermal titration calorimetry (ITC) methods though measured at different temperatures. These ITC-derived values are (17 ± 3) μM at 10 °C and (26.7 ± 0.7) μM at 20 °C [58,118]. These data show that the addition of the SITS to MN19 has no measurable effect on the binding affinity of the aptamer for cocaine.

5.5.2 The PHASA method is most sensitive using a structure switching aptamer

We used both a structure-switching (MN19) and a non-structure switching (MN4) version of the cocaine-binding aptamer to show that the photochrome aptamer switch assay is most sensitive when used with the structure-switching aptamer. The change in fluorescence intensity is greatest (Figures 5.4, 5.5), and the C_{LoD} for cocaine binding is lower (Figure 5.6) when the MN19 aptamer is used compared to when the MN4 aptamer is used. This better performance of the structure switching aptamer in the PHASA is consistent with our hypothesis that aptamers with a greater amount of structural change will better perform in this assay. A corollary of this finding would be that a greater change in fluorescence intensity in the PHASA can be used to identify, between related aptamers, which one undergoes more structural change with ligand binding. Despite MN4 not performing as well as MN19, the PHASA did work with the MN4 aptamer (Figures 5.4, 5.5).

The MN4 aptamer is thought to have little to no structural change occurring with cocaine binding [64]. However, the binding site at the three-way junction is thought to tighten or rigidify with cocaine binding based on the changes in the NMR-measured imino proton exchange rates [179]. This implies that the PHASA may work, albeit with reduced sensitivity, with non-

structure switching aptamers (MN4). This would significantly increase the usefulness of PHASA in biosensing. The obtained C_{LoD} for cocaine binding that I determined in this study (Table 5.3) using the MN19-SITS conjugate is within the range of values previously published (0.9–10 μM) that also use the short stem 1 structure-switching cocaine-binding aptamer [65,192]. This includes other optical-based cocaine-binding aptamer-based sensors applications [63,152]. The higher C_{LoD} values we observe in a complex matrix versus the simple buffer condition is likely due to differences in the sample matrix. It is worth noting that there is a trade-off of sensitivity in the PHASA in comparison with other aptamer detection methods in return for a quick assay, and it may be useful in applications such as in-line sensors in wastewater.

5.5.3 Optimizing the limit of detection

The limit of detection in this assay may be improved through optimization of the aptamer/ligand interaction through modeling, by exploiting the reversible photoisomerization (*cis* → *trans*) of stilbene, or through exploring other fluorescent switches, such as azobenzene, to sense kinetics decays in nano- or picosecond scales [103,190,202]. Also, employing laser-induced fluorescence techniques can report sudden alteration in SITS photoisomerization. In these methods, the conjugated SITS is excited to a higher energy level by the absorption of laser light and fluorescence decay is spontaneously monitored [203].

5.6 Conclusion

The hypothesis of this project was that when the PHASA is used with the cocaine-binding aptamer, the short stem 1 version of the cocaine-binding aptamer (MN19) would display a larger change in fluorescence decay and would show signals of subtle changes with cocaine binding than the long stem 1 version of the aptamer. Discussed results in combination with the statistical analysis and method validation performed in this chapter approve this hypothesis. We note that the cocaine-binding aptamer, with its stem 1 length-dependent binding mechanism, is an excellent example of an aptamer, where PHASA method can be tested. The next chapter presents two examples demonstrating MN19-SITS utilization proved beneficial.

Chapter 6: Two applications of the photochrome aptamer switch assay

6.1 Preface

Presented work in this chapter has been published in the articles listed below [204,205]:

- **Shoara, A. A.**, Churcher, Z. R., Slavkovic, S., and Johnson, P.E. (2021) Weak binding of levamisole by the cocaine-binding aptamer does not interfere with an aptamer-based detection assay. *ACS Omega.* 6 (37) 24209-24217.

- Slavkovic, S., **Shoara, A.A.**, Churcher, Z.R., Daems, E., Wael, K., Sobott, F., and Johnson, P.E. (2022) DNA binding by the antimalarial compound artemisinin. *Sci. Reports*. 12, 133.

6.2 Introduction

6.2.1 Application of aptamer-based cocaine detection in presence of levamisole

Levamisole is a pharmaceutical compound used to treat parasitic worm infections in humans and animals (Figure 6.1). As discussed in Chapter 1, levamisole is a commonly used adulterant of cocaine that causes serious debilitating inflammatory complications and skin necrosis [206–208]. The presence of levamisole in illicit cocaine samples also has the effect of interfering with electrochemical-based detection methods for cocaine by giving false negative readings when above a 1:1 molar ratio [209]. At present, it is unknown whether levamisole can interfere with aptamer-based assays for cocaine.

6.2.2 Application of PHASA for artemisinin-aptamer binding analysis

Artemisinin (ART) is derived from the plant *Artemisia annua*, and it is a vital medicinal compound that is used alone or as part of a combination therapy against malaria (Figure 6.1). ART is thought to function by attaching to heme covalently and alkylating a range of proteins [210]. Using a

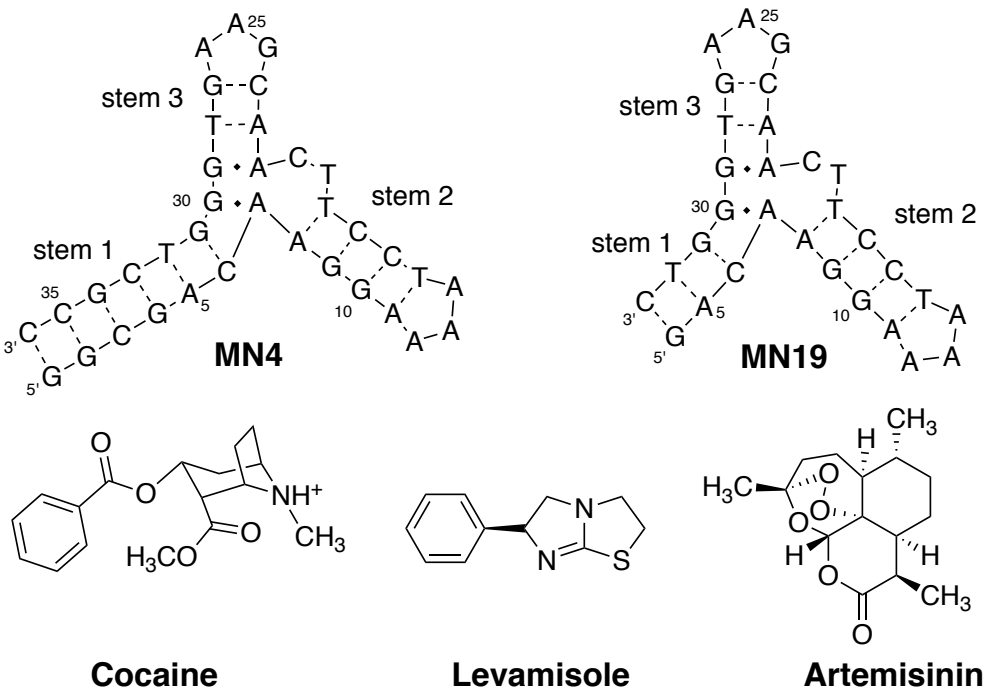

Figure 6.1 Structures of the cocaine-binding aptamers MN4 and MN19 as well as the compounds levamisole, cocaine, and artemisinin (ART). Nucleotides in both constructs are numbered in the same manner as in MN4. Dashes between nucleotides indicate Watson-Crick base pairs while dots indicate non-canonical base pairs.

combination of biophysical methods, we demonstrated that ART is bound by three-way junction and duplex containing DNA molecules.

Binding of ART by DNA was first shown for the cocaine-binding DNA aptamer and extensively studied using this DNA molecule. Binding analyses demonstrated in this study coupled with mass spectrometry, NMR and ITC studies show that ART binds at the three-way junction of the cocaine-binding aptamer, and that binding results in the folding of the structure-switching variant of the cocaine-binding aptamer (Figure 6.1, MN19) [70,177,179]. This structure-switching ability was exploited using the photochrome aptamer switch assay to demonstrate that ART can

be detected using this biosensing assay [102,189]. This study was the first to demonstrate the DNA binding ability of ART and furnished the foundation for further work to study implications of DNA binding for the antimalarial activity of ART.

In this chapter, I aim to demonstrate two independent applications of aptamer-based techniques that were discussed in Chapter 4 and Chapter 5: (*i*) to determine if levamisole binds the cocaine-binding aptamer and therefore potentially interfere with an aptamer-based assay for cocaine detection, and (*ii)* to study if artemisinin binds the cocaine-binding aptamer [102,189]. I use thermal melt techniques and the photochrome aptamer switch assay (PHASA) to show that at micromolar concentrations of aptamer, levamisole does not bind the cocaine-binding aptamer. Next, I use the same stated methods to show artemisinin binds the cocaine-binding aptamer.

6.3 Materials and Methods

The cocaine-binding aptamer construct (Figure 6.1, MN19) was obtained from Integrated DNA Technologies (IDT, Coralville, Iowa) and used without further purification. DNA samples were prepared in the same manner as explained in Chapter 2. The covalent conjugation of MN19 to *trans*-SITS was performed through the amine isothiocyanate reaction as discussed in Section 5.3 [102,189].

6.3.1 UV melts for levamisole studies

UV thermal melt experiments of MN19-SITS in presence and absence of levamisole were performed using a Cary 100 spectrophotometer in the same manner as explained in Section 4.3. The DNA melting curves were acquired in a temperature range from 10 °C to 80 °C. Experiments

were performed in triplicate in a complex mixture described previously containing 20 mM Tris buffer, pH 7.4, 140 mM NaCl, and 1.1 mM levamisole [189]. For each levamisole-aptamer mixture, a concentration of 0.97 μM the MN19-SITS was chosen to yield ~0.8 a.u. at 260 nm. The levamisole concentration was kept at ~1000-fold of the conjugated aptamer concentration. To quantify the thermal shift points (T_m), the first derivative of each thermal curve was plotted as a function of temperature.

6.3.2 UV-monitored thermal denaturation for artemisinin studies

UV melt experiments of the unbound and ART-bound MN19 aptamer, were performed using a Cary 100 UV–Vis spectrometer and 10-mm fused quartz cuvettes. Each experiment was performed in three trials in PBS buffer (10 mM sodium phosphate buffer, pH 7.4, 2.7 mM KCl, 137 mM NaCl). 3% v/v acetonitrile (ACN) added to the buffer instead of DMSO to avoid errors caused by the freezing point of DMSO at ~ 19 °C. All solutions were filter-sterilized using a 0.2 μm microfilter. The rate of temperature was increased at 1 °C·min^{-1} and controlled by a Cary Peltier unit. Two data points were acquired per minute in a temperature range from 15 °C to 75 °C. Data were analyzed in a range of 15 °C to 65 °C to eliminate background signals associated with the boiling temperature of acetonitrile. For each trial, (1.7 ± 0.1) μM MN19 was chosen to yield ~ 0.5 a.u. at 260 nm using the extinction coefficients of the aptamer. The ligand to aptamer molar ratio was kept constant at 95% ligand-bound using Eq. 2.1. Quinine was used as the positive control ligand, and ART in PBS plus 3% ACN was used as the blank for MN19•ART experiments. For the unbound MN19 experiments, PBS plus 3% ACN was used as the blank. To quantify the thermal denaturation points (T_m), the obtained data from blanks were subtracted from their

corresponding experimental values, and the first-order derivative of each thermal curve was plotted as a function of temperature using OriginPro software as described previously [132,176].

6.3.3 Fluorescence anisotropy for levamisole studies

I utilized the structure-switching binding mechanism of MN19-SITS in a fluorescence anisotropy assay of MN19-SITS as a function of cocaine concentration in the previously described complex mixture at 15 °C. The fluorescence anisotropy of SITS is governed by the ratio of the polarized light, and it is independent of the absolute emission intensity magnitudes [195]. Using a pair of manual Cary Eclipse light polarizers, the instrument grating factor (G) was measured according to Eq. 5.2 at emission intensity of SITS from 350 to 600 nm and the horizontal excitation at 340 nm. Also, the integrated horizontal emission intensity of SITS measured from 350 nm to 600 nm to include the maximum emission peak at 422 nm at the horizontal excitation at 340 nm.

The polarized emissions were obtained as a function of cocaine concentration, and the fluorescence anisotropy (r) values calculated as stated in Eq. 5.3. The results from five trials were averaged and plotted as a function of cocaine concentration. To quantify the K_d values and compare the affinities obtained by this method with previously published data, the binding curves were fitted to a one-site binding function (Eq. 2.5) and analyzed using OriginPro as described in Chapter 2 [104,132].

6.3.4 PHASA method for levamisole studies

The fluorescence decay kinetics of MN19-SITS in the absence and presence of levamisole were examined in 20 mM Tris buffer (pH 7.4) and 140 mM NaCl at 15 °C using a Cary Eclipse

fluorescence spectrophotometer and 10 mm fused quartz cuvettes. Then, the fluorescence decay kinetics of MN19-SITS analyzed titrations of cocaine solutions in a complex matrix at 15 °C as described in Chapter 5.

The complex matrix conditions included 20 mM Tris buffer (pH 7.4), 140 mM NaCl, and 50 μM each of ATP, atropine sulfate, benzoic acid, choline, creatine phosphate, CTP, dapsone, glycine, GTP, isopropyl β-d-1-thiogalactopyranoside (IPTG), l-ascorbic acid, l-glutamic acid, triethylamine, and UTP as well as 5.5 mM d-glucose, 140 mM glycerol, and 150 μM levamisole. The temperature was kept constant during each trial using a Cary Peltier controller. The spectrofluorometer was optimized for the limit of detection to maintain a constant signal-to-noise ratio, photomultiplier tube voltage, and spectral bandwidth parameters. Maximum UV-Vis absorbance and steady-state fluorescence emission wavelengths of levamisole were tested in 20 mM Tris buffer (pH 7.4) and 140 mM NaCl at 15 °C for the inner-filter effect measurements. Since the studied DNA aptamer, cocaine, or levamisole had no light absorbance at (340 ± 10) nm, the inner-filter effects for the loss of the excitation and emission light intensities were not calculated [211]. Method validation steps was performed as described in Section 5.3.5 [122,123].

6.3.5 PHASA method for artemisinin studies

The fluorescence decay kinetics of 0.1 μM MN19-SITS were analyzed in 20 mM Tris buffer (pH 7.4), 140 mM NaCl, 3% v/v DMSO at 20 °C as a function of artemisinin concentration (zero to 4.2 μM ART) as described in Section 5.3. Since MN19 and ART had no light absorbance at (340 ± 10) nm, the inner-filter effect for the loss of the excitation light intensity was not considered. An unbound ART solution in the binding buffer was used as the blank. The experimental and blank

samples were excited at 340 nm and emitted light intensities at 422 nm were simultaneously detected as a function of time in milliseconds. The obtained fluorescence decay kinetics were normalized as F/F_o and fitted to the first-order decay. The quantified average k_{app} values for each titration point were normalized and analyzed against ART concentration.

The concentration limit of detection (C_{LoD}) of ART was quantified from the residual standard deviation of the regression data obtained from the linear region of the dose-response curve in a manner as described in Section 5.3. Additionally, the ratio of k_{app} in the presence of ART to k_{app} of unbound MN19-SITS were analyzed as a function of ART concentration and fitted to a linear plot. The obtained linear slope was used to compare with previously published values, discussed in Chapter 5, for ligand-induced folding of the MN19 aptamer binding cocaine [189].

6.4 Results and Discussion

6.4.1 Levamisole studies

To study whether levamisole affects the thermal stability of MN19-SITS, and therefore interfere with the PHASA assay, UV-monitored thermal melt experiments on MN19-SITS in the presence and absence of levamisole were performed. Experiments were run with MN19-SITS at 0.97 μM. I did not observe any significant difference between the thermal melts of MN19-SITS with or without 1 mM levamisole added (Figure 6.2). The first derivative analyses of these melting plots, while the aptamer is unbound to cocaine, did not show a transition expected for a folded nucleic acid molecule. This indicates that levamisole does not bind and stabilize MN19-SITS in the manner that the binding of cocaine or quinine does [176,177].

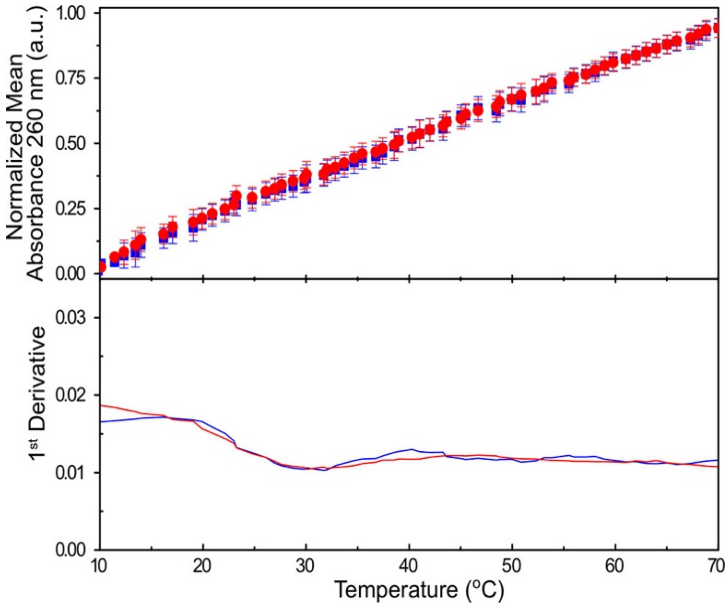

Figure 6.2 Analysis of the thermal stability of MN19 using UV melting curves. Displayed is the normalized UV absorbance at 260 nm for the MN19-SITS without levamisole (red) and MN19-SITS with 1.1 mM levamisole (blue). Each data point denotes an average of three experiments with the error bars corresponding to one standard deviation. Shown below each absorption plot are the first derivative analyses. Data acquired with 0.97 µM MN19-SITS in 20 mM Tris (pH 7.4), 140 mM NaCl.

I used fluorescence anisotropy to measure the binding affinity of the MN19-SITS aptamer to cocaine in the presence of levamisole. Fluorescence anisotropy correlates to the rotational diffusion of MN19-SITS undergoing Brownian motion of the macromolecule for which the anisotropy is measured. By quantifying the observed polarized fluorescence emitted from SITS upon addition of cocaine, I was able to determine the affinity of MN19-SITS for cocaine is (19.8 ± 0.9) µM at 15 °C in a complex matrix containing levamisole (Figure 6.3). The obtained affinity values agree with published K_d values using ITC and intrinsic fluorometry methods [58,104]. To validate our method, I measured the concentration limit of detection (C_{LoD}) of cocaine (10 ± 1) µM at 15 °C. The obtained C_{LoD} agrees with our published data [189].

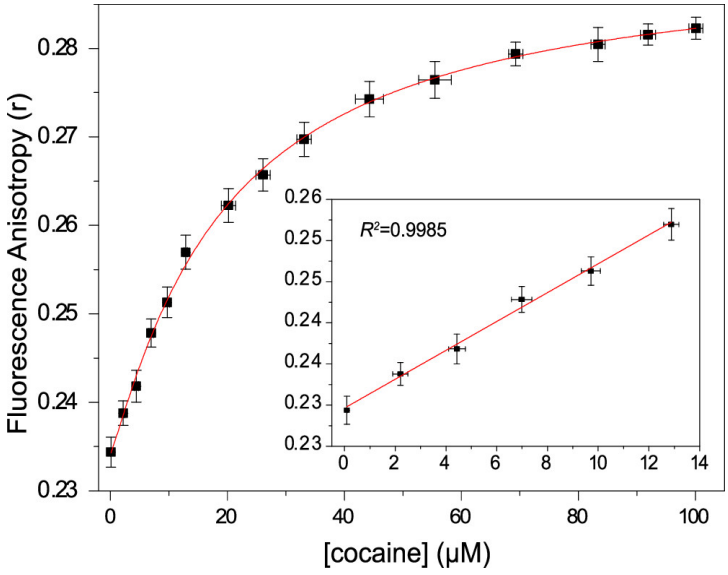

Figure 6.3 Fluorescence anisotropy assay for cocaine detection. Shown is the measured fluorescence anisotropy of MN19-SITS as a function of cocaine concentration in a complex matrix containing 150 μM levamisole, 20 mM Tris (pH 7.4), and 140 mM NaCl at 15 °C. The solution is excited at 340 nm and fluorescence anisotropy of MN19-SITS is detected in an emission range of 350-600 nm. Nonlinear regression analysis was used to quantify the apparent K_d of cocaine. The inset displays the linear portion of the plot that is used to calculate the concentration limit of detection (C_{LoD}) of cocaine. Error bars are the experimental standard deviation of five trials.

I measured the fluorescence kinetics of 0.50 μM MN19-SITS in 20 mM Tris buffer (pH 7.4), 140 mM NaCl at 15 °C, constant excitation of 340 nm, and an emission of 422 nm to detect the effect of levamisole concentration on the photoisomerization of *trans*-stilbene. I did not detect any significant alterations in the k_{app} of MN19-SITS versus levamisole (Figure 6.4). Further analyses of 0.50 μM MN19-SITS as a function of cocaine concentration in a complex matrix that also contains levamisole showed that the apparent rate for the fluorescence kinetics decay (k_{app}) decreases as the cocaine concentration increases. The linear slope of measured k_{app} constants of MN19-SITS as a function of cocaine concentration in a complex matrix including levamisole agrees with that in the same complex matrix without levamisole.

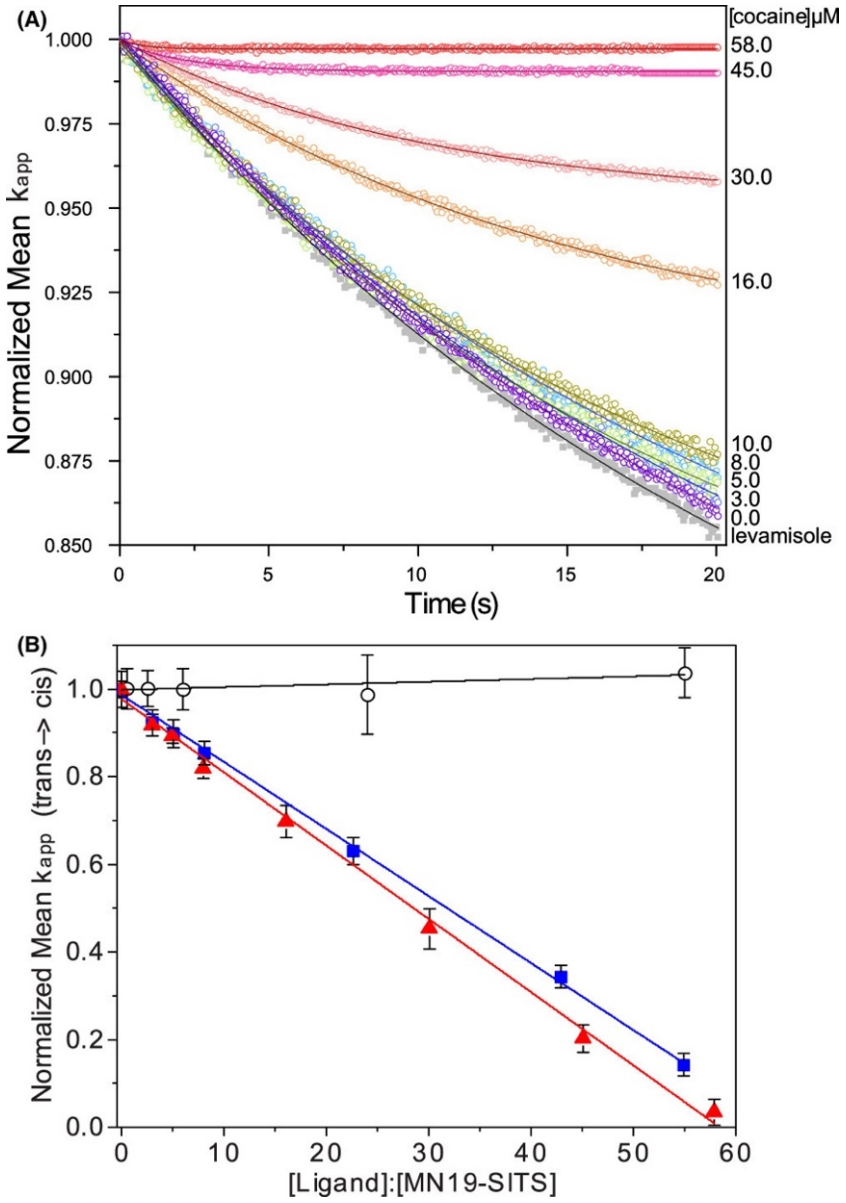

Figure 6.4 Photochrome aptamer switch assay (PHASA) applied to detect cocaine in a mixture containing levamisole. (**A)** shows the fluorescence decay kinetics curves of MN19-SITS titration with cocaine in a complex matrix containing 150 μM levamisole, 20 mM Tris (pH 7.4), and 140 mM NaCl at 15 °C. The gray curve represents the negative control (150 μM levamisole in complex matrix without cocaine). (**B)** displays normalized linear plots of observed k_{app} values as a function of the ligand to MN19-SITS molar ratio. The aptamer-SITS conjugate is continuously excited at 340 nm, and emissions at 422 nm are simultaneously detected as a function of time in milliseconds. Red triangles represent cocaine titration in MN19-SITS in a complex matrix containing levamisole; blue squares denote cocaine titration in MN19-SITS and Tris buffer; and black circles signify levamisole titration in MN19-SITS and complex matrix.

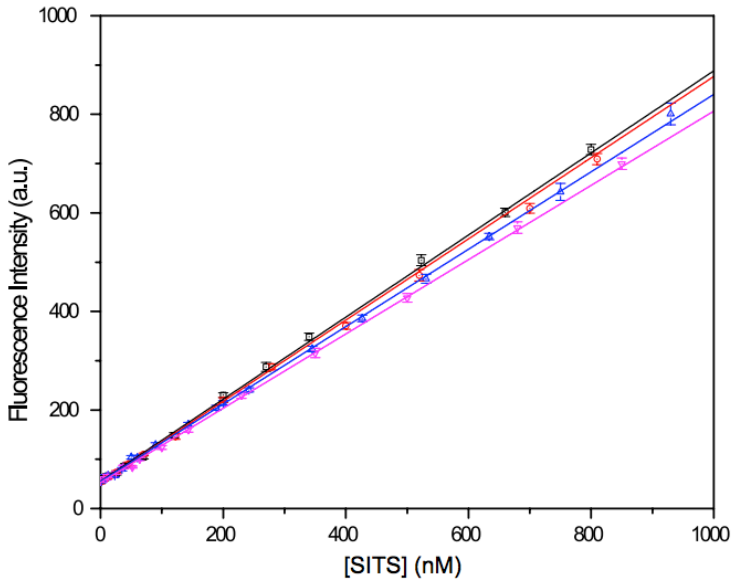

Figure 6.5 SITS sensing threshold for the Photochrome Aptamer Switch Assay applied to the cocaine-binding aptamer. Shown is the calibration plot for the measured fluorescence intensity of unconjugated SITS (black line) and equimolar mixture of unconjugated SITS and MN19 (red line) in 20 mM Tris buffer, pH 7.4,140 mM NaCl, and unconjugated SITS (blue line) and equimolar mixture of unconjugated SITS and MN19 (purple line) in a complex matrix containing 150 µM levamisole, 20 mM Tris buffer, pH 7.4, 140 mM NaCl. Triplicated samples were examined at 15 °C. Error bars denote one standard deviation.

For a negative control experiment, unconjugated stilbene fluorescence was examined to evaluate non-specific interactions of levamisole in both Tris buffer and the complex matrix (Figure 6.5). None of the examined conditions exhibited any significant differences in the presence or absence of levamisole.

6.4.2 Artemisinin studies

The binding of ART by MN19 and stabilization of MN19 cocaine-binding aptamer was demonstrated by measuring the thermal stability of the unbound MN19 as well as the ART-bound and quinine-bound MN19 aptamers (Figure 6.6). The DNA UV absorbance at 260 nm of unbound MN19 aptamer does not show a shift observed previously [190], and as expected for a loosely

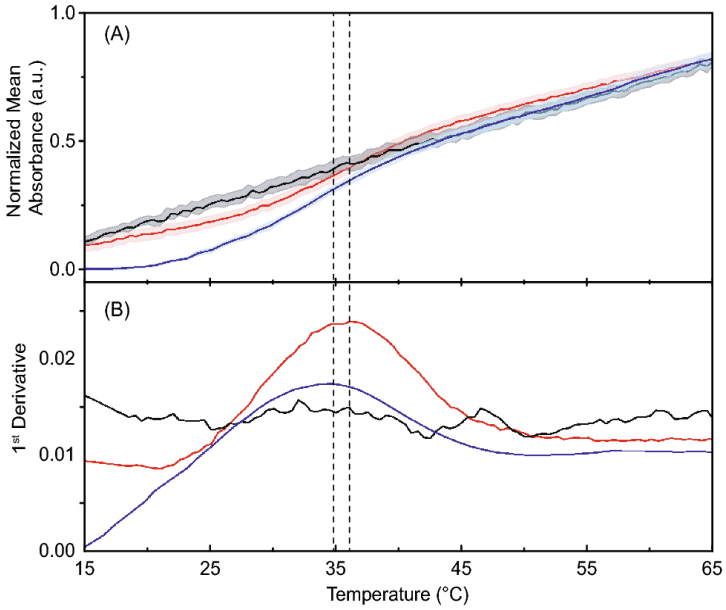

Figure 6.6 Analysis of the thermal stability of MN19 free and ligand-bound using UV melting plots. Shown in (**A**) are the normalized average of UV absorbance values at 260 nm versus temperature for the unbound MN19 (black), ART-bound MN19 (blue), and quinine-bound MN19 (red) as a positive control. Displayed in (**B**) are the first derivative plots. Dashed lines indicate the obtained T_m points of the aptamer. Data acquired in PBS (pH 7.4), 3% (v/v) acetonitrile. Each data point denotes an average of three experiments with the error ribbons corresponding to one standard deviation.

folded or unfolded nucleic acid molecule. For free MN19, the UV absorption increases linearly with temperature (Figure 6.6).

The MN19•ART shows a sigmoidal transition from folded to unfolded molecule with a thermal denaturation point at (34.8 ± 1.1) °C. The MN19·quinine complex was tested as the positive control, where it shows a sigmoidal transition with a thermal denaturation at (36.4 ± 1.2) °C. This unfolding temperature of MN19•quinine is consistent with our prior measurements [70,190]. These data confirm ART binding by the MN19 cocaine-binding aptamer and confirm the ART complex is slightly less thermally stable than with quinine as suggested by the NMR-monitored melt.

As the UV-monitored melt and NMR (not shown here) data indicate the folding of MN19 with ART binding, I applied the photochrome aptamer switch assay (PHASA) [195] for MN19-SITS both free and ART-bound in PBS plus 3% (v/v) DMSO at 20 °C and constant instrumental settings ($\lambda_{ex} = 340$ nm and $\lambda_{em} = 422$ nm). I measured the fluorescence decay of MN19-SITS to detect the kinetics rate due to internal conversion of *trans*- to *cis*-stilbene. First-order decay analysis was used to determine the apparent kinetics rates (k_{app}) (Figure 6.7A). Using the calibration plot for the normalized average k_{app} values of MN19-SITS against ART concentrations, I obtained the concentration limit of detection (C_{LoD}) as (0.22 ± 0.02) μM (Figure 6.7B). The ratio of average k_{app}, in the presence of ART, to average k_{app} of unbound MN19-SITS were analyzed as a function of ART concentration (Figure 6.8). The observed linear trend shows that the apparent rate for MN19-SITS decreases as the ART concentration increases. This observation is consistent with the presence of ART inducing the folding of MN19-SITS at 20 °C. Moreover, I obtained a linear slope of (-0.16 ± 0.01) μM^{-1} (Figure 6.8). The quantified slope agrees with previously published data for MN19-SITS bound to cocaine [195].

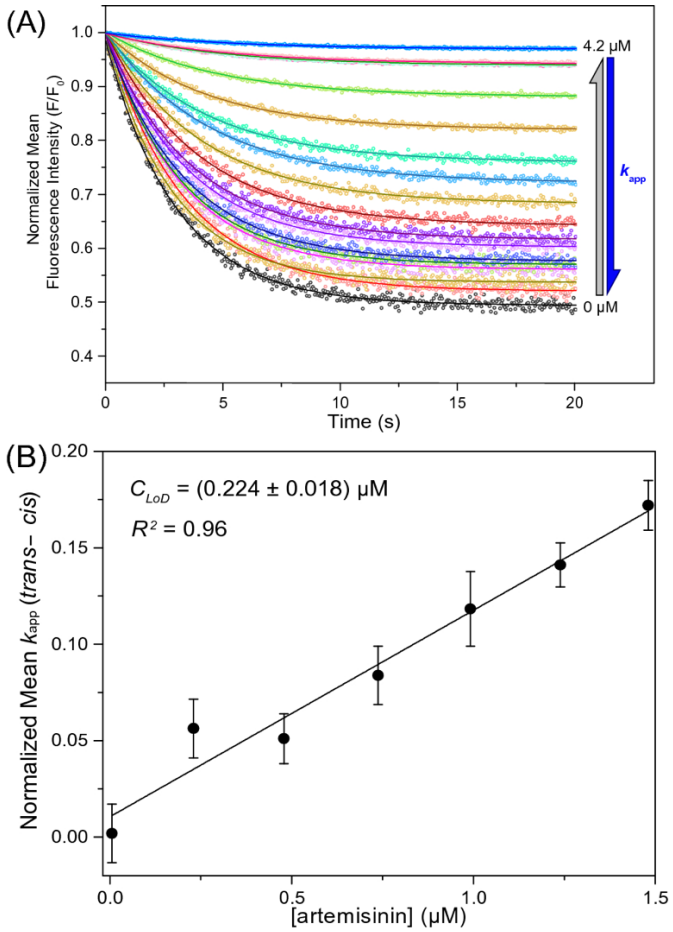

Figure 6.7 Detection of ART using the photochrome aptamer switch assay. (**A**) displays fluorescence decay plots of 0.1 μM unbound MN19-SITS (black) and as a function of zero to 4.2 μM ART concentration (light blue). The MN19-SITS is continuously excited at 340 nm and the emission intensities at 422 nm are simultaneously detected as a function of time. Each normalized decay plot is fitted to the first-order decay function (solid lines) to quantify the apparent *trans–cis* decay kinetics (Eq. 5.1; k_{app}). (**B**) shows a calibration plot for the normalized average k_{app} values of MN19-SITS against ART concentrations. The concentration limit of detection (C_{LoD}) obtained is (0.22 ± 0.02) μM. Triplicated experiments were performed in 20 mM Tris (pH 7.4), 140 mM NaCl at 20 °C. The error bars correspond to one standard deviation.

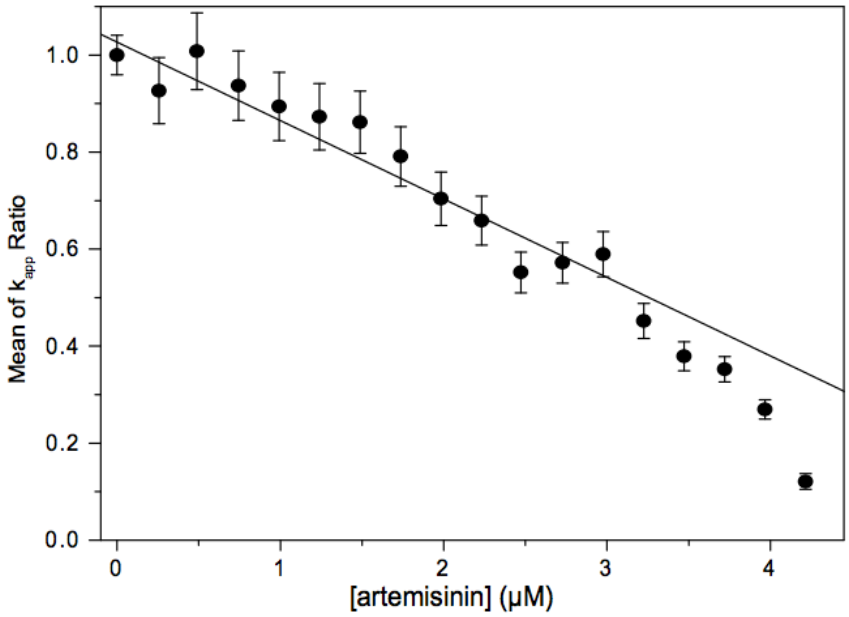

Figure 6.8 Exhibits a calibration plot for the normalized average k_{app} values of MN19-SITS against artemisinin concentrations. The obtained linear slope = (-1.6 ± 0.13) × 10^{-1} μM^{-1} and R^2 = 0.96. Triplicated experiments were performed in 20 mM Tris (pH 7.4), 140 mM NaCl at 20 °C. The error bars correspond to one standard deviation.

6.5 Conclusion

In this section, I aimed to show two independent applications of aptamer-based detection techniques. First, I investigated whether or not levamisole binds the cocaine-binding aptamers. Second, I examined DNA interactions of artemisinin (ART). I chose levamisole because its consumption is harmful to the user of an adulterated cocaine sample, and that levamisole can interfere with electrochemical detection methods. Also, I chose ART because it is an important antimalaria drug, and ART's interaction with DNA molecules had not been investigated prior to this study.

6.5.1 Levamisole studies

NMR studies of the cocaine-binding aptamer by other lab members showed weak binding of levamisole to both MN4 and MN19 resulting from changes in the imino ^{1}H signals in the aptamer. The K_d values obtained from NMR studies, performed by another lab member, were 0.5 mM MN4 and 1.7 mM MN19 at 5 °C in pH 6.8. ITC experiments performed by another lab member, provided no evidence of binding between MN4, MN19 and levamisole. UV thermal melts of MN19-SITS showed no evidence of a sigmoidal denaturation for 0.97 μM MN19-SITS (Figure 6.2). Furthermore, PHASA analysis of cocaine and MN19-SITS in presence of levamisole showed no binding interference from levamisole as these two methods work at a much lower concentration (micromolar range) than in the NMR spectroscopy (millimolar scale).

As many bioassays work in the micromolar concentration range, I do not expect this weak binding of levamisole by the cocaine-binding aptamer to interfere with aptamer-based assays. I demonstrated this non-interference by showing that the photochrome aptamer switch assay using SITS-conjugated to MN19 is not affected by the presence of levamisole.

6.5.2 Artemisinin studies

As for the second objective of this chapter, I showed that the antimalarial compound artemisinin (ART) binds DNA molecules that contain duplex DNA structures. I demonstrated binding with the cocaine-binding aptamer using a combination of UV melt and fluorometry methods. Results presented in this chapter coupled with ITC, NMR and mass spectrometry results obtained by other lab members supported thermal melt and fluorometry analyses [205]. Although the endoperoxide bridge is required for binding, indicating that ART binding might result in a covalently bound

ligand in a similar fashion as ART has been proposed to covalently bind heme, collision-induced dissociation mass spectrometry experiments did not indicate the presence of covalent binding.

Despite ART not being specific for the cocaine binding aptamer, the binding of ART by MN19 still results in ligand induced-folding in this aptamer construct. This occurs as ART binds at the three-way junction and likely pulls together or stabilizes the stems in the molecule. This MN19 folding with ART binding can be exploited by the PHASA assay previously used to quantify cocaine binding and indicates other assays that rely on short stem 1 constructs of the cocaine-binding aptamer folding will likely also detect ART. The implication of ART binding these DNA molecules for the role of ART as an antimalarial agent is yet to be revealed and can be the focus of future work. Whatever role DNA binding by ART may have, depends on numerous factors such as availability and pharmacology of ART in different biological systems.

Chapter 7: Concluding remarks

7.1 Summary

This study aimed to understand the structure dynamics and ligand-binding mechanisms of aptamers utilizing the cocaine-binding aptamer as a model system. Fluorescence spectroscopy was predominantly used as the main technique reported in this dissertation. Other biophysical techniques such as X-ray crystallography, circular dichroism spectroscopy, chromatography, and differential scanning calorimetry were also practiced though unpublished results were not integrated in the present peer-reviewed work.

To sum up, Chapter 1 furnished a comprehensive introduction about the origin and types of aptamers. Available methods of *in vitro* aptamer selection were reviewed and some of the aptamer applications, advantages, and nucleic acid motifs were concisely discussed. Furthermore, fundamentals of fluorescence spectroscopy techniques and the inherent fluorescence property of ligands were discussed. This chapter is particularly beneficial to researchers who practice outside the field of aptamers and fluorometry techniques.

Chapter 2 presented a detection method for aptamer-ligand binding analyses that are based on the intrinsic fluorescence of the ligand. Common extrinsic fluorescence detection techniques with aptamers involve the addition of fluorophores to the aptamer while adding labels can alter the native structure of the aptamer molecule. This chapter comprises of a method protocol demonstrating techniques, obstacles, and optimization steps for aptamer investigations. Although available biophysical techniques such as NMR, ITC, and DSC are accurate methods, these methods are not sensitive in nanomolar and micromolar concentration scales, where fluorometry

techniques perform with high sensitivity and accuracy. Furthermore, NMR and ITC instruments equipped with multi-well readers are currently unavailable. However, fluorometers equipped with multi-well plates can obtain fluorescence emission data from a large number of samples (*e.g.*, 24, 96, or 384 wells) in a matter of seconds-minutes timescale.

Practical applications of the intrinsic fluorometry methods for aptamer-ligand binding analyses were demonstrated in Chapter 3. The utilization of biophysical methods including inherent fluorescence of ligands such as quinine, cocaine, and merocyanine dye (FPhOBtz) was examined and ligand binding and structural dynamics of DNA aptamers were studied. These observations coupled with the identified Stokes shifts in the emission spectrum provided evidence of base stacking intercalations of employed ligands and the cocaine-binding aptamer.

The demonstrated fluorescence spectroscopy method was original in the field of aptamers. A substantial advantage of presented fluorometry protocol is that this method is applicable to other types of fluorescence spectrophotometers such as BioTek Synergy multiplate readers. Therefore, using presented methods can further help optimize the discussed sequences, or new aptamers and binding conditions quickly and quantitatively in a comparable manner to how qPCR (quantitative polymerase chain reaction) is performed [212,213].

Important applications of the first visible light-up probe (FPhOBtz) for the detection of the three-way junction structure in DNA include the identification of cancer biomarkers and investigations of cancer treatments. Studies have shown that some tumor and cancer cells including

HeLa and human breast MCF-7 cancer cells exhibit the three-way junction DNA motif structures [156,157].

The aptamer stem-length modification studies demonstrated in Chapter 4 offered sequence alteration of stems 1 and 2 of the cocaine-binding aptamer. These studies were new in the field of aptamers, where I presented multiple cocaine-binding aptamer variants that have both advantages: thermal stability and ligand-induced binding mechanism. In this chapter, a new method of differential fluorescence thermal shift assay was presented to examine the effect of sequence optimization on the thermal stability and ligand selectivity of the cocaine-binding aptamer.

The presented fluorescence thermal shift assay is original and innovative in the field of aptamers. The importance of this technique in the aptamer stem-length studies is that the propagated signal upon ligand binding detection is a result of aptamer folding. Moreover, the applications of presented ligand-induced binding mechanism have been exploited by other researchers in forensic investigations [214], methamphetamine aptamer tests [215], nanoparticle surface chemistry analyses [216], and electrochemical aptamer-based studies [217,218].

The exploitation of ligand-induced binding mechanism in the cocaine-binding aptamer was further deliberated in Chapter 5. I demonstrated the photoisomerization kinetics measurements of stilbene in the development of the Photochrome Aptamer Switch Assay (PHASA). I also showed the optimized method of aptamer-stilbene conjugation as well as method validation techniques. Furthermore, I investigated two original applications of PHASA method in the detection of

artemisinin, an effective antimalaria drug, and levamisole, a hazardous additive in illicit cocaine samples in Chapter 6.

The benefit of levamisole detection with PHASA method is significant because the consumption of levamisole is unsafe to the user of an adulterated cocaine sample. Also, levamisole can interfere with electrochemical detection methods. The benefit of artemisinin detection with PHASA method is essential since artemisinin is an important antimalaria drug, and the interaction of artemisinin with DNA molecules remained at speculation levels with no evidence of artemisinin-DNA interaction in the scientific community. Artemisinin detection with PHASA method, coupled with other biophysical techniques, proved a pharmacological mechanism of action for artemisinin-DNA interactions that has not been discovered prior to our studies.

7.2 Future Work

In addition to the demonstrated published work in this dissertation, I have conducted several other projects including the study of crystal structure of the chimeric cocaine-binding aptamer using X-ray diffraction methods, structural analyses and optimization of nanostructures such as aptachain and aptamesh [158], thermodynamic analyses of the cocaine-binding aptamer using differential scanning calorimetry [169] and pressure perturbation calorimetry techniques, structural analyses of ochratoxin A aptamer, the ligand displacement competitive binding assay, binding analyses of merocyanine probes with the cocaine-binding aptamer, binding analyses of thrombin protein with salvianolic acid drugs and the structural analyses of human apolipoprotein-A [219].

Some of these collaborative projects are nearing completion and some are in progress. One can utilize the functional knowledge and expertise gained through these research studies and improve discussed projects, namely the structural elucidation of the cocaine-binding aptamer and the structural analyses of human apolipoprotein-A for future projects.

For prospect research opportunities, the intrinsic fluorometry methods that were developed through this study can be applied to other intrinsically fluorescent ligands such as dopamine, serotonin, caffeine, or codeine aptamers [60,77,220]. Dopamine is a catecholamine and has fluorescence properties similar to that of in tyrosine and phenylalanine amino acids. Also, serotonin is a derivative of phenylamine, which has fluorescence properties similar to that of in tryptophan amino acid.

One can exploit these fluorescence properties and optimize previously selected aptamer sequences or characterize aptamer-ligand binding properties using the fluorometry method protocol that was discussed in Chapter 2. In addition, the chemical structures of salvianolic acid drugs contain catecholamine groups that can perform as ligands against the dopamine aptamer. One can use the biophysical methods discussed in this work and further investigate the promiscuous binding mechanism of the dopamine aptamer.

The photochrome aptamer switch assay (PHASA) method that was presented in Chapter 5 and Chapter 6 can be exploited in other aptamer constructs like ochratoxin A aptamer for future studies of ochratoxin A biosensors. The PHASA method is particularly beneficial for aptamer targets that lack fluorescence properties such as ions (*e.g.,* potassium ion aptamer), sugars

(*e.g.*, glucose aptamer), or when analytical conditions are not in favour of the intrinsic fluorescence of the ligand. For instance, in extreme acidic, basic, or high ionic strength conditions (*e.g.,* uric acid aptamer) [77,221,222].

One limitation of presented fluorescence techniques is the sensitivity of the instrument. As discussed in Chapter 1, sensitivity of a fluorometer is determined by its accuracy of fluorescence lifetime (τ) measurement. Available fluorometers can measure τ in milliseconds to microseconds. One can use a highly sensitive instrument that is capable of measuring time-resolved fluorescence in nanoseconds, or shorter, to gain insight about the intrinsic fluorescence quenching or enhancement events upon aptamer-ligand binding mechanisms with further enhanced details.

The effort of new generations of artificial intelligence, bioinformatics, and structural predication algorithms like AlphaFold and DeepRNAFold programs coupled with experimental data is foreseen to impact the field of structural biochemistry [223,224]. These structural prediction programs can be exploited to push our experimental knowledge of aptamer X-ray crystal structure condition optimizations to its frontiers. One can utilize these computational predication tools to study the effect of ligands on the special motif structures of aptamers.

As a final remark, the experimental research study that I demonstrated in this dissertation through utilization of the cocaine-binding aptamer as a model system combined with my collaborative work with other research groups provided valuable insight into the function and structure of the aptamers. It is my hope that this study will further motivate enthusiastic scientists for prospect discovery-driven investigations of structural elucidation of aptamers.

Bibliography

[1] C. Tuerk, L. Gold, Systematic evolution of ligands by exponential enrichment: RNA ligands to bacteriophage T4 DNA polymerase, Science (80-.). 249 (1990) 505–510. https://doi.org/10.1126/science.2200121.

[2] A.D. Ellington, J.W. Szostak, In vitro selection of RNA molecules that bind specific ligands., Nature. 346 (1990) 818–822. https://doi.org/10.1038/346818a0.

[3] E.J. Cho, J.-W. Lee, A.D. Ellington, Applications of Aptamers as Sensors, Annu. Rev. Anal. Chem. 2 (2009) 241–264. https://doi.org/10.1146/annurev.anchem.1.031207.112851.

[4] M. Blind, M. Blank, Aptamer Selection Technology and Recent Advances, Mol. Ther. Acids. 4 (2015) 223. https://doi.org/10.1261/rna.2008110.

[5] D.L. Robertson, G.F. Joyce, Selection in vitro of an RNA enzyme that specifically cleaves single-stranded DNA, Nature. 344 (1990) 467–468. https://doi.org/10.1038/344467a0.

[6] P.B. Moore, Structural motifs in RNA, Annu. Rev. Biochem. 68 (1999) 287–300.

[7] A.D. Ellington, J.W. Szostak, Selection in vitro of single-stranded DNA molecules that fold into specific ligand-binding structures, Nature. 355 (1992) 850–852. https://doi.org/10.1038/355850a0.

[8] P. Colas, B. Cohen, T. Jessen, I. Grishina, J. Mccoyt, R. Brent, Genetic selection of peptide aptamers that recognize and inhibit cyclin-dependent kinase 2, Nature. 380 (1996) 548–550.

[9] F. Hoppe-Seyler, I. Crnkovic-Mertens, C. Denk, B.A. Fitscher, B. Klevenz, E. Tomai, K. Butz, Peptide aptamers: new tools to study protein interactions, Pergamon, 2001. https://doi.org/10.1016/S0960-0760(01)00085-1.

[10] C. Milstein, Monoclonal Antibodies, Sci. Am. 243 (1980) 66–76. http://www.jstor.org/stable/24966435.

[11] P.N. Nelson, G.M. Reynolds, E.E. Waldron, E. Ward, K. Giannopoulos, P.G. Murray, Monoclonal antibodies, Mol. Pathol. 53 (2000) 111–117. https://doi.org/10.1136/mp.53.3.111.

[12] R.H. Kennett, Z.L. Jonak, N. Ikegaki, Monoclonal Antibodies and Molecular Genetics, in: R.H. Kennett, K.B. Bechtol, T.J. McKearn (Eds.), Monoclon. Antibodies, Springer US, Boston, MA, 1984: pp. 311–340. https://doi.org/10.1007/978-1-4684-4673-9_12.

[13] M. Mckeague, V. Calzada, L. Cerchia, M. Derosa, J.M. Heemstra, N. Janjic, P.E. Johnson, L. Kraus, J. Limson, G. Mayer, M. Nilsen-Hamilton, D. Porciani, T.K. Sharma, B. Suess, J.A. Tanner, Sarah Shigdar, The minimum aptamer publication standards (MAPS guidelines) for de novo aptamer selection, Aptamers. 6 (2022) 10–18.

[14] M. McKeague, M.C. Derosa, Challenges and opportunities for small molecule aptamer development, J. Nucleic Acids. 2012 (2012). https://doi.org/10.1155/2012/748913.

[15] D.J. Patel, Structural analysis of nucleic acid aptamers, Curr. Opin. Chem. Biol. 1 (1997) 32–46. https://doi.org/10.1016/s1367-5931(97)80106-8.

[16] X. Sun, S. Hyeon Ko, C. Zhang, A.E. Ribbe, C. Mao, Surface-mediated DNA self-assembly,

J. Am. Chem. Soc. 131 (2009) 13248–13249.

[17] B. Lemieux, A. Aharoni, M. Schena, Overview of DNA chip technology, Mol. Breed. 4 (1998) 277–289.

[18] J.R. Taylor, M.M. Fang, S. Nie, Probing specific sequences on single DNA molecules with bioconjugated fluorescent nanoparticles, Anal. Chem. 72 (2000) 1979–1986.

[19] A. Carré, V. Lacarrière, W. Birch, Molecular interactions between DNA and an aminated glass substrate, J. Colloid Interface Sci. 260 (2003) 49–55.

[20] J.C. Penedo, C.F.W. Becker, J. Ouellet, RNA Fluorescence with Light-Up Aptamers , 2016. https://doi.org/10.3389/fchem.2016.00029.

[21] A.B. Kinghorn, L.A. Fraser, S. Liang, S.C.-C. Shiu, J.A. Tanner, Aptamer bioinformatics, Int. J. Mol. Sci. 18 (2017) 2516.

[22] S. Jeong, S.R. Han, Y.J. Lee, S.-W. Lee, Selection of RNA aptamers specific to active prostate-specific antigen, Biotechnol. Lett. 32 (2010) 379–385.

[23] M. Jing, M.T. Bowser, Isolation of DNA aptamers using micro free flow electrophoresis, Lab Chip. 11 (2011) 3703–3709.

[24] C. Lyu, I.M. Khan, Z. Wang, Capture-SELEX for aptamer selection: A short review, Talanta. 229 (2021) 122274.

[25] K. Sefah, D. Shangguan, X. Xiong, M.B. O'donoghue, W. Tan, Development of DNA aptamers using Cell-SELEX, Nat. Protoc. 5 (2010) 1169–1185.

[26] S. Ohuchi, Cell-SELEX technology, Biores. Open Access. 1 (2012) 265–272.

[27] M. Berezovski, M. Musheev, A. Drabovich, S.N. Krylov, Non-SELEX selection of aptamers, J. Am. Chem. Soc. 128 (2006) 1410–1411.

[28] M. V Berezovski, M.U. Musheev, A.P. Drabovich, J. V Jitkova, S.N. Krylov, Non-SELEX: selection of aptamers without intermediate amplification of candidate oligonucleotides, Nat. Protoc. 1 (2006) 1359–1369.

[29] R. Stoltenburg, C. Reinemann, B. Strehlitz, FluMag-SELEX as an advantageous method for DNA aptamer selection, Anal. Bioanal. Chem. 383 (2005) 83–91.

[30] F.J. Hernandez, S.K. Dondapati, V.C. Ozalp, A. Pinto, C.K. O'Sullivan, T.A. Klar, I. Katakis, Label free optical sensor for Avidin based on single gold nanoparticles functionalized with aptamers, J. Biophotonics. 2 (2009) 227–231.

[31] O. Rabal, F. Pastor, H. Villanueva, M.M. Soldevilla, S. Hervas-Stubbs, J. Oyarzabal, In silico aptamer docking studies: from a retrospective validation to a prospective case study'tim3 aptamers binding, Mol. Ther. Acids. 5 (2016) e376.

[32] J.W. Park, R. Tatavarty, D.W. Kim, H.T. Jung, M.B. Gu, Immobilization-free screening of aptamers assisted by graphene oxide, Chem. Commun. 48 (2012) 2071–2073. https://doi.org/10.1039/c2cc16473f.

[33] V. Okhonin, M. Berezovski, S.N. Krylov, Sweeping capillary electrophoresis: a non-stopped-flow method for measuring bimolecular rate constant of complex formation

between protein and DNA, J. Am. Chem. Soc. 126 (2004) 7166–7167.

[34] S. Klußmann, A. Nolte, R. Bald, V.A. Erdmann, J.P. Fürste, Mirror-image RNA that binds D-adenosine, Nat. Biotechnol. 14 (1996) 1112–1115.

[35] A. Nolte, S. Klußmann, R. Bald, V.A. Erdmann, J.P. Fürste, Mirror-design of L-oligonucleotide ligands binding to L-arginine, Nat. Biotechnol. 14 (1996) 1116–1119.

[36] L. Gold, D. Ayers, J. Bertino, C. Bock, A. Bock, E. Brody, J. Carter, V. Cunningham, A. Dalby, B. Eaton, Aptamer-based multiplexed proteomic technology for biomarker discovery, Nat. Preced. (2010) 1.

[37] H. Youn, K. Lee, J. Her, J. Jeon, J. Mok, J. in So, S. Shin, C. Ban, Aptasensor for multiplex detection of antibiotics based on FRET strategy combined with aptamer/graphene oxide complex, Sci. Rep. 9 (2019) 1–9. https://doi.org/10.1038/s41598-019-44051-3.

[38] J.C. Rohloff, A.D. Gelinas, T.C. Jarvis, U.A. Ochsner, D.J. Schneider, L. Gold, N. Janjic, Nucleic acid ligands with protein-like side chains: modified aptamers and their use as diagnostic and therapeutic agents, Mol. Ther. Acids. 3 (2014) e201.

[39] C. Eid, J.W. Palko, E. Katilius, J.G. Santiago, Rapid slow off-rate modified aptamer (SOMAmer)-based detection of C-reactive protein using isotachophoresis and an ionic spacer, Anal. Chem. 87 (2015) 6736–6743.

[40] D.E. Volk, G.L.R. Lokesh, Development of phosphorothioate DNA and DNA thioaptamers, Biomedicines. 5 (2017) 41.

[41] G.L. Lokesh, H. Wang, C.H. Lam, V. Thiviyanathan, N. Ward, D.G. Gorenstein, D.E. Volk, X-aptamer selection and validation, in: RNA Nanostructures, Springer, 2017: pp. 151–174.

[42] T. Hermann, D.J. Patel, Adaptive Recognition by Nucleic Acid Aptamers, Science (80-.). 287 (2000) 820–825. https://doi.org/10.1126/science.287.5454.820.

[43] J.A. Cruz-Aguado, G. Penner, J. A. Cruz-Aguado, G. Penner, Determination of Ochratoxin A with a DNA Aptamer, J. Agric.Food Chem. 56 (2008) 10456–10461. https://doi.org/10.1021/jf801957h.

[44] G.J. Wedemayer, P.A. Patten, L.H. Wang, P.G. Schultz, R.C. Stevens, Structural insights into the evolution of an antibody combining site, Science (80-.). 276 (1997) 1665–1669.

[45] C.A.K. Borrebaeck, M. Ohlin, Antibody evolution beyond Nature, Nat. Biotechnol. 20 (2002) 1189–1190.

[46] G. Zhu, X. Chen, Aptamer-based targeted therapy, Adv. Drug Deliv. Rev. 134 (2018) 65–78.

[47] M.M. Soldevilla, H. Villanueva, F. Pastor, Aptamers: a feasible technology in cancer immunotherapy, J. Immunol. Res. 2016 (2016).

[48] D.W. Smith, H.E. Schaller, F.J. Bonhoeffer, DNA synthesis in vitro, Nature. 226 (1970) 711–713.

[49] B. Dejaegher, Y. Vander Heyden, Ruggedness and robustness testing, J. Chromatogr. A. 1158 (2007) 138–157. https://doi.org/10.1016/J.CHROMA.2007.02.086.

[50] B.A. Teicher, R.V.J. Chari, Antibody conjugate therapeutics: challenges and potential, Clin. Cancer Res. 17 (2011) 6389–6397.

[51] N. Li, Y. Wang, A. Pothukuchy, A. Syrett, N. Husain, S. Gopalakrisha, P. Kosaraju, A.D. Ellington, Aptamers that recognize drug-resistant HIV-1 reverse transcriptase, Nucleic Acids Res. 36 (2008) 6739–6751.

[52] A. Chandran, D. Ghoshdastidar, S. Senapati, Groove binding mechanism of ionic liquids: a key factor in long-term stability of DNA in hydrated ionic liquids?, J. Am. Chem. Soc. 134 (2012) 20330–20339.

[53] W.D. Wilson, R.L. Jones, Intercalating drugs: DNA binding and molecular pharmacology, Adv. Pharmacol. 18 (1981) 177–222.

[54] O. Kensch, B.A. Connolly, H.-J. Steinhoff, A. McGregor, R.S. Goody, T. Restle, HIV-1 reverse transcriptase-pseudoknot RNA aptamer interaction has a binding affinity in the low picomolar range coupled with high specificity, J. Biol. Chem. 275 (2000) 18271–18278.

[55] R.F. Macaya, P. Schultze, F.W. Smith, J.A. Roe, J. Feigon, Thrombin-binding DNA aptamer forms a unimolecular quadruplex structure in solution, Proc. Natl. Acad. Sci. U. S. A. 90 (1993) 3745–3749. https://doi.org/10.1073/PNAS.90.8.3745.

[56] D.E.E. Huizenga, J.W.W. Szostak, A DNA aptamer that binds adenosine and ATP., Biochemistry. 34 (1995) 656–665. https://doi.org/10.1021/bi00002a033.

[57] I. Jeddi, L. Saiz, Three-dimensional modeling of single stranded DNA hairpins for aptamer-based biosensors, Sci. Rep. 7 (2017) 1–13. https://doi.org/10.1038/s41598-017-01348-5.

[58] M.A.D. Neves, O. Reinstein, M. Saad, P.E. Johnson, Defining the secondary structural requirements of a cocaine-binding aptamer by a thermodynamic and mutation study, Biophys. Chem. 153 (2010) 9–16. https://doi.org/10.1016/j.bpc.2010.09.009.

[59] T. Kato, T. Takemura, K. Yano, K. Ikebukuro, I. Karube, In vitro selection of DNA aptamers which bind to cholic acid, Biochim. Biophys. Acta - Gene Struct. Expr. 1493 (2000) 12–18. https://doi.org/10.1016/S0167-4781(00)00080-4.

[60] T. Bing, W. Zheng, X. Zhang, L. Shen, X. Liu, F. Wang, J. Cui, Z. Cao, D. Shangguan, Triplex-quadruplex structural scaffold: a new binding structure of aptamer OPEN, Sci. Rep. 7 (2017) 1–10. https://doi.org/10.1038/s41598-017-15797-5.

[61] M.N. Stojanovic, P. De Prada, D.W. Landry, Fluorescent sensors based on aptamer self-assembly, J. Am. Chem. Soc. 122 (2000) 11547–11548. https://doi.org/10.1021/ja0022223.

[62] M.N. Stojanovic, P. De Prada, D.W. Landry, Aptamer-Based Folding Fluorescent Sensor for Cocaine, J. Am. Chem. Soc. 123 (2001) 4928–4931. https://doi.org/10.1021/ja0038171.

[63] M.N. Stojanovic, D.W. Landry, Aptamer-based colorimetric probe for cocaine, J. Am. Chem. Soc. 124 (2002) 9678–9679. https://doi.org/10.1021/ja0259483.

[64] M.A.D. Neves, O. Reinstein, P.E. Johnson, Defining a stem length-dependent binding mechanism for the cocaine-binding aptamer. A combined NMR and calorimetry study, Biochemistry. 49 (2010) 8478–8487. https://doi.org/10.1021/bi100952k.

[65] M.A.D. Neves, C. Blaszykowski, S. Bokhari, M. Thompson, Ultra-high frequency

piezoelectric aptasensor for the label-free detection of cocaine, Biosens. Bioelectron. 72 (2015) 383–392. https://doi.org/10.1016/j.bios.2015.05.038.

[66] O. Reinstein, M.A.D. Neves, M. Saad, S.N. Boodram, S. Lombardo, S.A. Beckham, J. Brouwer, G.F. Audette, P. Groves, M.C.J. Wilce, P.E. Johnson, Engineering a structure switching mechanism into a steroid-binding aptamer and hydrodynamic analysis of the ligand binding mechanism, Biochemistry. 50 (2011) 9368–9376. https://doi.org/10.1021/bi201361v.

[67] O. Reinstein, M. Yoo, C. Han, T. Palmo, S.A. Beckham, M.C.J.J. Wilce, J. P.E., P.E. Johnson, S. A. Beckham, M. C. J. Wilce, P. E. Johnson, S.A. Beckham, M.C.J.J. Wilce, P.E. Johnson, Quinine binding by the cocaine-binding aptamer. thermodynamic and hydrodynamic analysis of high-affinity binding of an off-target ligand, Biochemistry. 52 (2013) 8652–8662. https://doi.org/10.1021/bi4010039.

[68] S. Slavkovic, M. Altunisik, O. Reinstein, P.E. Johnson, Structure-affinity relationship of the cocaine-binding aptamer with quinine derivatives, Bioorganic Med. Chem. Med. Chem. 23 (2015) 2593–2597. https://doi.org/10.1016/j.bmc.2015.02.052.

[69] S. Slavkovic, Z.R. Churcher, P.E. Johnson, Nanomolar binding affinity of quinine-based antimalarial compounds by the cocaine-binding aptamer, Bioorganic Med. Chem. 26 (2018) 5427–5434. https://doi.org/10.1016/j.bmc.2018.09.017.

[70] Z.R. Churcher, D. Garaev, H.N. Hunter, P.E. Johnson, Reduction in Dynamics of Base pair Opening upon Ligand Binding by the Cocaine-Binding Aptamer, Biophys. J. 119 (2020) 1147–1156. https://doi.org/10.1016/j.bpj.2020.08.012.

[71] F. Bănică, Affinity-Based Recognition, Chem. Sensors Biosens. (2012) 101–117. https://doi.org/10.1002/9781118354162.ch6.

[72] S. Slavkovic, S.R. Eisen, P.E. Johnson, Designed Alteration of Binding Affinity in Structure-Switching Aptamers through the Use of Dangling Nucleotides, Biochemistry. 59 (2020) 663–670. https://doi.org/10.1021/acs.biochem.9b00630.

[73] N.B. Leontis, W. Kwok, J.S. Newman, Stability and structure of three-way DNA junctions containing unpaired nucleotides, Nucleic Acids Res. 19 (1991) 759–766. https://doi.org/10.1093/nar/19.4.759.

[74] C. Wu, L. Yan, C. Wang, H. Lin, C. Wang, X. Chen, C.J. Yang, A general excimer signaling approach for aptamer sensors, Biosens. Bioelectron. 25 (2010) 2232–2237. https://doi.org/10.1016/j.bios.2010.02.030.

[75] C. Altona, D.H. Faber, A.J.A.W. Hoekzema, Double-helical DNA1H chemical shifts: an accurate and balanced predictive empirical scheme, Magn. Reson. Chem. 38 (2000) 95–107.

[76] N. Nakatsuka, A. Faillétaz, D. Eggemann, C. Forró, J. Vörös, D. Momotenko, Aptamer Conformational Change Enables Serotonin Biosensing with Nanopipettes, Anal. Chem. 93 (2021) 4033–4041. https://doi.org/10.1021/acs.analchem.0c05038.

[77] N. Nakatsuka, K.A. Yang, J.M. Abendroth, K.M. Cheung, X. Xu, H. Yang, C. Zhao, B. Zhu, Y.S. Rim, Y. Yang, P.S. Weiss, M.N. Stojanović, A.M. Andrews, N. Nako, Y. Kyung-

Ae, A.J.A.A. M., C.K. M., X. Xiaobin, Y. Hongyan, Z. Chuanzhen, Z. Bowen, R.Y. Seung, Y. Yang, W.P. S., S.M. N., A.J.A.A. M., Aptamer-field-effect transistors overcome Debye length limitations for small-molecule sensing, Science (80-.). 362 (2018) 319–324. https://doi.org/10.1126/science.aao675.

[78] C. Baugh, D. Grate, C. Wilson, 2.8 Å Crystal structure of the malachite green aptamer, J. Mol. Biol. 301 (2000) 117–128. https://doi.org/10.1006/jmbi.2000.3951.

[79] T. Wang, J. A. Hoy, M. H. Lamm, M. Nilsen-Hamilton, J.A. Hoy, M.H. Lamm, M. Nilsen-Hamilton, W. Tianjiao, J.A. Hoy, M.H. Lamm, M. Nilsen-Hamilton, Computational and Experimental Analyses Converge to Reveal a Coherent Yet Malleable Aptamer Structure That Controls Chemical Reactivity, J. Am. Chem. Soc. 131 (2009) 14747–14755. https://doi.org/10.1021/ja902719q.

[80] A.U. Acuña, F. Amat-Guerri, Early History of Solution Fluorescence: The Lignum nephriticum of Nicolás Monardes, in: M.N. Berberan-Santos (Ed.), Fluoresc. Supermolecules, Polym. Nanosyst., Springer Berlin Heidelberg, Berlin, Heidelberg, 2008: pp. 3–20. https://doi.org/10.1007/4243_2007_006.

[81] E.N. Harvey, A History of Luminescence from the Earliest Times Until 1900, American Philosophical Society, 1957. https://doi.org/10.2307/1848952.

[82] A. Ulises Acuña, F. Amat-Guerri, P. Morcillo, M. Liras, B. Rodríguez, A.U. Acuña, F. Amat-Guerri, P. Morcillo, M. Liras, B. Rodríguez, Structure and formation of the fluorescent compound of lignum nephriticum, Org. Lett. 11 (2009) 3020–3023. https://doi.org/10.1021/ol901022g.

[83] R. Boyle, C. Merret, New experiments and observations touching cold, Royal Society of London, London, UK, 1665.

[84] D.A. Tomalia, B. Klajnert-Maculewicz, K.A.-M. Johnson, H.F. Brinkman, A. Janaszewska, D.M. Hedstrand, Non-traditional intrinsic luminescence: inexplicable blue fluorescence observed for dendrimers, macromolecules and small molecular structures lacking traditional/conventional luminophores, Prog. Polym. Sci. 90 (2019) 35–117. https://doi.org/10.1016/j.progpolymsci.2018.09.004.

[85] D.R. Dreyer, D.J. Miller, B.D. Freeman, D.R. Paul, C.W. Bielawski, D. R. Dreyer, D. J. Miller, B. D. Freeman, D. R. Paul, C. W. Bielawski, Elucidating the Structure of Poly(dopamine), Langmuir. 28 (2012) 6428−6435. https://doi.org/10.1021/la204831b.

[86] J.F.W. Herschel, On a case of superficial colour presented by a homogeneous liquid internally colourless, Philos. Trans. R. Soc. London. 135 (1845) 143–145. https://doi.org/10.1098/rstl.1845.0004.

[87] G.G. Stokes, On the Change of Refrangibility of Light, Philos. Trans. R. Soc. London. 142 (1852) 463–562. https://doi.org/10.1017/cbo9780511702266.012.

[88] J.R. Lakowicz, Principles of Fluorescence Spectroscopy, 3rd ed., Springer, Baltimore, USA, 2006. https://doi.org/10.1007/978-0-387-46312-4.

[89] R. LeSar, Statistical thermodynamics and kinetics, 3rd ed., Pearson, Boston, USA, 2013. https://doi.org/10.1017/cbo9781139033398.022.

[90] N. Boens, W. Qin, N. Basarić, J. Hofkens, M. Ameloot, J. Pouget, J.P. Lefèvre, B. Valeur, E. Gratton, M. VandeVen, N.D. Silva, Y. Engelborghs, K. Willaert, A. Sillen, G. Rumbles, D. Phillips, A.J.W.G. Visser, A. Van Hoek, J.R. Lakowicz, H. Malak, I. Gryczynski, A.G. Szabo, D.T. Krajcarski, N. Tamai, A. Miura, Fluorescence lifetime standards for time and frequency domain fluorescence spectroscopy, Anal. Chem. 79 (2007) 2137–2149. https://doi.org/10.1021/ac062160k.

[91] J.B. Birks, Fluorescence quantum yield measurements, J. Res. Natl. Bur. Stand. Sect. A Phys. Chem. 80A (1976) 389. https://doi.org/10.6028/jres.080a.038.

[92] C.A. Royer, Fluorescence spectroscopy, in: N.J. Clifton (Ed.), Methods Mol. Biol., Wiley-VCH, 1995: pp. 65–89. https://doi.org/10.1385/0-89603-301-5:65.

[93] Skoog, W. D. A., H. D. M., & C. F. J., Fundamentals of Chemistry Analytical, 9th ed., Brooks/Cole, Belmount, USA, 2015. Skoog, D. A., West, D. M., Holler, F. J., & Crouch, S. R. (2015). Fundamentals of Chemistry Analytical (Vol. 3, pp. 1–1088).

[94] V.E. Centonze, A. Takahashi, E. Casanova, B. Herman, Quantitative fluorescence microscopy, J. Histotechnol. 23 (2000) 229–234. https://doi.org/10.1179/his.2000.23.3.229.

[95] M. Sauer, J. Hofkens, J. Enderlein, Handbook of Fluorescence Spectroscopy and Imaging: From Single Molecules to Ensembles, Wiley-VCH, Weinheim, Germany, 2011. https://doi.org/10.1002/9783527633500.

[96] S. Hirka, M. Mckeague, Quantification of aptamer-protein binding with fluorescence anisotropy – Aptamers, Aptamers. 5 (2021) 1–6.

[97] J.C. Pessoa, I. Correia, G. Gonçalves, I. Tomaz, Circular dichroism in coordination compounds, J. Argentine Chem. Soc. 97 (2009) 151–165.

[98] M. Vorlíčková, I. Kejnovská, K. Bednářová, D. Renčiuk, J. Kypr, Circular Dichroism Spectroscopy of DNA: From Duplexes to Quadruplexes, Chirality. 24 (2012) 691–698. https://doi.org/https://doi.org/10.1002/chir.22064.

[99] K.C. Hasson, F. Gai, P.A. Anfinrud, The photoisomerization of retinal in bacteriorhodopsin: Experimental evidence for a three-state model, Proc. Natl. Acad. Sci. U. S. A. 93 (1996) 15124–15129. https://doi.org/10.1073/pnas.93.26.15124.

[100] H. Görner, H.J. Kuhn, Cis-Trans Photoisomerization of stilbene-like molecules, in: D.C. Neckers, D.H. Volman, G. von Bünau (Eds.), Adv. Photochem., Wiley, 2007: pp. 1–117. https://doi.org/10.1002/9780470133453.

[101] A. Faelli, M. Tosco, M.N. Orsenigo, G. Esposito, Effects of the stilbene derivatives SITS and DIDS on intestinal ATPase activities, Pharmacol. Res. Commun. 16 (1984) 339–350. https://doi.org/10.1016/S0031-6989(84)80002-8.

[102] V. Papper, O. Pokholenko, Y. Wu, Y. Zhou, P. Jianfeng, T.W.J. Steele, R.S. Marks, Novel photochrome aptamer switch assay (PHASA) for adaptive binding to aptamers, J. Fluoresc. 24 (2014) 1581–1591. https://doi.org/10.1007/s10895-014-1441-9.

[103] Y. Zhou, Y. Wu, O. Pokholenko, V. Papper, R.S. Marks, T.W.J. Steele, Design and optimisation of Photochrome Aptamer Switch Assay (PHASA), Anal. Chim. Acta. 1061

(2019) 134–141. https://doi.org/10.1016/j.aca.2019.01.049.

[104] A.A. Shoara, S. Slavkovic, L.W. Donaldson, P.E. Johnson, Analysis of the interaction between the cocaine-binding aptamer and its ligands using fluorescence spectroscopy, Can. J. Chem. 95 (2017) 1253–1260. https://doi.org/10.1139/cjc-2017-0380.

[105] M. Baranska, H. Schulz, Determination of Alkaloids through Infrared and Raman Spectroscopy, in: Alkaloids Chem. Biol., 2009: pp. 217–255. https://doi.org/10.1016/S1099-4831(09)06704-2.

[106] H.L. Holmes, The Chemistry of the Tropane Alkaloids, in: Alkaloids Chem. Physiol., Academic Press, 1950: pp. 271–374. https://doi.org/10.1016/S1876-0813(08)60189-X.

[107] G. Barger, H.H. Dale, Chemical structure and sympathomimetic action of amines, J. Physiol. 41 (1910) 19.

[108] UNODC, World Drug Report, United Nations Office on Drugs and Crime, Vienna, Austria, 2012. https://www.unodc.org/unodc/en/data-and-analysis/WDR-2012.html.

[109] S.B. Karch, F.P. Busardò, F. Vaiano, F. Portelli, S. Zaami, E. Bertol, Levamisole adulterated cocaine and pulmonary vasculitis: presentation of two lethal cases and brief literature review, Forensic Sci. Int. 265 (2016) 96–102.

[110] S.B. Karch, F. Mari, V. Bartolini, E. Bertol, Aminorex poisoning in cocaine abusers, Int. J. Cardiol. 158 (2012) 344–346.

[111] M.J. Fernández-Serrano, J.C. Perales, L. Moreno-López, M. Pérez-García, A. Verdejo-García, Neuropsychological profiling of impulsivity and compulsivity in cocaine dependent individuals, Psychopharmacology (Berl). 219 (2012) 673–683.

[112] N. Albein-Urios, J.M. Martinez-González, Ó. Lozano, L. Clark, A. Verdejo-García, Comparison of impulsivity and working memory in cocaine addiction and pathological gambling: Implications for cocaine-induced neurotoxicity, Drug Alcohol Depend. 126 (2012) 1–6.

[113] J.J. Baeza-Baeza, M.C. García-Alvarez-Coque, Prediction of peak shape as a function of retention in reversed-phase liquid chromatography, J. Chromatogr. A. 1022 (2004) 17–24. https://doi.org/10.1016/j.chroma.2003.09.059.

[114] A. Chakraborty, S. Ghosh, P. Mukhopadhyay, S.M. Dinara, A. Bag, M.K. Mahata, R. Kumar, S. Das, J. Sanjay, S. Majumdar, D. Biswas, Trapping effect analysis of AlGaN/InGaN/GaN Heterostructure by conductance frequency measurement, in: MRS Proc., Royal Society of Chemistry, Cambridge, UK, 2014: pp. 81–87.

[115] A.W. Sangster, K.L. Stuart, Ultraviolet Spectra of Alkaloids, Chem. Rev. 65 (1965) 69–130. https://doi.org/10.1021/cr60233a003.

[116] I. Vayá, T. Gustavsson, F.A. Miannay, T. Douki, D. Markovitsi, Fluorescence of natural DNA: From the femtosecond to the nanosecond time scales, J. Am. Chem. Soc. 132 (2010) 11834–11835. https://doi.org/10.1021/ja102800r.

[117] A.A. Shoara, Philip E. Johnson, Fluorometry Studies of Aptamers That Bind Intrinsically Fluorescent Ligands: Techniques, Obstacles, and Optimizations, Aptamers (Submitted).

(2022).

[118] C. Berens, A. Thain, R. Schroeder, A tetracycline-binding RNA aptamer, Bioorg. Med. Chem. 9 (2001) 2549–2556.

[119] R.J. Nedumpara, K.J. Thomas, V.K. Jayasree, C.P. Girijavallabhan, V.P.N. Nampoori, P. Radhakrishnan, Study of solvent effect in laser emission from Coumarin 540 dye solution, Appl. Opt. 46 (2007) 4786–4792. https://doi.org/10.1364/AO.46.004786.

[120] J.J. Pedrotti, S. Lima, N. Coichev, I.G.R. Gutz, Overcoming oxygen quenching in fluorescence spectrometry with a highly efficient in-line degassing device interfaced with a flow cell, Anal. Chim. Acta. 422 (2000) 131–137. https://doi.org/10.1016/S0003-2670(00)01060-6.

[121] J.N. Miller, J.C. Miller, The quality of analytical measurements, in: Stat. Chemom. Anal. Chem., 6th ed., Pearson, Harlow, UK, 2010: pp. 74–151. https://doi.org/10.1198/tech.2004.s248.

[122] G.L. Long, J.D. Winefordner, Limit of Detection: A Closer Look at the IUPAC Definition, Anal. Chem. 55 (1983) 712A-724A. https://doi.org/10.1021/ac00258a001.

[123] T.N. Rao, Validation of Analytical Methods, in: M.T. Stauffer (Ed.), Calibration Valid. Anal. Methods, IntechOpen, London, UK, 2018: pp. 131–141. https://doi.org/10.1021/ac00257a001.

[124] S.O. Flyckt, C. Marmonier, Photomultiplier tubes–principles & applications, Photonis, 2002, URL Http//Www2. Pv. Infn. It/Debari/Doc/Flyckt Marmonier. Pdf. (2002).

[125] Y. Guan, Photomultiplier tubes in biosensors., 2009. https://doi.org/10.1007/978-1-60327-567-5_21.

[126] C. Burgess, T. Frost, Standards and best practice in absorption spectrometry, Blackwell Science, 1999.

[127] J.M. Harnly, Optimization of Slit Parameters for Continuum Source Atomic Absorption Spectrometry, Anal. Chem. 54 (1982) 1043–1048. https://doi.org/10.1021/ac00244a007.

[128] C. Burgess, Practical absorption spectrometry, in: A. Knowles (Ed.), Tech. VISIBLE Ultrav. Spectrom., Wiley, London, UK, 1984: p. 151. https://doi.org/10.1016/0160-9327(84)90018-8.

[129] K. Rurack, Fluorescence Quantum Yields: Methods of Determination and Standards, 2008. https://doi.org/10.1007/4243_2008_019.

[130] A.T. Rhys Williams, S.A. Winfield, J.N. Miller, Relative fluorescence quantum yields using a Computer-controlled luminescence spectrometer, Analyst. 108 (1983) 1067–1071. https://doi.org/10.1039/an9830801067.

[131] H. Du, R.-C.A. Fuh, J. Li, L.A. Corkan, J.S. Lindsey, PhotochemCAD: A Computer-Aided Design and Research Tool in Photochemistry, Photochem. Photobiol. 68 (1998) 141–142. https://doi.org/https://doi.org/10.1111/j.1751-1097.1998.tb02480.x.

[132] Origin, OriginPro 2016, OriginLab. (2016).

[133] D.W. Newton, R.B. Kluza, pKa values of medicinal compounds in pharmacy practice, Drug Intell. Clin. Pharm. 12 (1978) 546–554. https://doi.org/10.1177/106002807801200906.

[134] S. Slavkovic, P.E. Johnson, Isothermal titration calorimetry studies of aptamer-small molecule interactions: practicalities and pitfalls, Aptamers. 2 (2018) 45–51.

[135] J.M. Price, M. Kaihara, H.K. Howerton, Influence of Scattering on Fluorescence Spectra of Dilute Solutions Obtained with the Aminco–Bowman Spectrophotofluorometer, Appl. Opt. 1 (1962) 521. https://doi.org/10.1364/ao.1.000521.

[136] Y. Li, F. Qian, Z. Li, Reduction of second-order scattering interference by variable-angle synchronous luminescence spectroscopy, Chem. J. Internet. 2 (2000) 29–36.

[137] L.A. Freiburger, K. Auclair, A.K. Mittermaier, M.A.K. Freiburger L.A., Auclair K., L.A. Freiburger, K. Auclair, A.K. Mittermaier, Elucidating Protein Binding Mechanisms by Variable-c ITC, ChemBioChem. 10 (2009) 2871–2873. https://doi.org/10.1002/cbic.200900614.

[138] I. Herrera, M.A. Winnik, Differential binding models for isothermal titration calorimetry: Moving beyond the Wiseman isotherm, J. Phys. Chem. B. 117 (2013) 8659–8672. https://doi.org/10.1021/jp311812a.

[139] E. Freire, A. Schön, A. Velazquez-Campoy, Isothermal titration calorimetry: general formalizm using binding polynomials, Methods Enzym. 455 (2009) 127–155. https://doi.org/10.1016/S0076-6879(08)04205-5.

[140] A.J. Van Riesen, J. Le, S. Slavkovic, Z.R. Churcher, A.A. Shoara, P.E. Johnson, R.A. Manderville, Visible Fluorescent Light-up Probe for DNA Three-Way Junctions Provides Host–Guest Biosensing Applications, ACS Appl. Bio Mater. 4 (2021) 6732–6741. https://doi.org/10.1021/acsabm.1c00431.

[141] R. Freeman, E. Sharon, T.V. Ran, I. Willner, Supramolecular cocaine-aptamer complexes activate biocatalytic cascades, J. Am. Chem. Soc. 131 (2009) 5028–5029. https://doi.org/10.1021/ja809496n.

[142] Y. Xiang, Y. Lu, Using personal glucose meters and functional DNA sensors to quantify a variety of analytical targets, Nat. Chem. 3 (2011) 697–703. https://doi.org/10.1038/nchem.1092.

[143] R. Kawano, T. Osaki, H. Sasaki, M. Takinoue, S. Yoshizawa, S. Takeuchi, Rapid detection of a cocaine-binding aptamer using biological nanopores on a chip, J. Am. Chem. Soc. 133 (2011) 8474–8477. https://doi.org/10.1021/ja2026085.

[144] K. Kang, A. Sachan, M. Nilsen-Hamilton, P. Shrotriya, Aptamer functionalized microcantilever sensors for cocaine detection, Langmuir. 27 (2011) 14696–14702. https://doi.org/10.1021/la202067y.

[145] A.K. Sharma, J.M. Heemstra, Small-molecule-dependent split aptamer ligation, J. Am. Chem. Soc. 133 (2011) 12426–12429. https://doi.org/10.1021/ja205518e.

[146] J. Das, K.B. Cederquist, A.A. Zaragoza, P.E. Lee, E.H. Sargent, S.O. Kelley, An ultrasensitive universal detector based on neutralizer displacement, Nat. Chem. 4 (2012)

642–648. https://doi.org/10.1038/nchem.1367.

[147] B. Malile, J.I.L. Chen, Morphology-based plasmonic nanoparticle sensors: Controlling etching kinetics with target-responsive permeability gate, J. Am. Chem. Soc. 135 (2013) 16042–16045. https://doi.org/10.1021/ja4086269.

[148] D. Roncancio, H. Yu, X. Xu, S. Wu, R. Liu, J. Debord, X. Lou, Y. Xiao, A label-free aptamer-fluorophore assembly for rapid and specific detection of cocaine in biofluids., Anal. Chem. 86 (2014) 11100–11106. https://doi.org/10.1021/ac503360n.

[149] M.N. Stojanovic, Allosteric regulation of small-molecule binding to aptamers, J.Serb.Chem. Soc. 69 (2004) 871–875.

[150] B.R. Baker, R.Y. Lai, M.S. Wood, E.H. Doctor, A.J. Heeger, K.W. Plaxco, B. R. Baker, R. Y. Lai, M. S. Wood, E. H. Doctor, A. J. Heeger, K. W. Plaxco, An electronic, aptamer-based small-molecule sensor for the rapid, label-free detection of cocaine in adulterated samples and biological fluids, J. Am. Chem. Soc. 128 (2006) 3138–3139. https://doi.org/10.1021/ja056957p.

[151] J. Liu, Y. Lu, Fast colorimetric sensing of adenosine and cocaine based on a general sensor design involving aptamers and nanoparticles, Angew. Chemie - Int. Ed. 45 (2005) 90–94. https://doi.org/10.1002/anie.200502589.

[152] B. Shlyahovsky, D. Li, Y. Weizmann, R. Nowarski, M. Kotler, I. Willner, Spotlighting of cocaine by an autonomous aptamer-based machine, J. Am. Chem. Soc. 129 (2007) 3814–3815. https://doi.org/10.1021/ja069291n.

[153] J. Chen, J. Jiang, X. Gao, G. Liu, G. Shen, R. Yu, A new aptameric biosensor for cocaine based on surface-enhanced raman scattering spectroscopy, Chem. - A Eur. J. 14 (2008) 8374–8382. https://doi.org/10.1002/chem.200701307.

[154] Y. Du, S. Dong, Nucleic acid biosensors: Recent advances and perspectives, Anal. Chem. 89 (2017) 189–215. https://doi.org/10.1021/acs.analchem.6b04190.

[155] S.P. Jagtap, S. Mukhopadhyay, V. Coropceanu, G.L. Brizius, J.L. Brédas, D.M. Collard, Closely stacked oligo(phenylene ethynylene)s: Effect of π-stacking on the electronic properties of conjugated chromophores, J. Am. Chem. Soc. 134 (2012) 7176–7185. https://doi.org/10.1021/ja3019065.

[156] K.C. Woods, S.S. Martin, V.C. Chu, E.P. Baldwin, Quasi-equivalence in site-specific recombinase structure and function: crystal structure and activity of trimeric cre recombinase bound to a three-way lox DNA junction, J. Mol. Biol. 313 (2001) 49–69. https://doi.org/https://doi.org/10.1006/jmbi.2001.5012.

[157] K. Duskova, J. Lamarche, S. Amor, C. Caron, N. Queyriaux, M. Gaschard, M.-J. Penouilh, G. de Robillard, D. Delmas, C. H. Devillers, A. Granzhan, M.-P. Teulade-Fichou, M. Chavarot-Kerlidou, B. Therrien, S. Britton, D. Monchaud, Identification of Three-Way DNA Junction Ligands through Screening of Chemical Libraries and Validation by Complementary in Vitro Assays, J. Med. Chem. 62 (2019) 4456–4466. https://doi.org/10.1021/acs.jmedchem.8b01978.

[158] M.A.D. Neves, S. Slavkovic, O. Reinstein, A.A. Shoara, P.E. Johnson, A proof of concept

application of aptachain: ligand-induced self-assembly of a DNA aptamer, RSC Adv. 9 (2019) 1690–1695. https://doi.org/10.1039/C8RA07462C.

[159] Y. Dong, C. Yao, Y. Zhu, L. Yang, D. Luo, D. Yang, DNA functional materials assembled from branched DNA: Design, synthesis, and applications, Chem. Rev. 120 (2020) 9420–9481. https://doi.org/10.1021/acs.chemrev.0c00294.

[160] A.J. Van Riesen, R.E. Johnson, M. Sameer Al-Abdul-Wahid, C. Liota, A. Christyanton, R.A. Manderville, Temperature Sensing of Thiolate Addition by Phenolate Merocyanine Dyes: Importance of the Quinone Methide Resonance Structure, J. Org. Chem. 86 (2021) 1583–1590. https://doi.org/10.1021/acs.joc.0c02428.

[161] R. E. Johnson, A. J. Van Riesen, R. A. Manderville, On-Strand Knoevenagel Insertion of a Hemicyanine Molecular Rotor Loop Residue for Turn-On Fluorescence Detection of Pb-Induced G-Quadruplex Rigidity, Bioconjug. Chem. 32 (2021) 2224–2232. https://doi.org/10.1021/acs.bioconjchem.1c00386.

[162] H. Wang, Y. Chen, W. Tan, Aptamer Selection, Phage Display, and Sensor Development, in: Chemosens. Princ. Strateg. Appl., 2011: pp. 191–209. https://doi.org/https://doi.org/10.1002/9781118019580.ch10.

[163] M. Van De Weert, Fluorescence quenching to study protein-ligand binding: Common errors, J. Fluoresc. 20 (2010) 625–629. https://doi.org/10.1007/s10895-009-0572-x.

[164] M.R. Eftink, C.A. Ghiron, Fluorescence quenching studies with proteins, Anal. Biochem. 114 (1981) 199–227. https://doi.org/10.1016/0003-2697(81)90474-7.

[165] W.R. Laws, P.B. Contino, Fluorescence quenching studies: Analysis of nonlinear Stern-Volmer data, Methods Enzymol. 210 (1992) 448–463. https://doi.org/10.1016/0076-6879(92)10023-7.

[166] H.J. Böhm, G. Schneider, Protein-Ligand Interactions: From Molecular Recognition to Drug Design, 2nd ed., Springer-Humana, Hatfield, UK, 2005. https://doi.org/10.1002/3527601813.

[167] C. Würth, M. Grabolle, J. Pauli, M. Spieles, U. Resch-Genger, Relative and absolute determination of fluorescence quantum yields of transparent samples, Nat. Protoc. 8 (2013) 1535–1550. https://doi.org/10.1038/nprot.2013.087.

[168] G. Bozokalfa, H. Akbulut, B. Demir, E. Guler, Z.P.P. Gumus, D. Odaci Demirkol, E. Aldemir, S. Yamada, T. Endo, H. Coskunol, S. Timur, Y. Yagci, Polypeptide Functional Surface for the Aptamer Immobilization: Electrochemical Cocaine Biosensing, Anal. Chem. 88 (2016) 4161–4167. https://doi.org/10.1021/acs.analchem.6b00760.

[169] R.W. Harkness, S. Slavkovic, P.E. Johnson, A.K. Mittermaier, Rapid characterization of folding and binding interactions with thermolabile ligands by DSC, Chem. Commun. 52 (2016) 48–91. https://doi.org/10.1039/c6cc05576a.

[170] M.R. Eftink, C.A. Ghiron, Dynamics of a protein matrix revealed by fluorescence quenching., Proc. Natl. Acad. Sci. 72 (1975) 3290–3294. https://doi.org/10.1073/pnas.72.9.3290.

[171] O. Stern, M. Volmer, The extinction period of fluorescence., Phys. Zeitschrift. 20 (1919) 183–188.

[172] E. Blatt, R.C. Chatelier, W.H. Sawyer, Effects of Quenching Mechanism and Type of Quencher Association on Stern-Volmer Plots in Compartmentalized Systems, Biophys. J. 50 (1986) 349–356. https://doi.org/10.1016/S0006-3495(86)83468-3.

[173] J.B. Chaires, Calorimetry and thermodynamics in drug design, Annu. Rev. Biophys. 37 (2008) 135–151. https://doi.org/10.1146/annurev.biophys.36.040306.132812.

[174] N.C. Garbett, N.B. Hammond, D.E. Graves, Influence of the amino substituents in the interaction of ethidium bromide with DNA, Biophys. J. 87 (2004) 3974–3981. https://doi.org/10.1529/biophysj.104.047415.

[175] T.C. Jenkins, Optical absorbance and fluorescence techniques for measuring DNA-drug interactions., in: K.R. Fox (Ed.), Methods Mol. Biol., 1st ed., Springer-Humana, Totowa, NJ, 1997: pp. 195–218. https://doi.org/10.1385/0-89603-447-x:195.

[176] A.A. Shoara, O. Reinstein, O.A. Borhani, T.R. Martin, S. Slavkovic, Z.R. Churcher, P.E. Johnson, Development of a thermal-stable structure-switching cocaine-binding aptamer, Biochimie. 0300–9084 (2017) 30207–30209. https://doi.org/10.1016/j.biochi.2017.08.010.

[177] M.A.D. Neves, A.A. Shoara, O. Reinstein, O. Abbasi Borhani, T.R. Martin, P.E. Johnson, Optimizing stem length to improve ligand selectivity in a structure-switching cocaine-binding aptamer, ACS Sens. 2 (2017) 1539–1545. https://doi.org/10.1021/acssensors.7b00619.

[178] D.I. Li, S. Song, C. Fan, Target-responsive structural switching for nucleic acid-based sensors, Acc. Chem. Res. 43 (2010) 631–641. https://doi.org/10.1021/ar900245u.

[179] Z.R. Churcher, M.A.D. Neves, H.N. Hunter, P.E. Johnson, Comparison of the free and ligand-bound imino hydrogen exchange rates for the cocaine-binding aptamer, J. Biomol. NMR. 68 (2017) 33–39. https://doi.org/10.1007/s10858-017-0112-y.

[180] E. Guler, G. Bozokalfa, B. Demir, Z.P. Gumus, B. Guler, E. Aldemir, S. Timur, H. Coskunol, An aptamer folding-based sensory platform decorated with nanoparticles for simple cocaine testing, Drug Test. Anal. 9 (2017) 578–587. https://doi.org/10.1002/dta.1992.

[181] R. Pei, A. Shen, M.J. Olah, D. Stefanovic, T. Worgall, M.N. Stojanovic, High-resolution cross-reactive array for alkaloids, Chem. Commun. (2009) 3193–3195. https://doi.org/10.1039/b900001a.

[182] H. T. Allawi, J. SantaLucia, Nearest Neighbor Thermodynamic Parameters for Internal G·A Mismatches in DNA, Biochemistry. 37 (1998) 2170–2179. https://doi.org/10.1021/bi9724873.

[183] F.H. Niesen, H. Berglund, M. Vedadi, The use of differential scanning fluorimetry to detect ligand interactions that promote protein stability, Nat. Protoc. 2 (2007) 2212–2221. https://doi.org/10.1038/nprot.2007.321.

[184] S. Kiyonaka, T. Kajimoto, R. Sakaguchi, D. Shinmi, M. Omatsu-Kanbe, H. Matsuura, H.

Imamura, T. Yoshizaki, I. Hamachi, T. Morii, Y. Mori, Genetically encoded fluorescent thermosensors visualize subcellular thermoregulation in living cells, Nat. Methods. 10 (2013) 1232–1238. https://doi.org/10.1038/nmeth.2690.

[185] M.A.D. Neves, S. Slavkovic, Z.R. Churcher, P.E. Johnson, Salt-mediated two-site ligand binding by the cocaine-binding aptamer, Nucleic Acids Res. 45 (2016) 1041–1048. https://doi.org/10.1093/nar/gkw1294.

[186] H.T. Allawi, J. Santalucia, Thermodynamics and NMR of internal G·T mismatches in DNA, Biochemistry. 36 (1997) 10581–10594. https://doi.org/10.1021/bi962590c.

[187] J. SantaLucia, D. Hicks, The thermodynamics of DNA structural motifs, Annu. Rev. Biophys. Biomol. Struct. 33 (2004) 415–440. https://doi.org/10.1146/annurev.biophys.32.110601.141800.

[188] S. Yoshizawa, G. Kawai, K. Watanabe, K.I. Miura, I. Hirao, GNA trinucleotide loop sequences producing extraordinarily stable DNA minihairpins, Biochemistry. 36 (1997) 4761–4767. https://doi.org/10.1021/bi961738p.

[189] A.A. Shoara, Z.R. Churcher, T.W.J.J. Steele, P.E. Johnson, Analysis of the role played by ligand-induced folding of the cocaine-binding aptamer in the photochrome aptamer switch assay, Talanta. 217 (2020) 121022. https://doi.org/10.1016/j.talanta.2020.121022.

[190] Y. Zhou, Y. Wu, O. Pokholenko, M. Grimsrud, Y. Sham, V. Papper, R. Marks, T. Steele, Aptamer adaptive binding assessed by stilbene photoisomerization towards regenerating aptasensors, Sensors Actuators, B Chem. 257 (2018) 245–255. https://doi.org/10.1016/j.snb.2017.10.135.

[191] T. Li, B. Li, S. Dong, Adaptive recognition of small molecules by nucleic acid aptamers through a label-free approach, Chem. - A Eur. J. 13 (2007) 6718–6723. https://doi.org/10.1002/chem.200700068.

[192] J.S. Swensen, Y. Xiao, B.S. Ferguson, A.A. Lubin, R.Y. Lai, A.J. Heeger, K.W. Plaxco, H.T. Soh, Continuous, real-time monitoring of cocaine in undiluted blood serum via a microfluidic, electrochemical aptamer-based sensor, J. Am. Chem. Soc. 131 (2009) 4262–4266. https://doi.org/10.1021/ja806531z.

[193] M.A.D. Neves, C. Blaszykowski, M. Thompson, Utilizing a Key Aptamer Structure-Switching Mechanism for the Ultrahigh Frequency Detection of Cocaine, Anal. Chem. 88 (2016) 3098–3106. https://doi.org/10.1021/acs.analchem.5b04010.

[194] J. Hetherington, B. Savory, J.H. Turnbull, The luminescence spectra of tropine drugs, J. Photochem. 20 (1982) 367–374. https://doi.org/10.1016/0047-2670(82)87042-1.

[195] V. LeTilly, C.A. Royer, Fluorescence Anisotropy Assays Implicate Protein-Protein Interactions in Regulating trp Repressor DNA Binding, Biochemistry. 32 (1993) 7753–7758. https://doi.org/10.1021/bi00081a021.

[196] C. Perez-Gonzalez, D.A. Lafontaine, J.C. Penedo, Fluorescence-based strategies to investigate the structure and dynamics of aptamer-ligand complexes, Front. Chem. 4 (2016) 1–22. https://doi.org/10.3389/fchem.2016.00033.

[197] H.S.P. Rao, A. Desai, I. Sarkar, M. Mohapatra, A.K. Mishra, Photophysical behavior of a new cholesterol attached coumarin derivative and fluorescence spectroscopic studies on its interaction with bile salt systems and lipid bilayer membranes, Phys. Chem. Chem. Phys. 16 (2014) 1247–1256. https://doi.org/10.1039/c3cp53895h.

[198] E. Feinstein, G. Deikus, E. Rusinova, E.L. Rachofsky, J.B.A. Ross, W.R. Laws, Constrained analysis of fluorescence anisotropy decay: Application to experimental protein dynamics, Biophys. J. 84 (2003) 599–611. https://doi.org/10.1016/S0006-3495(03)74880-2.

[199] I. Lavagnini, F. Magno, A statistical overview on univariate calibration, inverse regression, and detection limits: Application to gas chromatography/mass spectrometry technique, Mass Spectrom. Rev. 26 (2007) 1–18. https://doi.org/10.1002/mas.20100.

[200] S. Bommarito, N. Peyret, J. SantaLucia, Thermodynamic parameters for DNA sequences with dangling ends, Nucleic Acids Res. 28 (2000) 1929–1934. https://doi.org/10.1093/nar/28.9.1929.

[201] B.G. Moreira, Y. You, R. Owczarzy, Cy3 and Cy5 dyes attached to oligonucleotide terminus stabilize DNA duplexes: Predictive thermodynamic model, Biophys. Chem. 198 (2015) 36–44. https://doi.org/10.1016/j.bpc.2015.01.001.

[202] V. Ladányi, P. Dvořák, J. Al Anshori, L. Vetráková, J. Wirz, D. Heger, Azobenzene photoisomerization quantum yields in methanol redetermined, Photochem. Photobiol. Sci. 16 (2017) 1757–1761. https://doi.org/10.1039/c7pp00315c.

[203] L. Fluorescence, J.L. Kinsey, Laser-Induced Fluorescence, Annu. Rev. Phys. Chem. 28 (1977) 349–372. https://doi.org/10.1146/annurev.pc.28.100177.002025.

[204] A.A. Shoara, Z.R. Churcher, S. Slavkovic, P.E. Johnson, Weak Binding of Levamisole by the Cocaine-Binding Aptamer Does Not Interfere with an Aptamer-Based Detection Assay, ACS Omega. 6 (2021) 24209–24217. https://doi.org/10.1021/acsomega.1c03781.

[205] S. Slavkovic, A.A. Shoara, Z.R. Churcher, E. Daems, K. de Wael, F. Sobott, P.E. Johnson, DNA binding by the antimalarial compound artemisinin, Sci. Rep. 12 (2022) 133. https://doi.org/10.1038/s41598-021-03958-6.

[206] K.C. Lee, B. Ladizinski, D.G. Federman, Complications associated with use of levamisole-contaminated cocaine: An emerging public health challenge, Mayo Clin. Proc. 87 (2012) 581–586. https://doi.org/10.1016/j.mayocp.2012.03.010.

[207] T.M. Brunt, J. van den Berg, E. Pennings, B. Venhuis, Adverse effects of levamisole in cocaine users: a review and risk assessment, Arch. Toxicol. 91 (2017) 2303–2313. https://doi.org/10.1007/s00204-017-1947-4.

[208] A. Larocque, R.S. Hoffman, Levamisole in cocaine: Unexpected news from an old acquaintance, Clin. Toxicol. 50 (2012) 231–241. https://doi.org/10.3109/15563650.2012.665455.

[209] M. De Jong, A. Florea, A.M. De Vries, A.L.N.N. Van Nuijs, A. Covaci, F. Van Durme, J.C. Martins, N. Samyn, K. De Wael, Levamisole: A Common Adulterant in Cocaine Street Samples Hindering Electrochemical Detection of Cocaine, Anal. Chem. 90 (2018) 5290–5297. https://doi.org/10.1021/acs.analchem.8b00204.

[210] Y. Zhou, W. Li, Y. Xiao, Profiling of Multiple Targets of Artemisinin Activated by Hemin in Cancer Cell Proteome, ACS Chem. Biol. 11 (2016) 882–888. https://doi.org/10.1021/acschembio.5b01043.

[211] M. Van De Weert, L. Stella, M. Van De Weert, L. Stella, Fluorescence quenching and ligand binding : A critical discussion of a popular methodology, J. Mol. Struct. 998 (2011) 144–150. https://doi.org/10.1016/j.molstruc.2011.05.023.

[212] S.A. Bustin, Why the need for qPCR publication guidelines?-The case for MIQE, Methods. 50 (2010) 217–226. https://doi.org/10.1016/j.ymeth.2009.12.006.

[213] P. Held, K. Newick, Using Biotek's Synergy HT Reader to Measure Reactive Oxygen Species (ROS) Generation in Stimulated Cells, Biotechniques. 46 (2009) 61–62. https://doi.org/10.2144/000113081.

[214] E. Aydindogan, S. Balaban, S. Evran, H. Coskunol, S. Timur, A Bottom-Up Approach for Developing Aptasensors for Abused Drugs: Biosensors in Forensics, Biosensors. 118 (2019) 1–27. https://doi.org/10.3390/bios9040118.

[215] C. Sester, J.A.J. McCone, A. Sen, J. Vorster, J.E. Harvey, J.M. Hodgkiss, Unraveling the binding mode of a methamphetamine aptamer: A spectroscopic and calorimetric study, Biophys. J. 121 (2022) 2193–2205. https://doi.org/10.1016/j.bpj.2022.04.027.

[216] B. Malile, J.I.L. Chen, Factors influencing polyelectrolyte-aptamer multilayered films with target-controlled permeability for sensing applications, Analyst. 141 (2016) 3794–3802. https://doi.org/10.1039/c5an02198g.

[217] A. Chamorro-Garcia, G. Ortega, D. Mariottini, J. Green, F. Ricci, K.W. Plaxco, Switching the aptamer attachment geometry can dramatically alter the signalling and performance of electrochemical aptamer-based sensors, Chem. Commun. 57 (2021) 11693–11696. https://doi.org/10.1039/d1cc04557a.

[218] P. Dauphin-Ducharme, K.W. Plaxco, Maximizing the signal gain of electrochemical-DNA sensors, Anal. Chem. 88 (2016) 11654–11662. https://doi.org/10.1021/acs.analchem.6b03227.

[219] D. Mackeigan, A.A. Shoara, M. Neves, P. Chen, C. Shen, P. Bhoria, P. Johnson, H. Ni, Apolipoprotein A-IV Polymorphisms Q360H and T347S Reduce its Inhibitory Effect against Thrombosis, Res Pr. Thromb Haemost. 5 (2021) e71-2.

[220] E.E. Ferapontova, E.M. Olsen, K. V Gothelf, An RNA aptamer-based electrochemical biosensor for detection of theophylline in serum, J. Am. Chem. Soc. 130 (2008) 4256–4258. https://doi.org/10.1021/ja711326b.

[221] Y. Liu, J. Liu, Selection of DNA Aptamers for Sensing Uric Acid in Simulated Tears, (2022). https://doi.org/10.1002/anse.202200010.

[222] A. Radi, C.K. O'sullivan, Aptamer conformational switch as sensitive electrochemical biosensor for potassium ion recognition, (2006). https://doi.org/10.1039/b606804a.

[223] J. Jumper, R. Evans, A. Pritzel, T. Green, M. Figurnov, O. Ronneberger, K. Tunyasuvunakool, R. Bates, A. Žídek, A. Potapenko, A. Bridgland, C. Meyer, S.A.A. Kohl,

A.J. Ballard, A. Cowie, B. Romera-Paredes, S. Nikolov, R. Jain, J. Adler, T. Back, S. Petersen, D. Reiman, E. Clancy, M. Zielinski, M. Steinegger, M. Pacholska, T. Berghammer, S. Bodenstein, D. Silver, O. Vinyals, A.W. Senior, K. Kavukcuoglu, P. Kohli, D. Hassabis, Highly accurate protein structure prediction with AlphaFold, Nature. 596 (2021) 583–592. https://doi.org/10.1038/s41586-021-03819-2.

[224] R. Pearce, G.S. Omenn, Y. Zhang, De Novo RNA Tertiary Structure Prediction at Atomic Resolution Using Geometric Potentials from Deep Learning, Submitted. (2022). https://doi.org/10.1101/2022.05.15.491755.

[225] J.L. Irvin, E.M. Irvin, A fluorometric method for the determination of pamaquine, J. Biol. Chem. 174 (1948) 589–596.